

Review

Progress and challenges of emerging MXene based materials for thermoelectric applications

Maiyong Zhu,^{1,*} Congcong Lu,¹ and Lingran Liu¹

SUMMARY

To realize sustainable development, more and more countries forwarded carbon neutrality goal. Accordingly, improving the utilization efficiency of traditional fossil fuel is an effective strategy for this great goal. Keeping this in mind, developing thermoelectric devices to recover waste heat energy resulted in the consumption process of fuel is demonstrated to be promising. High performance thermoelectric devices require advanced materials. MXenes are a kind of 2D materials with a layered structure, which demonstrate excellent thermoelectric performance owing to their unique physical, mechanical, and chemical properties. Also, substantial achievement has been gained during the past few years in synthesizing MXene based materials for thermoelectric devices. In this review, the mainstream synthetic routes of MXene from etching MAX were summarized. Significantly, the current state and challenges of research on improving the performance of MXene based thermoelectrics are explored, including pristine MXene and MXene based composites.

INTRODUCTION

Energy resources play a significant role in the development of industries. The utilization of fossil fuels is always accompanied by harmful substances and releases huge amounts of thermal energy. In addition, these fossil energy resources are not renewable. Significantly, the energy utilization currently is very low. As shown in Figure 1A, above 60% of energy has been wasted as heat energy during consumption. The high-grade ($T > 300^{\circ}\text{C}$) waste energy could be reused, whereas the recovery of the low grade ($T < 300^{\circ}\text{C}$) waste heat is still a great challenge.^{1,2} For sustainable development, there are at least three measurements for human beings to consider. The first solution is to reduce the utilization of these unrenewable fossil fuels. As a result, the research and utilization of new energy, such as geothermal, solar energy, wind energy, hydrogen energy, and so on, has emerged as the focus because of the aggravation of the greenhouse effect.³ The second solution might be improving the utilization efficiency of fossil fuels. In this solution, the engineering process and industrial models should be reconstructed or rearranged.⁴ Third, as a supplementary to the previous solution, harvesting, conversion and utilization of waste thermal energy, low grade waste heat in particular, might also be a promising strategy.^{5–7} Currently, electric energy is regarded as a prominent form of energy storage. As a consequence, thermoelectric devices have been a hot topic during the past years. Thermoelectric energy conversion techniques, which can directly convert heat into electricity, have gained a substantial amount of attention. Having no moving parts, thermoelectrics play an important role in the exploration of sustainable clean energies, such as radioisotope, thermoelectric power generation, and recovery of automobile exhaust heat.^{8–11} There are three thermoelectric effects, Seebeck effect, Peltier effect, and Thomson effect (Figures 1B–1D). Seebeck effect refers to the function of converting external temperature changes to electric signals via preferential diffusion of charge carriers (holes with positive charge or electrons with negative charge) under a thermal gradient, as shown in Figure 1B. For Seebeck effect, it is an electric energy generating device, in which a thermovoltage across a material ΔV will be induced by a temperature difference ΔT . The relationship between ΔV and ΔT can be described as $\Delta V = S\Delta T$, where S is called Seebeck coefficient. By contrast, for Peltier effect (Figure 1C), it is usually applied to construct cooler, in which a heat flow Q will be induced under an electric current I . The Q is greatly dependent on I , following the equation of $Q = \Pi I$, where $\Pi = TS$ is the Peltier coefficient.^{12,13} For Thomson effect (Figure 1D), it refers to a reversible cooling or heating occurring in a homogeneous conductor when an electric current and a temperature gradient co-exist. No matter what type of effect, the conversion efficiency of thermoelectric materials or devices is defined by the following formula:

¹Research School of Polymeric Materials, School of Materials Science & Engineering, Jiangsu University, Zhenjiang 212013, P. R. China

*Correspondence: maiyongzhu@ujs.edu.cn
<https://doi.org/10.1016/j.isci.2023.106718>



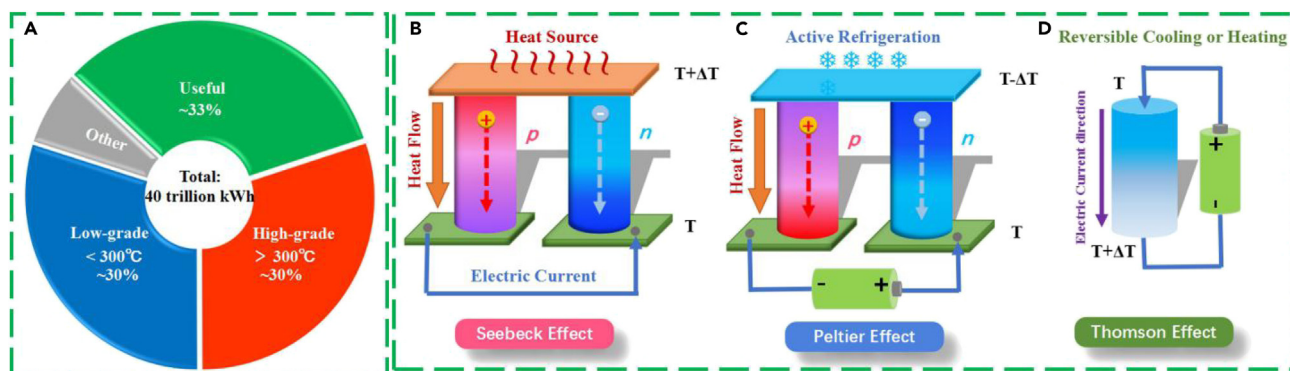


Figure 1. Diagram of energy consumption distribution and thermoelectric effect

(A) Diagram of energy consumption distribution. Data were adapted from ref. ¹. Published under a CC-BY license. Schematic illustration of thermoelectric effects.

(B) Seebeck effect, (C) Peltier effect, and (D) Thomson effect. Reproduced from ref. ¹⁴ with permission. Copyright 2020 American Chemical Society.

$$ZT = \frac{S^2\sigma}{\kappa} = \frac{S^2\sigma}{\kappa_l + \kappa_e} T \quad (\text{Equation 1})$$

Here S is the Seebeck coefficient, σ is the electrical conductivity, T is the absolute temperature, and κ is the thermal conductivity, which could be divided into two parts, lattice thermal conductivity (κ_l) and electronic thermal conductivity (κ_e). In addition, $S^2\sigma$ are usually called power factor. The challenge for rationally designing high performance thermoelectric materials is to enhance power factor $S^2\sigma$. In another word, an ideal thermoelectric material is expected possess high electrical conductivity and low thermal conductivity.

As 2D materials with good development prospects, MXene has attracted significant attention since its birth in 2011.¹⁵ Typically, the general formula of MXene could be written as $M_{n+1}X_nT_x$, in which M denotes transition metal, X represents C or/and N, T_x is used to represent functional group ($-O$, $-OH$, and $-F$), and n can be from 1 to 4.^{16–18} In the family of MXene, the combination of M and X brings the number of possible structure of MXene up to over 100. In addition, termination groups on the surface of the outmost transition metal layers increased it by another order of magnitude. Figure 2A shows current available compositions of MXene (the elements used to build MXene are marked in color) and structures of some typical MXene. Owing to the unique structure characteristics, MXene render 2D sheets with many interesting properties, such as metallic electrical conductivity, excellent mechanical properties, good biocompatibility, and aqueous solution processing without surfactants.^{19,20} Furthermore, MXene is often obtained by removing A atom from MAX through chemical etching, resulting in abundant native defects, chemically active surfaces, and high conductivity. MXene have demonstrated promise for a variety of applications and in particular for energy management for the near future.

The utilization of MXenes to attain high-performance thermoelectric devices shares several advantages. First, the high electrical conductivity and hydrophilicity of MXenes is favor for thermoelectrics. This characteristic is very different from traditional thermoelectric materials, such as Bi_2Te_3 , CuSe , and ZnSe , which usually hold n-type conduction, resulting in low electrical conductivity. What's more, the flexible surface termination groups further provide opportunities to modify MXene, yielding MXene based composites with desired functions. Besides, the intrinsic 2D layered structure allows for convenient property regulation and multilayer assembly. These characteristics provide promising opportunities to tailor the electronic and thermal properties of MXene, holding promises in thermoelectrics. Furthermore, the existence of transition metal atoms on the surface provides abundant redox activity in electrochemical processes, which is much desired when constructing a thermoelectrochemical cell. In addition, the hydroxyl-terminated surface endows good hydrophilicity for interaction with aqueous electrolyte. On the other hand, heat energy is widely found everywhere. In particular, the temperature difference between the environment and human body is capable of generating electric. As a result, wearable flexible thermoelectrics are in urgent needed. When a thermoelectric generator/cell is equipped, many wearable electronic accessories are expected to self-power without additional energy supply. Compared with many other thermoelectric materials, MXenes usually deliver better flexibility. Limited by relatively small Seebeck coefficients and high thermal conductivity in metallic systems, the MAX phases usually show poor thermoelectric

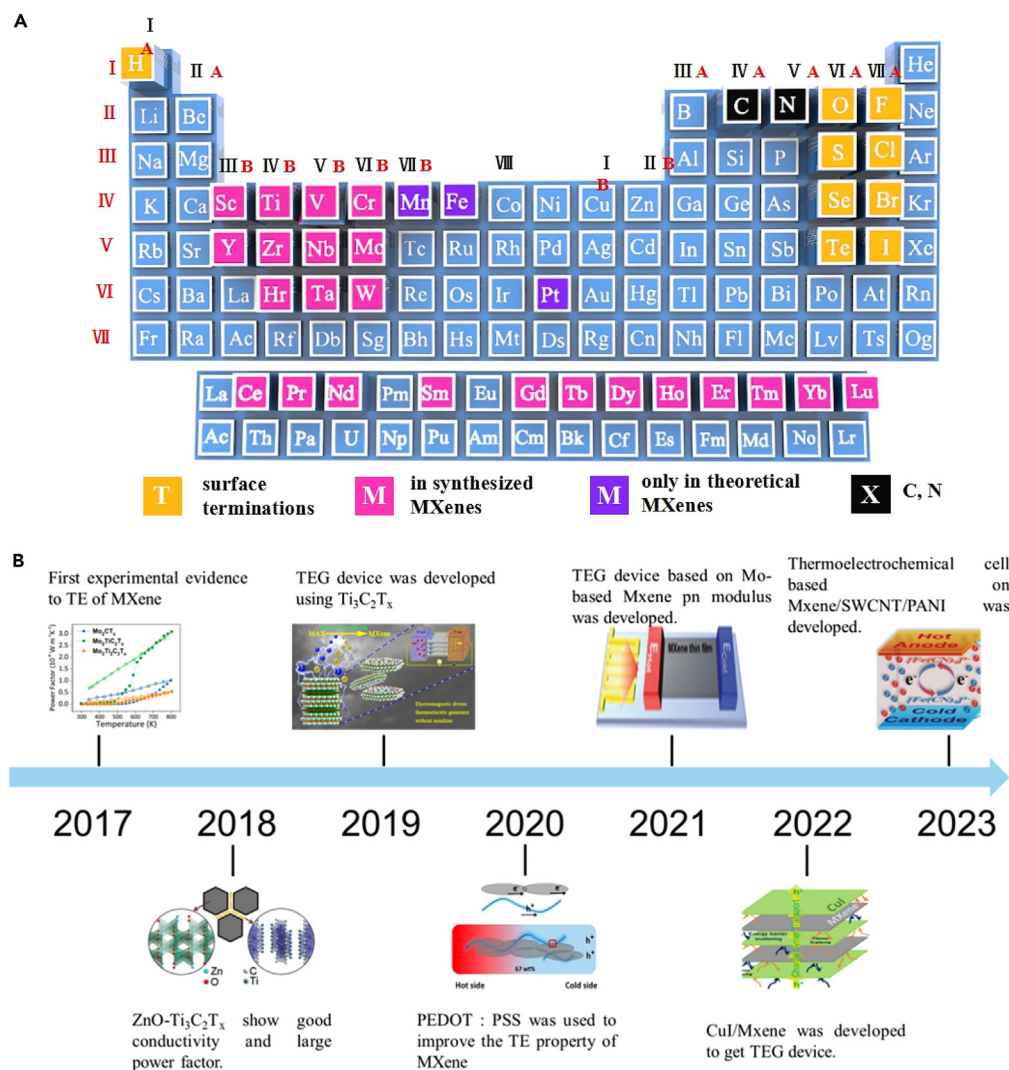


Figure 2. MXene composition and timeline for the research on thermoelectric properties/applications of MXene based materials

(A) Periodic table showing compositions of MXenes. Elements used to build MXenes are color-coded. The schematics of four typical structures of MXenes are presented at the bottom.

(B) timeline for the research on thermoelectric properties/applications of MXene based materials. Year 2017. Reproduced from ref. ²¹ with permission. Copyright 2017 American Chemical Society. Year 2018, Reproduced from ref. ²² with permission. Copyright 2018 John Wiley & Sons. Year 2019, Reproduced from ref. ²³ with permission. Copyright 2019 American Chemical Society. Year 2020, Reproduced from ref. ²⁴ with permission. Copyright 2020 American Chemical Society. Year 2021, Reproduced from ref. ²⁵ with permission. Copyright 2021 John Wiley & Sons. Year 2022, Reproduced from ref. ²⁶ with permission. Copyright 2021 John Wiley & Sons. Year 2023, Reproduced from ref. ²⁷ with permission. Copyright 2023 John Wiley & Sons.

performance. In contrast, after removing A-atom, many yielded MXenes exhibited semiconducting properties on appropriate surface terminations. Both the first principle theory and DFT predicted that semiconducting MXenes had higher Seebeck coefficient and larger electrical conductivity than conventional thermoelectric materials regardless of their relatively high thermal conductivity. Figure 2B plots timeline of MXene based materials applied in thermoelectric field, evidencing the promising prospect of MXene based materials for thermoelectric devices.

It is out of the question that MXenes may hold good promise of thermoelectric applications. The prediction is in well agreement with the fact. The development of MXene in thermoelectric application is faster

and faster. To date some reviews have been reported on the synthesis and application of MXene based materials. For example, Huang et al. reviewed MXene based nanostructures for next generation devices, including energy storage and conversion, catalysis, sensors, photodetectors, EMI shielding, degradation, and biomedical applications.²⁸ The application of four types of MXenes (Niobium carbide, vanadium carbide, titanium carbide, and molybdenum carbide) in supercapacitor, superconductor, catalysis, sensors, batteries, medical treatment, and optoelectronic devices are reviewed by Qin et al.²⁹ Aslam et al. reviewed the applications of MXenes in non-lithium energy storage technologie.³⁰ Pang et al. provided a summary of MXene structures in the production of hydrogen, ammonia, and multi-carbon compounds, as well as energy storage applications by emphasizing rational design of MXene structures.³¹ Jin et al. reviewed the synthesis of MXene materials and their application of textile sensors in the wearable field.³² Recently, Ayodhya provided a comprehensive review discussing the composites of MXene and the existing applications in various chargeable energy storage devices and sensors.³³ Sherryana et al. highlighted the role of Ti_3C_2 MXene and its potential in promoting photocatalytic hydrogen production.³⁴ Jamil et al. provided a great review on MXene, in which major preparation techniques, various important properties as well as different applications, such as solar energy storage, hybrid photovoltaic thermal system, electronic applications, desalination and other areas of thermal management field.³⁵ Although these excellent reviews on energy-related application of MXenes have been published, thermoelectric properties of MXenes are rarely summarized. Considering its rapid development, here we provided a comprehensive review focusing on the synthesis of MXene by etching MAX by highlighting the etching principles and discussing the merits and disadvantages. To assuring the comprehensive property of this review, the current two popular synthetic process of MAX, solid state reaction and solution based reaction, were also briefly introduced. Furthermore, considering the fascinating properties of MXene based materials, recent advances in MXene based thermoelectric materials, including pristine MXene, MXene/carbon composite, MXene/polymer composite, and MXene/inorganic composite, are reviewed one by one. Finally, the perspectives and challenges in the areas of MXenes and thermoelectrics were outlined. We hope to strength the connection between the fascinating compositions/structures of MXene based materials and thermoelectric properties and promote the rapid development of thermoelectric devices.

SYNTHESIS OF MAX AND MXene

MAX synthesis

Owing to the relation of “mother and son” between MAX and MXene, it is necessary to briefly introduce the strategies to obtain MAX, though the synthesis of MAX seems to be out of this review scope. Typically, MAX could be prepared by many methods, among which solid-phase reaction and solution-phase method (such as sol-gel method) are the two most popular ones. In this section, we will highlight these two methods in brief.

Solid state chemistry

As a conventional approach, solid state chemistry is the most frequently utilized method to synthesize MAX. From the element composition of MAX, one may easily to wonder the possibility of synthesizing MAX from the corresponding elementary precursors. Surely by reacting among these pure elementary precursors the corresponding MAX may be obtained, which have been verified by numerous reports.³⁶ For single transition metal containing MAX, there are three elements in MAX, so ternary phase diagram may be helpful to provide some information. In fact, the M source can also be metal hydrides, such as TiH_2 or ZrH_2 .³⁷ Take $Hf_{n+1}Al_nC$ as an example, Figure 3A depicted the ternary phase diagram of Hf-Al-C system. The formation point of HfAlC can be clearly distinguished from the phase diagram (either compositions or stoichiometry). It is noted that the formation of Hf-Al-C may require sintering at high temperature. The detail process could be described as below. Initially, as indicated by the phase diagram the powder of the three experimental starting compositions were mixed homogeneous by the assistance of milling balls in the presence of isopropanol. To obtain HfAlC phase, the powder mixture should be supposed to drying and a high temperature sintering at high pressure.³⁸ Besides Hf-Al-C, the same group extended this solid state chemistry to synthesize binary MAX phase in which two transition metals (Zr and Ti) are contained, as displayed in Figure 3B.³⁹ Similarly, Jiang et al. synthesized $Mo_2Ti_2AlC_3$ MAX by thermal treating the powder of Mo, Ti, Al, and graphite (2:2:1.2:3 M ratio) at 1600°C in argon gas flow.⁴⁰ In 2021, Nemani et al. did a benchmark work to synthesize high entropy MAX and MXene, in which there are five metal elements at M site in the structure of MAX and MXene. The synthetic process is schematically depicted in Figure 3C. The initial step was to synthesize a high entropy MAX containing five metal elements through a reactive sintering of five elemental powders. Briefly, four transition metals (TiVNbMo or TiVCrMo) were

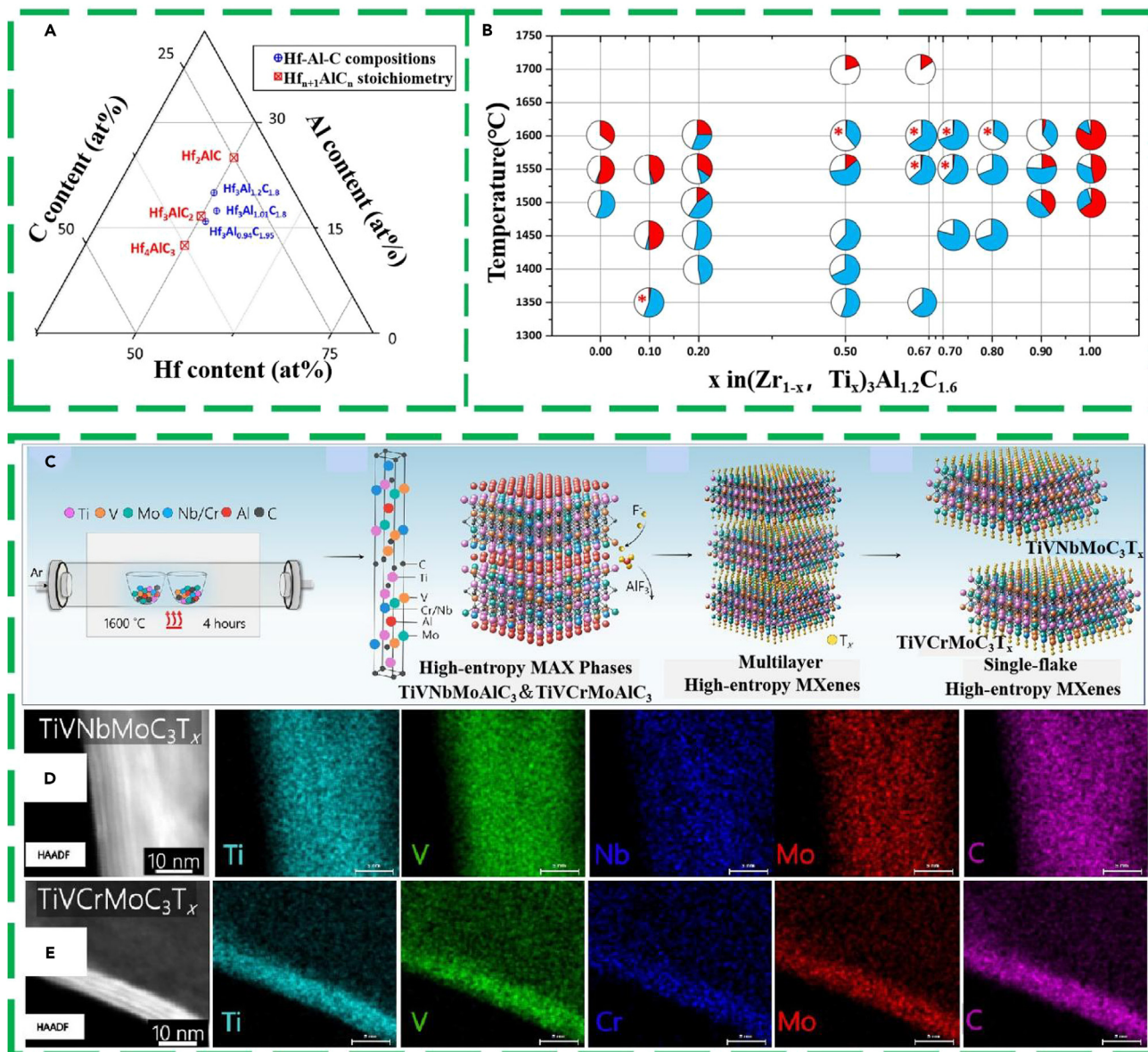


Figure 3. Solid state chemical synthesis of MXene

(A) Three starting powder compositions are indicated in blue, while the compositions of the stoichiometric compounds Hf_2AlC , Hf_3AlC_2 , and Hf_4AlC_3 are shown in red. Reproduced from ref. ³⁸ with permission. Copyright 2016 American Chemical Society.

(B) Map showing the phase assembly of MAX phase ceramics synthesized in the Zr-Ti-Al-C system, as a function of the hot-pressing temperature and the Ti content, x , in the $(\text{Zr}_{1-x}\text{Ti}_x)_3\text{Al}_{1.2}\text{C}_{1.6}$ starting powder. Reproduced from ref. ³⁹ with permission. Copyright 2017 American Chemical Society.

(C–E) Schematic illustration of the synthetic process of $\text{TiVNbMoC}_3\text{T}_x$ or $\text{TiVCrMoC}_3\text{T}_x$ and the HAADF STEM combined with EDS results of $\text{TiVNbMoC}_3\text{T}_x$ (D) or $\text{TiVCrMoC}_3\text{T}_x$ (E). Reproduced from ref. ⁴¹ with permission. Copyright 2021 American Chemical Society.

mixed with Al and carbon at equimolar ratio. Once heated from room temperature to 1600°C with a holding duration of 4 h, the mixture of the powders can be easily converted into TiVNbMoAlC_3 or TiVCrMoAlC_3 . The TiVNbMoAlC_3 or TiVCrMoAlC_3 can be converted into $\text{TiVNbMoC}_3\text{T}_x$ or $\text{TiVCrMoC}_3\text{T}_x$ by conventional etching removal of Al. From the HAADF STEM combined with EDS results (Figures 3D and 3E), one can see that uniform layered morphology and homogeneous atomic distribution of Ti, V, Nb/Cr, Mo, and C atoms in the final $\text{TiVNbMoC}_3\text{T}_x$ or $\text{TiVCrMoC}_3\text{T}_x$ product.⁴¹ Recently, Zhou et al. also prepared high-entropy laminate metal carbide MAX phase using a high-temperature solid-state reaction of Ti/V/Cr/Nb/Ta/Al/C powder mixtures in a tube furnace. To mix such multielements homogeneous, they added a small amount of ethanol.⁴²

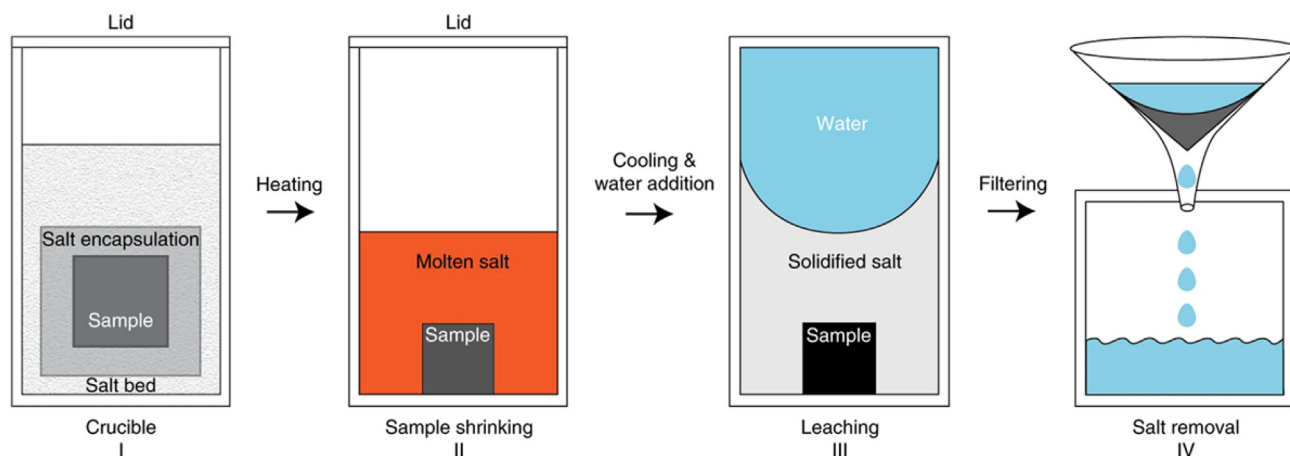


Figure 4. Schematic illustration of molten salt assisted synthesis of MXene
Reproduced from ref. ⁴⁵ with permission. Copyright 2022 John Wiley & Sons.

It is noted that the inert atmosphere is usually needed for solid state chemistry synthesizing MAX. The minor amount of oxygen may lead to the spontaneous oxidation of carbon or metal precursors, leading to the undesired quality of the MAX product. To inhibit the spontaneous oxidation, Dash et al. creatively developed a molten salt assisted synthesis technique. Their molten salt assisted technique is different from previous ones where argon atmospheres are usually needed, which could be operated in air.^{43,44} Take the work of Dash et al. as an example in case. As shown in Figure 4, the sample was encapsulated in the molten salt, which prevents the air/oxygen contacting the reaction systems. In their synthesis protocol, potassium bromide (KBr) was used as the reaction medium because it has high ductility at room temperature and can be cold-pressed to densities above 95% relative density. Taking advantage of this property of KBr, gas-tight encapsulation around a specimen can be achieved before placing it in a KBr salt bed for further heating (step I). In this way, before the system was exposed to heating, the specimen could be protected from oxidation by the gas-tight salt encapsulation. When heated, the sample is well submerged in the molten salt, and so a barrier is formed between ambient air and the sample (step II). When the reaction is completed, water was introduced to cool the system. Under such circumstance, KBr will be dissolved (step III). Free powder is then obtained by boiling the samples in water followed by filtration (step IV).⁴⁵ The benefits of utilizing molten salt as reaction medium are many. First, the synthesis temperature could be reduced, resulting in saving additional cost. Second, the reaction system could be performed in air atmosphere because the oxygen/air and the sample are isolated by the molten salt, preventing the oxidation during the sintering process. Significantly, by simply increase the batch size or setting the process continuous, such molten salt assisted process can be scaled up to industrial scale.⁴⁶ The high content of water required for the washing step might be the main disadvantage of this process, which may result in the impossibility to fully densify bulk samples in a singlestep. Later, Roy et al. have prepared V_2AlC and Ti_2AlN MAX phases in a low melting eutectic salt mixture (NaCl: KCl = 1: 1) medium using elemental powders as raw materials. The NaCl and KCl molten salt mixture not only protect the metal precursors from oxidation at high temperature but also produce the required phase at lower temperature with shorter soaking time compared to the single molten salt system.⁴⁷

Solution based process

Considering the high cost of solid state chemistry methods, which limit their practical application at an industrial scale, scientists are always looking for solution based approaches to synthesize MAX materials. Furthermore, some MAX, such as Cr_2GaC can not be synthesized via traditional solid state chemistry.⁴⁸ Siebert et al. proposed a sol-gel method to prepare Cr_2GeC MAX. The synthesis process includes two steps. Initially, the sol and gel was formed by dispersing germanium ethoxide, $Cr(NO_3)_3$, citric acid in ethanol. Afterward, the gel was combusted at $1000^\circ C$ for several hours under the constant Ar flow, thus forming Cr_2GeC MAX. Alternatively, the gel can also be converted into Cr_2GeC MAX through a microwave assisted route, instead of combustion boat. Obviously, the carbon resource in this work is citric acid. It is noted that citric acid may be converted into graphite under microwave irradiation, so the amount of citric acid in the precursor system is critical for the purity of the final MAX product. Siebert et al also prepared V_2GeC MAX by using vanadyl(IV) acetylacetonate to replace $Cr(NO_3)_3$.⁴⁹ Besides direct synthesis single transition

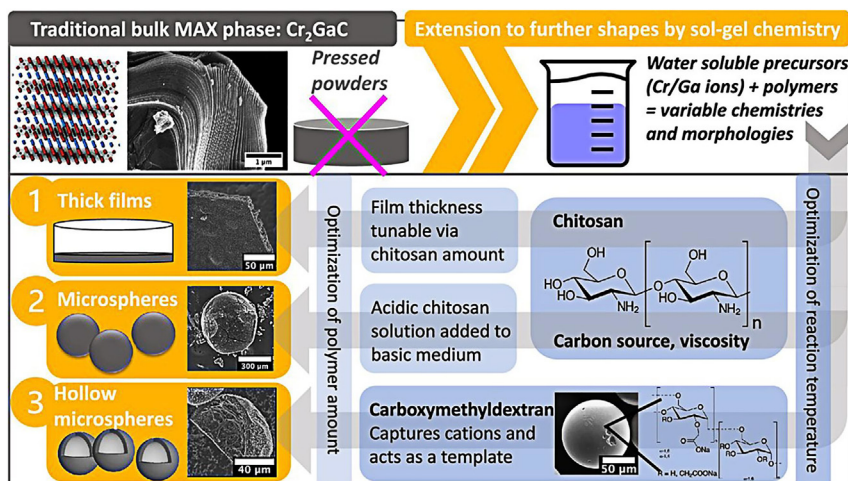


Figure 5. Preparation of MAX materials by sol-gel method

Schematic visualization of transitioning from traditional approaches to the more versatile wet chemistry to allow for higher degrees of freedom in the achievable shapes and morphology of MAX phase Cr₂GaC. Reproduced from ref. ⁵² with permission. Copyright 2023 American Chemical Society.

metal-containing MAX, some authors of the same group proved that double transition metal-containing MAX is also available via such sol-gel process, such as (Cr/Mn)₂AlC₂ and (Cr/Fe)₂AlC₂.^{50,51} Recently, Siebert et al. extended sol-gel method to prepare MAX with different morphology. In their recent work, the introduction of biopolymer into the gel enables the synthesis of the model compound in the form of thick films as well as full and hollow microspheres. As shown in Figure 5, by optimizing the amount of biopolymer and reaction temperature, the shape of Cr₂GaC MAX could be well controlled from solid microsphere, hollow microspheres, and thin films. Take chitosan as an example in case, the use of biopolymer template shares several advantages. For one thing, chitosan as a nature biopolymer ensure the precursors are able to dissolve in water, making the possibility to use Cr/Ga ions as metal resources. For another thing, the versatile nature of chitosan ensures the tuning morphology of the template. The required viscosity of the system (entanglement of cationloaded polymer chains) can be easily obtained to make thick films with the potential to use different shaped molds. For the full microspheres, the water solubility of chitosan makes the formation of spherical beads. As for the hollow microspheres, the aggregated chitosan exposes the negative charged surface to capture the metal cations and acted as the template.⁵²

Typically, solid state chemistry process shares the advantages of pure product, simple cooperation. The high energy consuming might be the main disadvantage of solid state chemistry because the synthesis temperatures are typically required up to 900°C and 1700°C.^{53–55} Furthermore, a milling step is added to obtain powders before the heating treatment, which makes the process complex. Using advanced techniques (such as microwave irradiation) the thermal cycles and reaction temperature may be reduced. Nevertheless, microwave presents some limitations in synthesizing large samples because of temperature gradients. At last, in some cases the use of metallic hydrides might be dangerous because of the liberation of H₂ during the thermal process. Compared to traditional solid-state chemistry, sol-gel chemistry offers a variety of advantages over classical solid-state chemistry, such as milder reaction conditions and greater processibility. The choice of raw materials is wide. For M resource, numerous metal ions/salts may be available. For carbon resource, many organic molecules as well as polymers may work. The disadvantage of sol-gel chemistry synthesizing MAX lies in the residual impurity in the final product, though the amount of impurity usually is minor. Besides solid state chemistry and sol-gel based solution process, there are some other techniques for synthesizing MAX phase materials, such as physical vapor deposition,^{56,57} pressureless synthesis,^{58,59} hot isostatic pressing route,⁶⁰ replacement reaction,^{61–63} carbothermal,⁶⁴ microwave heating accompanied by spark plasma sintering,⁶⁵ and conventional/nonconventional combinations.⁶⁶ Readers interested in this field can refer to specific literature.

MXene synthesis

Since the birth of MXene in 2011, many researchers are devoted to synthesize MXene and investigate the properties and potential applications of MXene. Generally, MXenes are prepared by selectively etching A

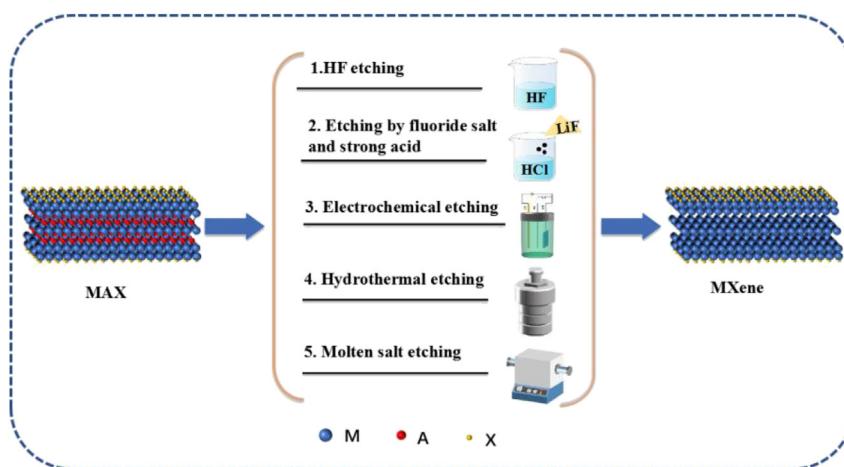


Figure 6. Diagram of popular synthetic routes to etch MAX into MXene

atoms from MAX phases. On delamination, ultrathin single/few-layer MXene flakes can be readily obtained. They can be expressed as $M_{n+1}X_nT_x$, where T stands for the surface functional group, such as -O, -F, and -OH. To date, many MXene materials are mainly produced from the parent 2D MAX via top-down process. Depending on the reactivity difference of M and A in MAX, some reagents are able to etching A from MAX. On the basis of reagent used and technique involved, these etching methods can mainly be divided into five categories (Figure 6), which are HF etching, fluoride salt etching, electrochemical etching, hydrothermal etching, and molten salt etching. In this section, we will briefly discuss them.

HF etching

HF is the most common utilized etching agent to remove A atom layer from MAX. The mechanism of etching removal of A atoms includes several reactions. Using HF etching technique, Naguid et al. from the group discovering MXene prepared a series of MXenes via immersing MAX phases (including Ti_2AlC , Ta_4AlC_3 , $(Ti_{0.5}Nb_{0.5})_2AlC$, $(V_{0.5}Cr_{0.5})_3AlC_2$, and Ti_3AlCN) to remove Al atoms.⁵⁷ Take HF etching Al atoms from Ti_3AlC_2 as an example. To obtain single or few layer MXene materials, the whole process involves two procedures, an etching procedure followed by an exfoliation treatment, as depicted by Figure 7.⁶⁸ The first reaction occurs between Ti_3AlC_2 and HF. Owing to the high electronegativity of F and the weak interaction between Al atom layer and Ti layer in Ti_3AlC_2 , AlF_3 is easy to form in this step. Meanwhile, hydrogen gas simultaneously is generated. The removal of Al atoms fails to destroy the layered structure of the materials. As a result, the yielded Ti_3C_2 maintains the layered structure of Ti_3AlC_2 . The etching process is usually carried out in aqueous solution, consequently, Ti_3C_2 is easy to form hydrolysis reaction, which is the second reaction in the system. In this reaction, the Ti element is oxidized while H element is reduced, so hydrogen gas is also generated accompanying the formation of $Ti_3C_2(OH)_2$. At the same time, the excessive HF may also react with Ti_3C_2 to yield $Ti_3C_2F_2$ and hydrogen gas. The above-mentioned reactions could be simply described as below:



To date, numerous MXene materials have been synthesized via HF etching removal of A atoms from the parent MAX phase. Table 1 summarized some typical MXene materials gained by etching removal of A atoms from parent MAX phase using HF as etching agent. From this table, one may see that the etching performing condition varies with MAX phases. This is because the bonding energy of A-M is different in different MAX phases. The advantage of HF etching is simple operation and mild condition. Nevertheless, HF etching possesses several cons such as the toxicity of HF itself, the generation of H_2 as byproduct which is dangerous. Moreover, the highly corrosive nature of HF usually does damage to the product, such as causing pores in the product, which decrease the mechanical strength of the product.^{69,70} In addition,

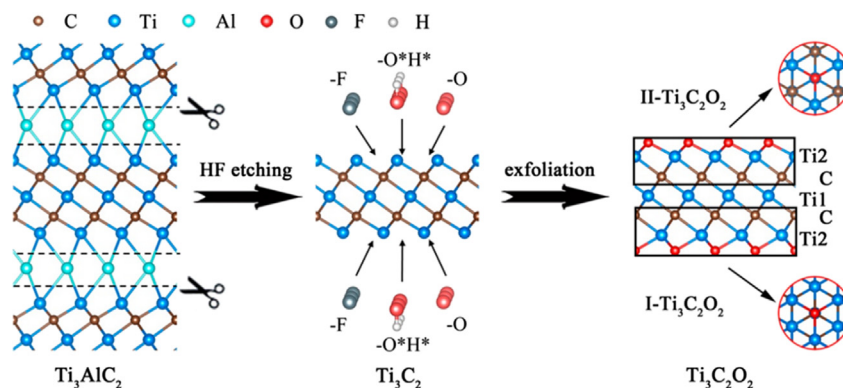


Figure 7. Schematic exfoliation process of MXenes from MAX phases

The red circles show the configurations I and II in vertical views. Reproduced from ref. ⁶⁸ with permission. Copyright 2016 American Chemical Society.

the resultant MXene obtained with HF usually exhibited multilayered structure with an accordionlike structure, after which a further delamination procedure is necessary by tetramethylammonium hydroxide (TMAOH) or tetrabutylammonium hydroxide (TBAOH).⁷¹ At last but not least, theory calculations have predicted that carbon vacancy is easily generated during the HF etching and exfoliation process because the formation energy of carbon vacancy is very low (1.7 eV).⁷²

Etched by fluoride salt and strong acid

To avoid directly using HF as etching agent, researcher proposed improved methods. One effective strategy is replacing HF with the mixture of fluoride salt and HCl. In this way, when MAX phases are immersed into the mixture of fluoride and HCl, HF will be *in-situ* formed to etching MAX phase. Ghidui et al. prepared two-dimensional Ti_3C_2 by etching Ti_3AlC_2 in a mixture solution of LiF and HCl. Of interest, the resulting hydrophilic material swells in volume when hydrated, and can be shaped like clay and dried into a highly conductive solid or rolled into films tens of micrometres thick.¹⁶ Later, Tian et al., Sun et al. and Kim et al. also prepared such materials using the similar process.^{86–88} Figure 8A depicted a typical operation

Table 1. Typical MXene materials prepared via HF etching removal of A atom from parent MAX phases

MAX	MXene	Etching agent	condition	Reference
Mo_2GaC	Mo_2C	50% HF	3 h	Meshkian et al. ⁷³
Mo_2TiAlC_2	$Mo_2TiC_2T_x$	HF	–	Anasori et al. ⁷⁴
$Mo_2Ti_2AlC_3$	$Mo_2Ti_2C_3T_x$	HF	–	Anasori et al. ⁷⁵
Ti_3AlC_2	$Ti_3C_2T_x$	50% HF	Room temperature 18 h	Liu and Li ⁷⁶
Ti_3AlC_2	$Ti_3C_2T_x$	48% HF	Room temperature 20 h	Guo et al. ⁷⁷
Ti_3AlC_2	$Ti_3C_2T_x$	49% HF	60°C, 4–36 h	Peng et al. ³⁶
Nb_2AlC	Nb_2CT_x	40% HF	60°C, 48 or 72 h	Peng et al. ³⁶
Mo_2Ga_2C	Mo_2CT_x	25% HF	55°C 8 days	Guo et al. ⁷⁸
Ti_2CO_2	Ti_3C_2	HF	Room temperature	Naguib et al. ⁷⁹
Ti_3AlC_2	$Ti_3C_2T_x$	40% HF	room temperature one day	Hermawan et al. ⁸⁰
	e-TAC	HF	80°C, 2h	Xie et al. ⁸¹
Ti_3AlC_2	$Ti_3C_2(OH/ONa)_x F_{2-x}$	40% HF	313 K, 10 h	Peng et al. ⁸²
Ti_3AlC_2	$Ti_3C_2T_x$	45% HF	60°C, 24 h	Yang et al. ⁸³
Mo_2Ga_2C	Mo_2CT_x	48% HF	60°C 7 days	Luo et al. ⁸⁴
V_2AlC	V_2CT_x	50% HF	Room temperature 8 h	Naguib et al. ⁸⁵
Nb_2AlC	Nb_2CT_x	50% HF	Room temperature 90 h	Gonzalez-Julian et al. ⁵⁸
Ti_3AlC_2	$Ti_3C_2T_x$	50% HF	2 h	Naguib et al. ¹⁵

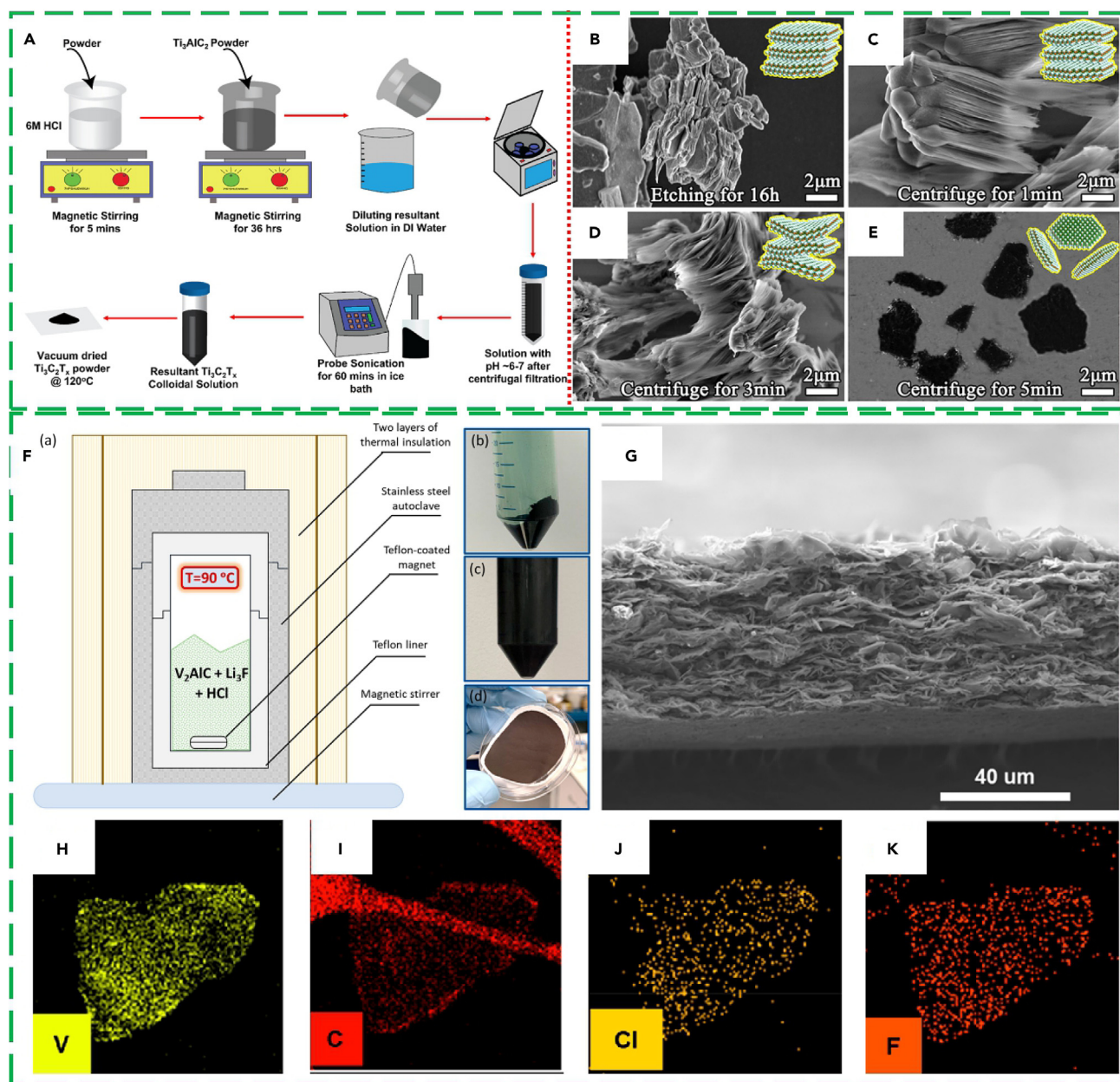


Figure 8. Schematic illustration of procedures for preparing $Ti_3C_2T_x$ MXene using LiF and HCl as etching agent

(A) traditional experimental process. Reproduced from ref. ⁸⁹ with permission. Copyright 2022 American Chemical Society. SEM images of $Ti_3C_2T_x$ obtained via LiF/HCl etching 16 h (B), centrifuged for (C) 1 min, (D) 2 min, and (E) 5 min. Reproduced from ref. ²³ with permission. Copyright 2019 American Chemical Society.

(F) Improved fluoride salt and HCl etching process to prepared V_2C MXene.

(G) Typical SEM image of the V_2C MXene.

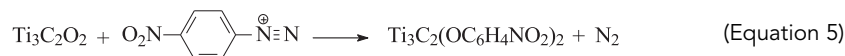
(H–K) Corresponding elemental maps from the dark-field STEM image of the individual V_2C MXene. Reproduced from ref. ⁹⁴ with permission. Copyright 2022 American Chemical Society.

procedures for prepare $Ti_3C_2T_x$ from Ti_3AlC_2 using LiF and HCl as etching agent. In this protocol, no particular instruments are involved.⁸⁹ Besides LiF and HCl system as etching agent, other fluoride salt may also work, such as FeF_3 , KF, and cobalt Fluoride (CoF_2 or CoF_3).^{15,90–92} The etching time and centrifugation have significant impact on the quality of the product. Usually, the etching time is long because it includes at least stages, *in-situ* formation of HF and reaction between the parent MAX and HF. Figures 8B–8E shows the

products of the process of preparing $\text{Ti}_3\text{C}_2\text{T}_x$ in the work of He et al., where through LiF/HCl etching followed by centrifugation, granular Ti_3AlC_2 was transformed into sheet-shaped $\text{Ti}_3\text{C}_2\text{T}_x$ MXene. Initially, multilayered $\text{Ti}_3\text{C}_2\text{T}_x$ was formed by etching Ti_3AlC_2 particles with LiF/HCl for 16 h. The obtained multilayered $\text{Ti}_3\text{C}_2\text{T}_x$ exhibits an accordionlike structure. As shown in Figures 8C–8E, the layer distance of interlayer in $\text{Ti}_3\text{C}_2\text{T}_x$ gets larger and larger when a brief centrifugation applied. Such result was also obtained by Zhang et al.⁹³

To simplify the preparation process, Firestein et al. develop an improved LiF/HCl etching process to synthesize 2D delaminated V_2C (d- V_2C), which is very simple and includes only a single-step.⁹⁴ The synthetic experiment setup is schemed in Figure 8F, in which the mixture of LiF and HCl was utilized as etching reagent. The etching process was carried out in a hydrothermal autoclave. In this way, the etching process could be restricted in the closed environment of autoclave under continuous stirring different from previous ones, where the delamination can not occur during the etching process. Here delamination is expected to occur *in situ*, i.e., during washing of etched V_2C with deionized water. Compare to previous studies, the utilization of a thermal insulating fabric is another important advantage of this approach, which assures the temperature of the reaction mixture was stable (90°C) through the whole process.^{95,96} SEM image of the product (Figure 8G) reveals a characteristic layered stack of delaminated MXene flakes. As for the chemical composition, which was identified through the dark-field scanning TEM combined with EDS mapping analysis. As shown in Figures 8H–8K, the representative electron image and elemental maps of an individual nanosheet reveals that the V_2C is composed of V, C, Cl, F. Obviously, Cl and F are terminated groups in the product, which are originated from the etching reagent.

The properties of MXenes are much dependent on surface terminations. For example, traditional termination groups (either O containing or F containing) render MXenes hydrophilic surface, benefiting their dispersion in water. For some cases, hydrophobic surface may be desired. Considering the inactivity of the O and/or F termination groups, which are expected to mask the active sites for N_2 reduction reaction, Guo et al. developed a strategy to convert these termination groups on the surface of $\text{Ti}_3\text{C}_2\text{T}_x$ into iron-containing species. Thanks to the chemical changes on the surface of $\text{Ti}_3\text{C}_2\text{T}_x$ and strong coupling interactions between Fe and Ti species, the surface work function was reduced dramatically, leading to an enhanced catalytic reactivity of MXene toward N_2 reduction.⁷⁷ To tuning the surface group of MXenes, To avoid the formation of -O, or -OH terminated MXene, organic solvent might be preferred. Natu et al. developed a water free process to prepare MXene.⁹⁷ By using organic polar solvents in the presence of ammonium dihydrogen fluoride, $\text{Ti}_3\text{C}_2\text{T}_z$ flakes rich in fluorine terminations were obtained. Jing et al. forwarded a solid-liquid reaction process to graft 4-nitrophenyl groups onto $\text{Ti}_3\text{C}_2\text{T}_x$ MXene. The whole process can be depicted as Figure 9A. The first etching removal of Al atom layer is the same as traditional reports. The subsequent delamination process is different. In their work, MXene were placed on substrates in 4-nitrobenzene-diazonium (4-NBD) in anhydrous acetonitrile (CH_3CN) for 10 min with N_2 bubbling. The diazonium modification processes are described by the following chemical equations: usually the terminal groups in $\text{Ti}_3\text{C}_2\text{T}_x$ are in the form of = O, - OH, and - F. These groups possess lone electron pairs which are easy to be transformed to electron-accepting species if any. As a result, when treated with 4-NBD, aryl diazonium cation may get the lone pair electrons from = O and - OH, subsequently releasing a molecule of N_2 to yield an aryl radical (Equations 4 and 5). The aryl radical can form a covalent bond with an oxygen atom and/or a titanium atom in the $\text{Ti}_3\text{C}_2\text{T}_x$ lattice. As for the - F terminal groups, the lone-pair electrons in the F of $\text{Ti}_3\text{C}_2\text{T}_x$, shown in Equation 6, may be seized by the diazonium ion, forming F-Ph bond, which are more stable than Ti-F bond. As such, the terminal groups in was removed as the byproduct of $\text{FC}_6\text{H}_4\text{NO}_2$. Through above analysis, one can easily conclude that the graft amount of 4-NBD would absolutely be dependent on the termination O-containing groups because F groups are removed from MXene. As shown in Figure 9B, aromatic C=C bond stretching, asymmetric and symmetric stretching bands were observed at 1595.0, 1517.8, 1346.2, and 1103.2 cm^{-1} , respectively. The above phenomena indicate that the 4-NBD was successfully anchored onto the surface of MXene. By anchoring 4-NBD molecules, the work function, conductivity, and mobility of the MXene can be controlled.⁹⁸



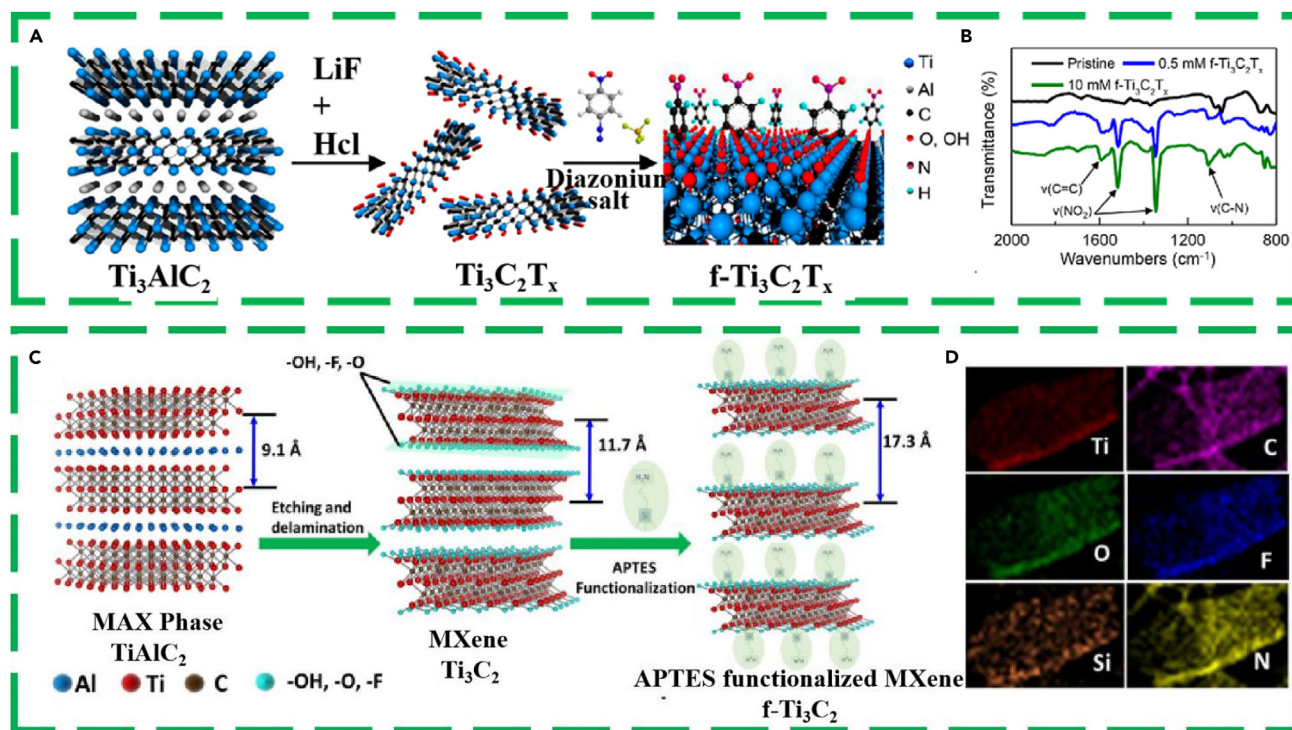
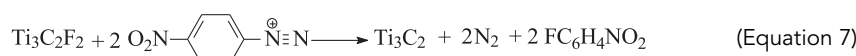
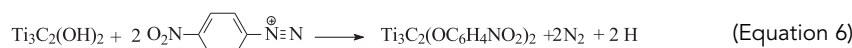


Figure 9. Organic solvents adjust MXene surface groups

(A) Schematic diagram of synthesis and subsequent diazonium functionalization of $Ti_3C_2T_x$.

(B) diazonium functionalized FTIR spectrum of $Ti_3C_2T_x$. Reproduced from ref. ⁹⁸ with permission. Copyright 2021 American Chemical Society.

(C) Schematic illustration of synthesizing APTES functionalized Ti_3C_2 MXene as well its EDS mapping (D). Reproduced from ref. ⁹⁹ with permission. Copyright 2018 Elsevier.



MXenes are expected to provide huge surface area and space, which are benefited for accommodate guest molecules, such as enzyme. To increase the binding affinity between MXene and enzyme, functionalizing MXene with organosilicon molecules is a preferred strategy. Kumar et al. developed a process to functionalize MXene with (3-Aminopropyl)triethoxysilane (APTES) (Figure 9C). After etching removal of Al atoms and delamination, Ti_3C_2 MXene could be obtained. By adding 1 mg of APTES into the suspension of 100 mg of Ti_3C_2 MXene dispersed on 50 mL of ethanol, APTES functionalized Ti_3C_2 MXene would be yielded. As shown in Figure 9D, the elements of Si, O, N were homogeneous distributed on the surface of functionalized Ti_3C_2 owing to the existence of NH_2 , the functionalized Ti_3C_2 can be used for covalently immobilize anti-CEA. After immobilization of anti-CEA, the Ti_3C_2 MXene immobilizing anti-CEA could be used to construct electrochemical biosensor for detecting cancer biomarker.⁹⁹

Fluoride salt and HCl replacing HF can avoid direct using hazardous HF and the etching environments provide opportunity to further modify the surface, morphology, and chemical reactivity of MXene. The flexible select of fluoride salt may further boost the application range of this method. Sometimes the fluoride can provide additional function besides etching reagent. For example, when $FeCl_3$ and HCl was used to etching Ti_3AlC_2 , Fe(III) ions may enter the interlayer spaces of MXene, increasing the water reactivity of $Ti_3C_2T_x$ toward forming TiO_2 anatase. The case for cobalt ions intercalating, it is more advantageous. For one thing, the size of cobalt ions is relative larger, whose intercalation could provide a stable expanded interlayer space. For another thing, the intercalated cations could be able to be converted into other functional component (such as oxide particles), thus processing MXene into a composite. However, when

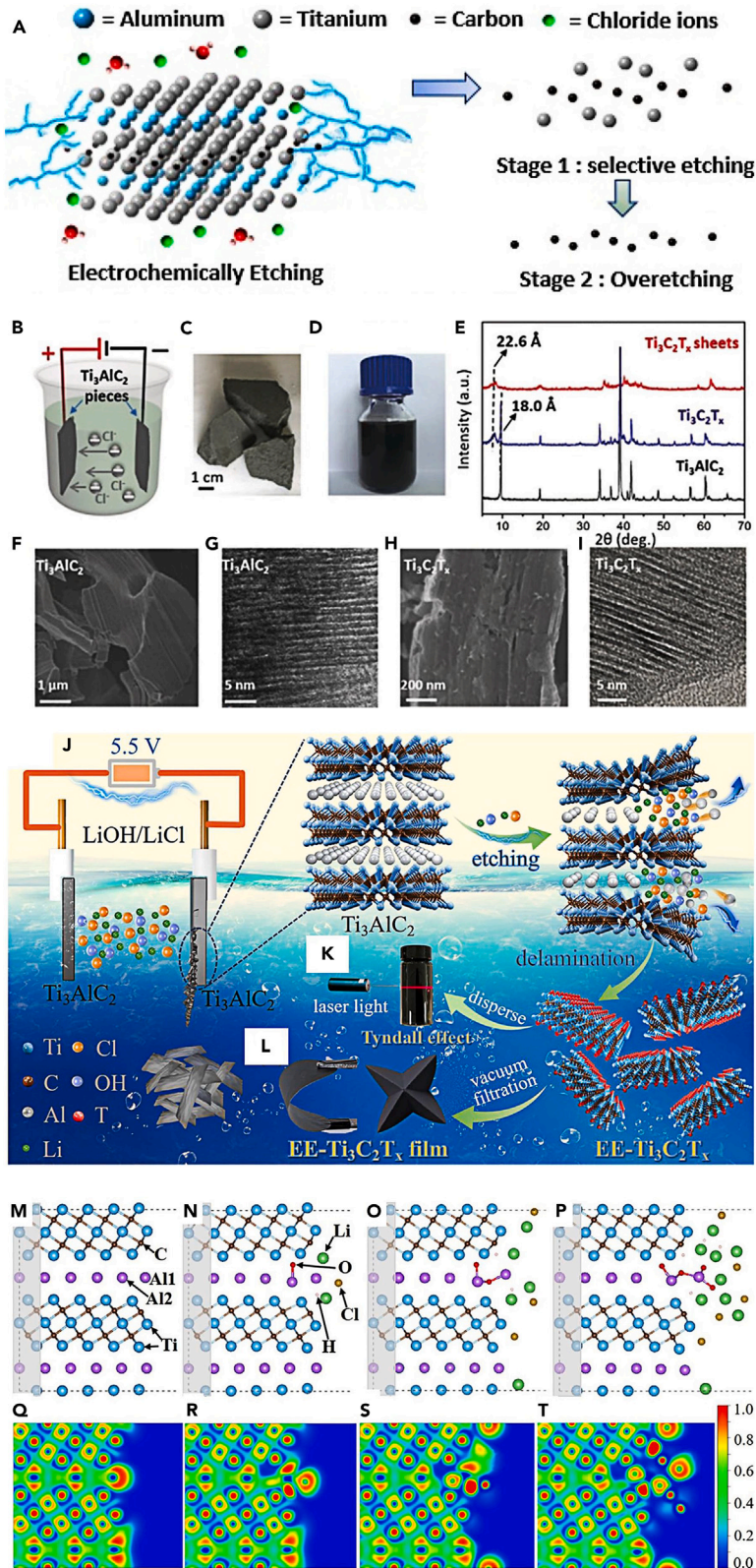


Figure 10. Electrochemical etching in aqueous solution

(A) Mechanism of electrochemical etching Ti_2AlC to Ti_2CT_x in HCl. Reproduced from ref.¹⁰² with permission. Copyright 2019 American Chemical Society.
 (B–I) Schematic illustration and characterization of Ti_2CT_x prepared via electrochemical etching MAX in binary aqueous electrolyte. Reproduced from ref.¹⁰³ with permission. Copyright 2018 John Wiley & Sons.
 (J) Schematic illustration of the electrochemical etching synthesis of $Ti_3C_2T_x$ in LiOH/LiCl solution.
 (K) Photograph of $Ti_3C_2T_x$ dispersion showing Tyndall effect.
 (L) Photographs of $Ti_3C_2T_x$ films.
 (M–P) Lowest-energy atomic configurations and (Q–T) corresponding ELF plots of the pristine Ti_3AlC_2 and the etched Ti_3AlC_2 with increasing amounts of LiOH and LiCl. Reproduced from ref.¹⁰⁴ with permission. Copyright 2022 American Chemical Society.

etching Al-containing MAX with fluoride salt, a significant amount of crystalline $AlF_3 \cdot 3H_2O$ may simultaneously be formed during the etching process, which is a common undesired byproduct. The residual crystalline $AlF_3 \cdot 3H_2O$ may affect quality of the final MXene. Post-synthesis treatments, such as washing with HCl, have to be taken to obtain pure MXene. Similar to HF etching process, fluoride salt based etching methods are also usually time consuming (surpassing 24 h, not including the repeated washing stages). Much F-based reagents are involved, which are dramatically hypertoxic, leading to serious safety and environmental concerns. Moreover, the resultant MXenes are terminated by F-based groups, which would seriously impede the transportation of electrolyte ions and sacrifice the electroactive sites.

Electrochemical etching

In chemical principle, the underlying mechanism for etching removal of A atom layers in MAX phase is attributed to the higher chemical active nature of the M–Al bond than the M–C bond. Theoretically, all process involving charge/electron transfer can be designed as an electrochemical process. As a consequence, MAX could be electrochemically etched to MXene. In the past years, extensive efforts have been devoted to synthesize MXene via electrochemical methods. In 2017, Sun et al. proposed an electrochemical etching method to convert Ti_2AlC to Ti_2CT_x using 2 M HCl aqueous electrolyte. Owing to F-based reagent free, the resultant MXenes possess only –Cl terminal groups, as well as the common ones, such as –O and –OH. It is well known that many parameters, such as the potential window, current density, the concentration of electrolyte, as well as the surface properties of electrode, are critical for electrochemical process, and these parameters may vary with the electrochemical processing. In their system, the over-etching of parent Ti_2AlC phases may occur, leading to the formation of carbide-derived carbon.¹⁰⁰ Lukatskaya et al. also noticed the formation of amorphous carbon when selectively removing Al layers from Ti_3AlC_2 by anodic etching in dilute NaCl, HCl, and HF solutions.¹⁰¹ Pang et al. prepared Ti_2CT_x by electrochemical etching Ti_2AlC in HCl solution. As displayed in Figure 10A, the etching mechanism involves two stages. Initially, Al atom in Ti_2AlC was removed by an applied voltage because of the weaker Ti–Al bond than Ti–C bond. Afterward, both Al and Ti atoms are etched until only monolayer carbon atoms are retained. The overall etching reaction on Ti_2AlC is described as follows:



Similar to the work of Sun et al., the resultant Ti_2CT_x MXenes possess only Cl-terminated groups and some common –OH and –O group. Compared to Sun's work, the optimal etching time was shortened to be 9 h by gentle heating.¹⁰²

It is well known that Al is an amphoteric metal which can react with both acids and bases. The etching of Al foil via conventional acids/bases has been experimentally verified many years ago.^{105,106} To figure out applicable electrolyte for removing Al layer from MAX phases, Yang et al. examined various aqueous solutions, including sulfuric acid (H_2SO_4), nitric acid (HNO_3), sodium hydroxide (NaOH), ammonium chloride (NH_4Cl), and ferric chloride ($FeCl_3$). The results reveal that chloride-containing electrolytes possess apparent etching effects. This is attributed to the strong binding capability of Cl^- with Al. Unfortunately, limited by kinetic problems, the etching reactions take place preferentially on the surfaces.¹⁰⁷ Taking this concerning in mind, the authors of the same group proposed a binary aqueous system to electrochemically etch Ti_3AlC_2 for obtaining Ti_3C_2 . In their protocol, NH_4Cl and TMA-OH was utilized as electrolytes. As shown in Figures 10B–10D, two pieces of bulk Ti_3AlC_2 was used as electrodes. It is noted that in this system the cathode also acted as a counter electrode, so the etching process only took place on the surface of the anode. It is noted that TMA-OH here plays two roles. For one thing, together with NH_4Cl it is the component of the electrolyte. For another thing, TMA-OH would dissociate into TMA^+ and OH^- .

The generated OH⁻ ions are capable of combining with NH₄⁺ from the dissociation of NH₄Cl, forming NH₄OH. As a consequence, the intercalation of NH₄OH into the interlayer of Ti₃C₂T_x may occur in the electrochemical etching system, which may enlarge the interlayer distance, thus improving the etching kinetics. A series of characterization (XRD and SEM) in Figures 10E–10I confirmed this conclusion. Owing to the absence of fluoride-containing reagent in the system, the termination groups on the surface of the exfoliated Ti₃C₂T_x (T = O, OH) flakes exclude any fluorine terminations. As expected, the exfoliated Ti₃C₂T_x (T = O, OH) delivers excellent supercapacitor performance, which surpasses those made from traditional wet-chemical approaches.¹⁰³ As a successive of the above work, the same group proposed an iodine-assisted etching strategy for preparing Ti₃C₂T_x in acetonitrile solvent. Though no electrochemical techniques were applied, the real driving force for the etching processing is the moderate redox potential of I₂/I⁻ ($E^\ominus(I_2/I^-) = 0.54$). However, in this protocol a further HCl delamination treatment is needed.¹⁰⁸

Very recently, Chen et al. developed another binary aqueous system based electrochemical etching process to prepare F-free and Cl-containing Ti₃C₂T_x MXene. As shown in Figure 10J, the etching process was carried out in LiOH/LiCl solution using two identical Ti₃AlC₂ electrodes at a potential window of 5.5 V. The choice of LiOH/LiCl combination lies in two aspects. For one thing, Cl-containing electrolytes are able to etch Ti₃AlC₂ owing to the strong interaction between Cl⁻ and Al. For another thing, the amphoteric nature of Al enables it to react with OH⁻.¹⁰⁹ whole etching process includes two steps. First, Al was removed by Cl-containing electrolyte and OH⁻ owing to the weaker bond strength of Ti–Al than that of Ti–C. Second, Li⁺ in the electrolytes can intercalate into the Ti₃C₂T_x layers, enlarging the interlayer distances by weakening the interactions between adjacent layers. Owing to such intercalation and no organic solvent used, the surface of the synthesized Ti₃C₂T_x is expected to be can be excellent hydrophilicity, making the synthesized Ti₃C₂T_x water dispersible (Figure 10K). In addition, the good film-forming ability of the Ti₃C₂T_x makes the Ti₃C₂T_x film highly flexible, which can be folded into a special shape without fracture Figure 10L. Another merit of this process is ascribed to the high etching efficiency of 92.2% within 5 h. Furthermore, no addition delamination is needed and sonification alone is able to delaminate Ti₃C₂T_x without using any hazardous organic intercalant. The detail etching mechanism is illustrated in Figures 10M–10P, which can be well evidenced by the corresponding ELF plots in Figure 10Q–10T.¹⁰⁴

Besides carrying out in aqueous solution, electrochemical etching can also be performed in organic solvent. For some applications, we may need MXene materials with hydrophobic surface or terminated with desired organic functional groups. Under these circumstances, electrochemical etching in organic solvent might be preferred. Yang et al. prepared Ti₃C₂T_x MXene quantum dots (MXene QDs) via a simple electrochemical etching process which was followed by a bath sonication delamination procedure. As shown in Figure 11A, their experimental setup is very simple, in which the Pt and Ag were utilized as counter electrode and reference electrode, whereas the Ti₃AlC₂ was working electrode. The electrolyte was non-aqueous ionic liquid 1-butyl-3-methylimidazolium hexafluorophosphate ([BMIM]–[PF₆]) and acetonitrile (MeCN). Once a potential was applied on working electrode, the fluoride-containing ionic liquid will release F⁻, which would etching Al from Ti₃AlC₂, forming Ti₃C₂T_x. The exfoliation potential of Ti₂AlC₂ is crucial, which could be determined by cyclic voltammetry (CV) testing of an electrolyte with 1.0 M [BMIM][PF₆] in MeCN. Under optimal condition, the etching process can be finished within 5 h. The microstructure of the MXene QDs is clearly visible in TEM images, as shown in Figures 11B and 11C, which show uniform and ultrasmall MXene QDs. HRTEM image in Figure 11D reveals that the lattice fringes had an inner plane spacing of 0.21 nm, corresponding with (0110) facet of Ti₃C₂ MXene. The average lateral size was determined to be ~5.34 nm as shown in Figure 11E.¹¹⁰

Hydrothermal etching

Hydrothermal technique is a versatile method to prepare various functional materials. In a typical hydrothermal process, all reactants are sealed in a vessel where a high temperature (usually above the boiling point of solvent) and a high pressure is provided. Compared to conventional wet-chemical and solid state chemical processes, hydrothermal possesses high efficiency and energy economical characteristics. In view of thermodynamic point, the attack of base to Al in MAX can occur under standard condition. The practical difficulty is a kinetic problem in which a thin layer protective some oxide/hydroxide is often formed on the surface of MAX, preventing the etching reaction.¹¹¹ Recently, hydrothermal has been utilized for exfoliating MAX to synthesize MXene. Peng et al. prepared Ti₃C₂ and Nb₂C MXene via hydrothermal method. In their protocol, NaBF₄ and HCl was used as etching reagents, which can occur reaction to form HF.³⁶ Li et al. have

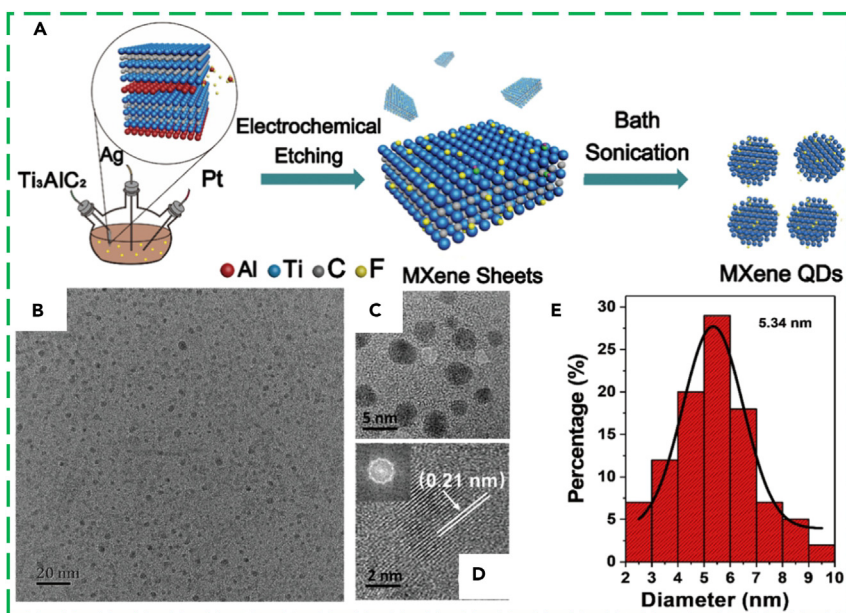


Figure 11. Electrochemical etching in organic solvents

(A) Process for the preparation of $Ti_3C_2T_x$ MXene Quantum Dots by an electrochemical etching technique in CH_3CN containing ionic liquid.

(B–D) Characterization of $Ti_3C_2T_x$ including TEM (B and C), HRTEM (D) and size distribution (E). Reproduced from ref. ¹¹⁰ with permission. Copyright 2020 American Chemical Society.

reported a hydrothermal synthesis of $Ti_3C_2T_x$ MXene using NaOH as alkali. Typically, $Ti_3C_2T_x$ MXene terminated with -OH and -O with high purity was synthesized via treating Ti_3AlC_2 with NaOH under hydrothermal condition. The etching removal of Al layer from MAX involves two steps, oxidation of Al into Al oxide/hydroxide and the dissolution of Al oxide/hydroxide. Intrinsically, the reaction between MAX and NaOH is a heterogeneous one. The outer Al atoms are prone to oxidation and dissolution by NaOH. With reaction processing, the inner Al atoms may be oxidized and dissolved only if the concentration of NaOH is enough. As shown in Figure 12A, both the concentration of NaOH and reaction temperature has significant impact on the quality of the final product. In particular, owing to the jamming effect, at low concentration of NaOH

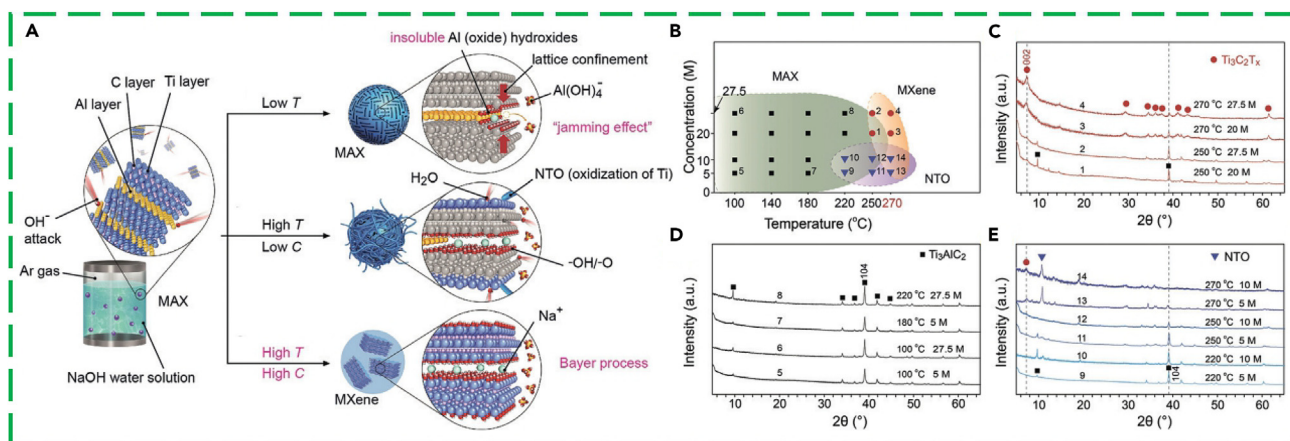


Figure 12. NaOH as alkali hydrothermal synthesis of $Ti_3C_2T_x$ MXene

(A) Schematic illustration of hydrothermal etching Ti_3AlC_2 MAX to synthesize $Ti_3C_2T_x$ MXene.

(B) formation of $Ti_3AlC_2T_x$ under various hydrothermal temperatures and NaOH concentrations. Dominant products for 24 batches of samples prepared under different conditions. Red circles: MXene; black squares: MAX; blue triangles: NTOs. There are three regions of according to the main product.

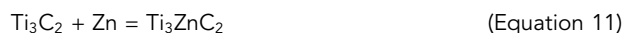
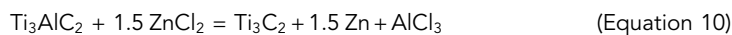
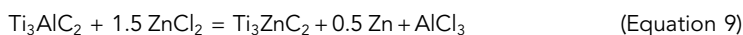
(C–E) XRD patterns of the products gained at different conditions. Reproduced from ref. ¹¹² with permission. Copyright 2018 John Wiley & Sons.

(either high temperature or low temperature), with the etching processing, the inner Al atoms oxidize as well. However, the newborn Al hydroxides (Al(OH)₃), and their dehydrated oxide hydroxides (AlO-(OH)) may form. The dissolution of the newborn Al(OH)₃ may be prevented. On the other hand, the dissolution of Al(OH)₃ with NaOH is an endothermic reaction, which is favored on increasing the reaction temperature. In addition, the oxidation of Ti in Ti₃AlC₂ is possible, leading to the formation of Na/K-Ti-O compounds (NTOs). Obviously, the formation of NTOs is not desired for synthesizing MXene. To figure out the optimal experiment condition, the authors carried out a series of experiments. Figure 12B provided the dominant products for 24 batches of samples prepared under different conditions (combination of different concentration of NaOH and different hydrothermal time). From the visible result one can see three product region, MXene (marked as red circles), MAX (marked as black squares), and NTOs (blue triangles). The products were further identified via XRD (Figures 12C–12E). On the above evidence, the optimal condition was set to be 27.5 M NaOH under 270°C. It is noted that an argon atmosphere should be provided to alleviate the oxidation of the sample.¹¹² Of interest, Jiang et al. prepared several mildly oxidized MXenes ((mo-Nb₂CT_x, mo-Ti₃C₂T_x, and mo-V₂CT_x) via a hydrothermal process, in which LiF and HCl were utilized as etching reagent. The reason for their work to allow the MXenes to be mildly oxidized might be because of the fact that F-terminated MXenes usually provide unsatisfied electrochemical performance when acting as electrode candidates.¹¹³

Under hydrothermal condition, all reactants are expected to dissolve and the reaction rates are much higher than those under conventional wet-chemical processes. Meanwhile, currently mature operation equipment and optimum route are available for hydrothermal process. Certainly there are also several drawbacks utilizing hydrothermal method to prepare MXene. Similar to other wet chemical process, MXenes prepared via hydrothermal method usually need to be further modified to meet the requirement of specific application because it is difficult to real *in-situ* activation in a typical hydrothermal process. In addition, the equipment from using acid/alkali solution is not avoidable.

Molten salt etching

Although electrochemical and hydrothermal etching avoids resorting to HF solution, the use of aqueous solutions introduces a mixture of Cl, O, and OH surface groups. Recently, water-free etching has attracted extensive attention, among which molten salt etching is one of the most popular strategies. Li et al. developed a ZnCl₂ molten salt assisted etching strategy to prepare Cl-terminated MXene. Take Ti₃C₂Cl₂ as an example in case, the synthetic process is schematically depicted in Figure 13. The formation mechanism involves two steps. Initially, Al atoms at A sites of Ti₃AlC₂ was replaced by Zn atoms, forming Ti₃ZnC₂. The driving force for this step is ascribed to two aspects. For one thing, the strong Lewis acidity of ZnCl₂ can produce strong electron-accepting ligands, which can react with the A element in the MAX phases because Ti-Zn bonds are thermodynamically more stable than Ti-Al bonds. Simultaneously, the A-layer (here is Al atom layer) diffusion process at high temperature can also promote the formation of Ti₃ZnC₂. The second step is the formation of Ti₃C₂Cl₂. This step can only take place on condition that excessive amount of ZnCl₂ is used (The molar ratio of Al-MAX to ZnCl₂ here was 1:6). The reactions involved in the process can be summarized as below.



By flexibly selecting salt constituents and precisely control the reaction temperatures, the authors of this group synthesized a variety of MAX phases (Ti₃ZnC₂, Ti₂ZnC, Ti₂ZnN, and V₂ZnC) and MXenes (Ti₃C₂Cl₂ and Ti₂CCl₂). The results indicate a general and controllable approach to synthesizing

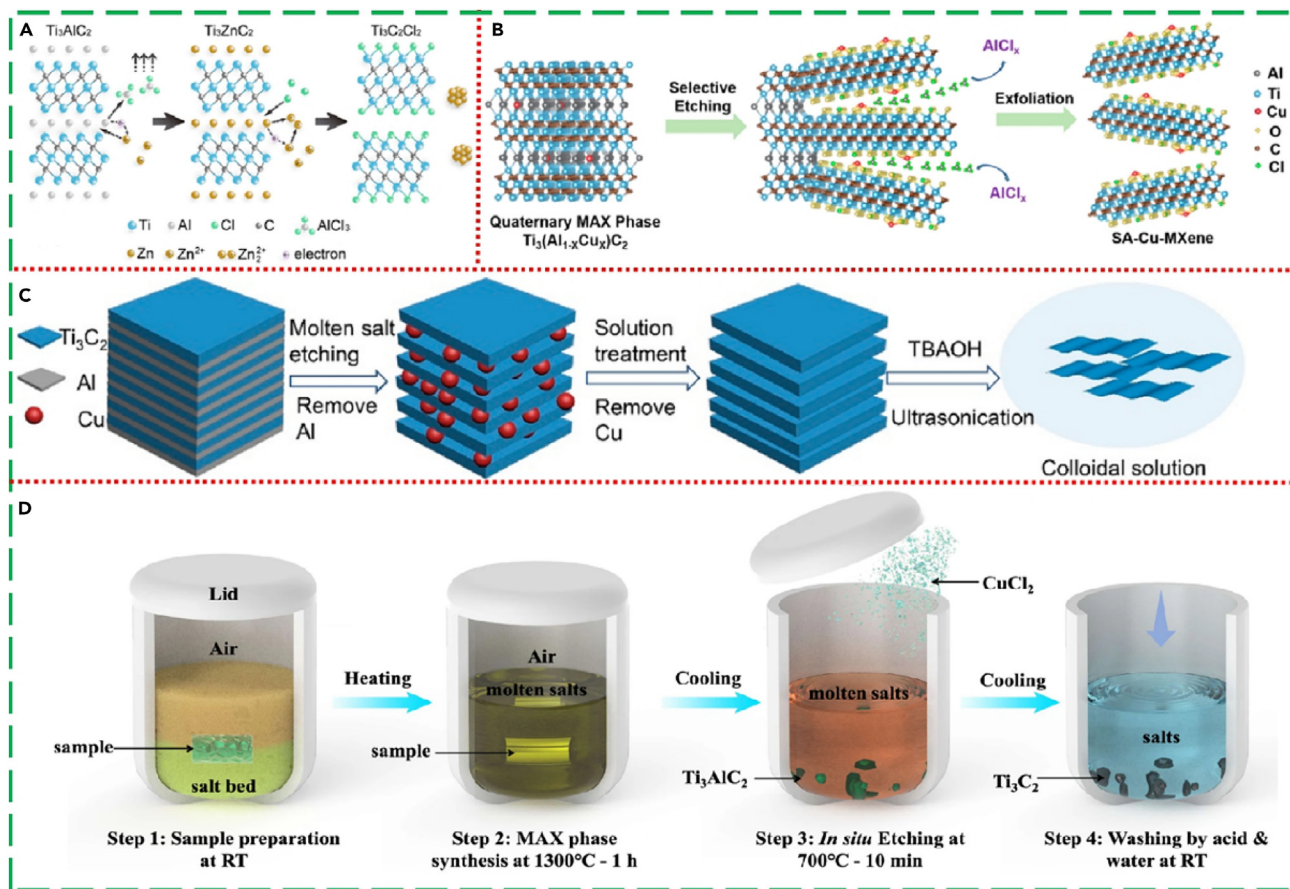


Figure 13. MXene was prepared by molten salt assisted etching

(A) Process for preparing $\text{Ti}_3\text{C}_2\text{Cl}_2$ MXene using ZnCl_2 molten salt etching method. Reproduced from ref. ¹¹⁴ with permission. Copyright 2019 American Chemical Society.

(B) Schematic illustration for the synthesizing SA-Cu-MXene by selective etching quaternary $\text{Ti}_3(\text{Al}_{1-x}\text{Cu}_x)\text{C}_2$. Reproduced from ref. ¹¹⁵ with permission. Copyright 2021 American Chemical Society.

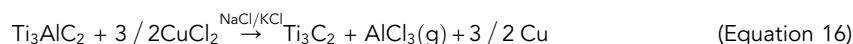
(C) Schematic illustration for the synthesis of Ti_3AlC_2 MAX phase by a one-pot process integrating the fabrication and etching of MAX. Reproduced from ref. ¹¹⁶ with permission. Copyright 2022 American Chemical Society.

(D) Schematic illustration of one-pot molten salt synthetic process of Ti_3C_2 MXene using Ti, Al, and C as raw materials. Reproduced from ref. ¹¹⁷. Published under a CC-BY license.

nanolaminated MAX phases and the derivation of halide group terminated MXenes from its respective parent MAX phase.¹¹⁴

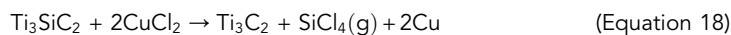
Using a quaternary $\text{Ti}_3(\text{Al}_{1-x}\text{Cu}_x)\text{C}_2$ MAX as precursor, Zhao et al. prepared single atom Cu immortalized on MXene. In this work, the etching removal of Al atoms from the quaternary $\text{Ti}_3(\text{Al}_{1-x}\text{Cu}_x)\text{C}_2$ MAX phase is crucial. The innovated thought lies in the removal of Al with simultaneously preserving Cu atoms in the product. As depicted in Figure 13B, when the quaternary $\text{Ti}_3(\text{Al}_{1-x}\text{Cu}_x)\text{C}_2$ MAX was immersed into the molten ZnCl_2 at 600°C , Al layers in MAX phase reacted with zinc chloride to produce AlCl_3 . Meanwhile, the easy sublimation of AlCl_3 would promote the etching remove of Al atoms in the A layer. As for the preservation of Cu, it was related to the intrinsic nature of Cu. The residual Cu atoms generates accordionlike single atom Cu immortalized MXene (SA-Cu-MXene). Here, it should be emphasized that the complete removal of Al is also supposed to occur at excessive amount of ZnCl_2 (in the work mass ratio of $\text{Ti}_3(\text{Al}_{1-x}\text{Cu}_x)\text{C}_2$ to ZnCl_2 is 1 : 5).¹¹⁵ By analyzing the works of Li et al. and Zhao et al., one may conclude that the excessive amount of ZnCl_2 is necessary to assure the removal of Al. Otherwise, the Zn would only replace Al resided in MAX. From the intrinsic mechanism analyzing, one may also know that the excessive amount of Cl^- plays crucial role because the formed AlCl_4^- is the leaving species of Al. Taking these considerations as well as the high price of ZnCl_2 , Liu et al. proposed another molten salt etching process to

remove Al atoms from Ti_3AlC_2 to prepare Ti_3C_2 . The whole etching process is shown in Figure 13C.¹¹⁶ In their work, $CuCl_2$, NaCl and KCl were used as molten salt etching reagent. Obviously, $CuCl_2$ is the crucial one whereas NaCl and KCl may be expected to act as solvent providing Cl^- . Compared to $ZnCl_2$, these three chlorides ($CuCl_2$, NaCl and KCl) are much cheaper. Similar to $ZnCl_2$ system, the Lewis acid of Cu^{2+} may react with Al layer to form Cu on the MXene surface, whereas Al is converted into $AlCl_3$ gas, which is benefit for expanding the interlayer distance of MXene. Excess Cu^{2+} also partially reacts with the exposed Ti atoms from Ti_3C_2 to form metallic Cu, whereas charge compensation is ensured by Cl^- anions reacting to form $Ti_3C_2Cl_2$. The etching reactions can be described as below.



Ma et al. combined the molten salt etching process with the synthesis of MAX phase, resulting a one-pot molten salt process to obtain MXene from raw Ti, Al, and carbon. The fabrication protocol is schematically illustrated in Figure 11D, which involves four steps. Initially, a pellet was prepared by mixing stoichiometric amounts of titanium, alumina and graphite powders with NaCl and KCl, followed by a pressing treatment on a steel die. Afterward, Ti_3AlC_2 MAX phase was achieved via heating the pellet to 1300°C. At this temperature, Ti, Al, and carbon are expected to react and give Ti_3AlC_2 , different from traditional process where the synthesis of MAX and MXene are separate. The as yielded Ti_3AlC_2 MAX phase is not necessary to be isolated from the molten NaCl and KCl medium. By adding $CuCl_2$ into the system, the etching removal of Al atom layer may occur via the reduction of Cu^{2+} ions into the Cu and concomitant Al oxidation into the volatile $AlCl_3$ phase. Finally, after cooling to room temperature, a water plus $(NH_4)_2S_2O_8$ washing was applied to remove the solidified salts and Cu from the MXene particle surface.¹¹⁷ Besides Ti-based MXene, other MXene can also be prepared via molten salt etching process. Dong et al. report the preparation of Nb_2CT_x MXene by $CuCl_2+KCl+NaCl$ molten salts, in which $CuCl_2$ was the etching agent to react with Nb_2AlC , whereas NaCl and KCl were used as salt bed.¹¹⁸ Different from Zn, Cu is a relative inert metal element. It should be pointed out that the formed elemental Cu may reside in the product after the etching reaction is completed. As a result, a further removing Cu procedure is needed to obtain pure Ti_3C_2 MXene. In their work, ammonium persulfate (APS), which is a strong oxidant, is used to oxide Cu particles, thus removing Cu. Owing to the introduction of the strong oxidant which also contains O element, this final MXene prepared from this molten salt route is expected to be terminated with O and Cl surface groups. Though $CuCl_2$, NaCl and KCl share the advantages of lower price over $ZnCl_2$, the strong oxidant APS may cause some environmental issues such as releasing SO_2 . Very recently, Huang et al. demonstrated that the Ti_3AlC_2 could be etched into $Ti_3C_2T_x$ in molten $MCl_2 \cdot nH_2O$ ($M = Fe, Co, Ni$), in which the $MCl_2 \cdot nH_2O$ were reduced into M particles. Of interest, they further transformed the residual M particles into MS_x via sulfurization. The final resulted $Ti_3C_2T_x/MS_2$ delivered excellent sodium storage performance.¹¹⁹ In another work, to avoid the post operation of removing metal particles caused by the redox reaction between molten $CuCl_2$ and MAX, developing simple and environmentally sound processes are always desired. Shen et al. forwarded an integrated process (MS-E etching) combining molten salt and electrochemical technique to etching MAX phase yielding MXene. In this way, cathode reduction and anode etching can be spatially isolated, resulting in metallic impurities absence in MXene product. Moreover, this strategy is superior in modification because the surface terminations can be *in situ* modified from-Cl to-O and/or-S by adding various inorganic salts. As a result, the modification steps are greatly shortened and the variety of surface terminations is enriched as well. Last, but not least, such MS-E etching can be regarded as a sustainable method owing to the two significant aspects. For one thing, no acidic liquid waste is produced during the whole process. For another thing, the salt can be reused.¹²⁰

In 2020, Li et al. have further proved that the molten salt etching technique to synthesize MXene is powerful tool. In their work, a series of MAX materials with different atoms in A site ($A = Al, Si, \text{ or } Ga$) were used as precursors to synthesize various MXenes. Take a site of Si as an example, the derivation process for converting Ti_3SiC_2 into Ti_3C_2 can be shown in Figure 14A. Similar to Liu et al.'s work, the etching process includes two steps, which involve the follow reactions.



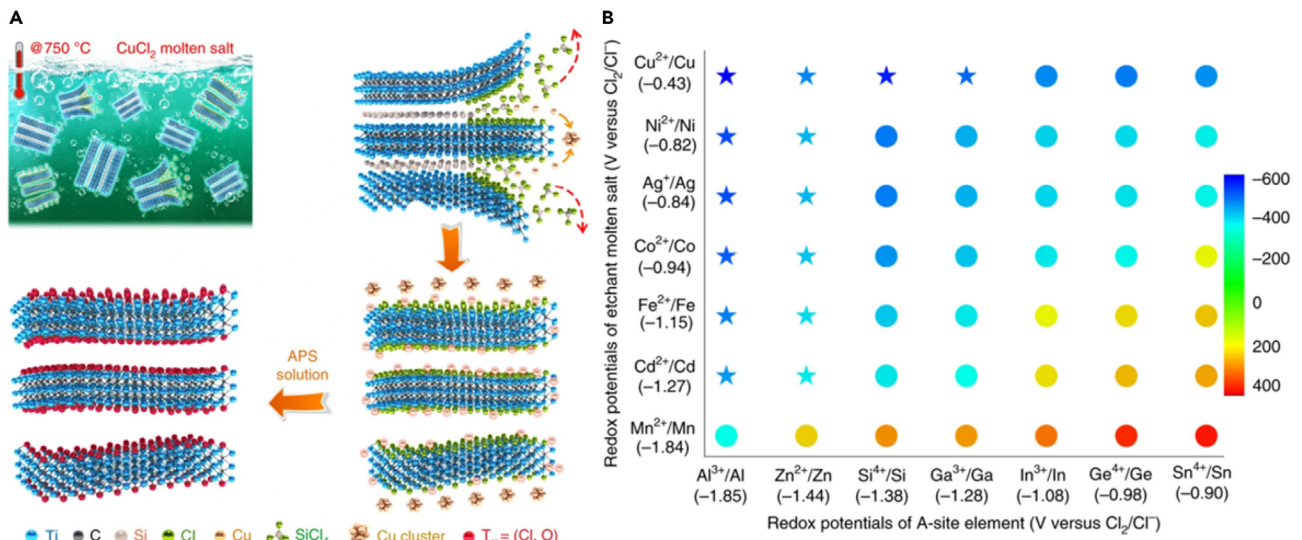


Figure 14. Synthesis of MXenes using MAX materials with different atomic sites as precursors

(A) Schematic illustration of synthesis of Ti₃C₂T_x using CuCl₂ molten salt etching process.

(B) Gibbsfree energy mapping (700°C) guiding the selection of Lewis acid Cl salts according to the electrochemical redox potentials of A-site elements in MAX phases (x axis) and molten salt cations (y axis) in Cl melts. Stars mark the corresponding MXenes demonstrated in the current study. All symbols (stars and spots) were calculated using the same approach; the star symbols were experimentally verified in this paper, whereas spot symbols remain theoretical prediction. Reproduced from ref. ¹²¹. Published under a CC-BY license.

The Lewis acid of Cu²⁺ is expected to oxidize the exposed Si atoms which are weakly bonded to Ti in the Ti₃C₂ sublayers, forming SiCl₄ phase. SiCl₄ is easy to sublimation because its boiling point is just 57.6°C. Similar the reports elsewhere,^{114,116} excess Cu²⁺ partially reacts with the exposed Ti atoms from Ti₃C₂ accompanied by the formation of metallic Cu, whereas charge compensation is ensured by Cl⁻ anions, forming Ti₃C₂Cl₂. To remove Cu from the MXene, either APS or FeCl₃ was available. Besides etching Ti₃AlC₂ to form Ti₃C₂, other MAX phases were also tested in their group. By a series of experimental evidence, they proposed a generic method to etch MAX phases by direct redox coupling between the A element and the cation of the Lewis acid molten salt, which could be described as below:



Obviously, this is a redox reaction. To make the reaction spontaneous, the potentials of B^{x+}/B ($E_{(B^{x+}/B)}$) and A^{y+}/A ($E_{(A^{y+}/A)}$) are expected to meet the requirement:

$$E_{(B^{x+}/B)} > E_{(A^{y+}/A)} \quad (\text{Equation 21})$$

Furthermore, the Gibbsfree energy change ($\Delta_r G_m$) of the reaction could be calculated using the following equation:

$$\Delta_r G_m = -nF(E_{(B^{x+}/B)} - E_{(A^{y+}/A)}) \quad (\text{Equation 22})$$

Here n refers to the number of electron transferred in the redox reaction, and F refers to the Faradic constant, which is 96485C/mol.

Theoretically, those reactions with a negative value in Gibbsfree energy change are expected to work for synthesize MXene. Rational combination of chloride molten salt and MAX is capable of forming corresponding MXene. Figure 14B provide a Gibbsfree energy mapping with the electrode potentials. Guided by this mapping, some combinations (star symbols) have been verified in experiment, whereas some (spot symbols) are only theoretically verified.¹²¹ Here, what should be pointed out is that for practical synthesis, one should simultaneously consider kinetic factors besides thermodynamic factors.

Considering the postmodification of MXenes, the Cl- or Br-terminated MXenes are preferred to O- or F-terminated ones. Take Ti-based MXene as example; this can be verified by the fact that the bond strengths of Ti-F and Ti-O are more stable than Ti-Cl and Ti-Br. Their formation enthalpies are confirmed to

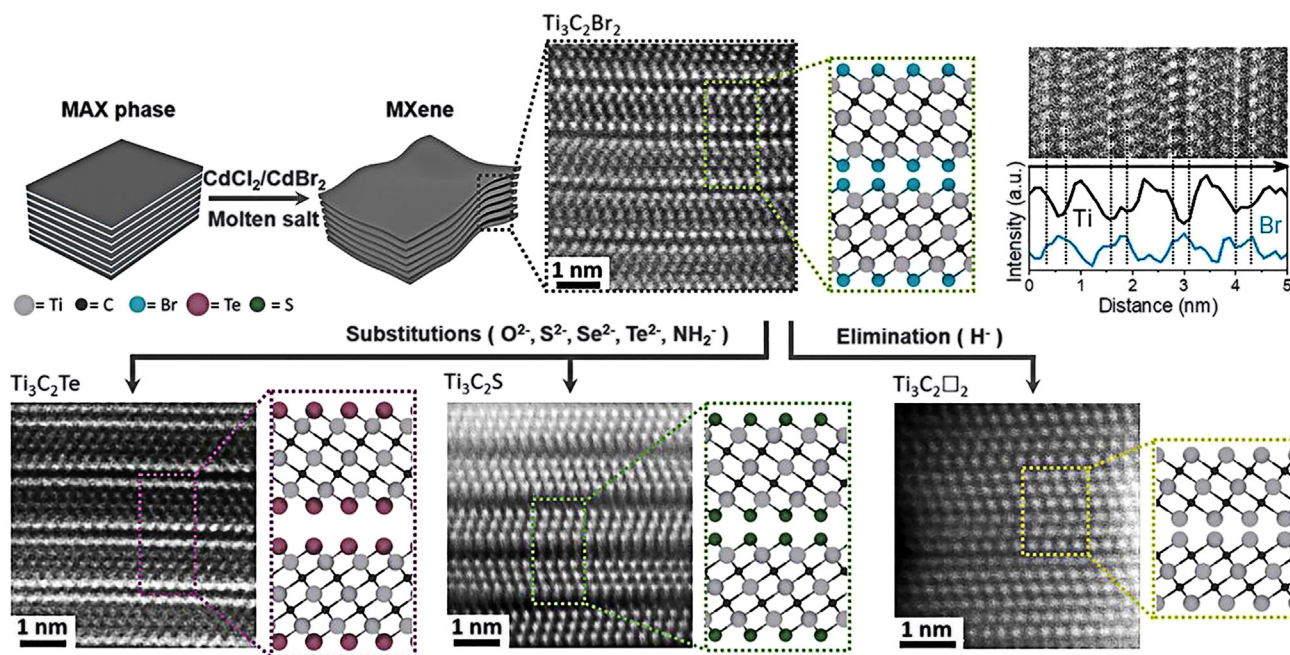


Figure 15. Schematic illustration of molten etching process to prepare $\text{Ti}_3\text{C}_2\text{Br}_2$ MXene as well as its derivatives
Reproduced from ref. ¹²² with permission. Copyright 2020 Prof. Dmitri V. Talapin.

be -617 kJ/mol (TiBr_4), -804 kJ/mol (TiCl_4), and -1649 kJ/mol (TiBr_4). Kamysbayev et al. developed a general strategy to install and remove surface groups by performing substitution and elimination reactions in molten inorganic salts. As shown in Figure 15. In the presence of CdCl_2 or CdBr_2 , MAX phase could be easily converted into MXene terminated with Cl or Br (here is $\text{Ti}_3\text{C}_2\text{Br}_2$ as example in the figure). It should be noted that Cd may be formed during the etching process, which can be removed by adding HCl (or HBr). This is very different from the removal of Cu by Li et al. and Zhao et al., where APS or FeCl_3 are needed. The reason for such difference could be ascribed to the intrinsic different properties of Cd and Cu. Obviously, using HCl or HBr to remove Cd will yield CdCl_2 or CdBr_2 , which can be recovered for recycle use. Owing to the high reactivity of Ti-Cl and Ti-Br bonds, the MXenes terminated with Cl or Br surface groups can be easily converted to other groups. For convenience, the cases reported in their work was also summarized in Table 2.¹²²

HF etching, fluoride salt plus HCl etching, electrochemical etching, and hydrothermal etching are belonged to wet-chemical etching. Wet-chemical processes usually result in high yield of MXene products, which may remain the method of choice for large-scale manufacturing. Meanwhile, wet-chemical process allows for flexible selecting etching reagent and condition, which has discussed above. Different from wet-chemical etching process, molten salt etching usually yield MXene product with only one type of termination groups. Molten salt etching method shares the advantages of single thermal process, flexible choosing salt.

Table 2. Summary of samples prepared via molten salt etching process in ref ¹²²

Original MXene	Molten salt system	Exchange reagent	Temperature (°C)	Target MXene
$\text{Ti}_3\text{C}_2\text{Br}_2$	CsBr-KBr-LiBr	Li_2Te	300	$\text{Ti}_3\text{C}_2\text{Te}$
$\text{Ti}_3\text{C}_2\text{Br}_2$	CsBr-KBr-LiBr	Li_2S	300	$\text{Ti}_3\text{C}_2\text{S}$
$\text{Ti}_3\text{C}_2\text{Br}_2$	CsBr-KBr-LiBr	LiSe	550–600	$\text{Ti}_3\text{C}_2\text{Se}$
$\text{Ti}_3\text{C}_2\text{Cl}_2$	KCl/LiCl	Li_2O	550–600	$\text{Ti}_3\text{C}_2\text{O}$
$\text{Ti}_3\text{C}_2\text{Cl}_2$	KCl/LiCl	NaNH_2	300	$\text{Ti}_3\text{C}_2(\text{NH})$
$\text{Ti}_3\text{C}_2\text{Br}_2$	CsBr-KBr-LiBr	LiH	300	$\text{Ti}_3\text{C}_2\text{O}_2$
Ti_2CBr_2	CsBr-KBr-LiBr	LiH	300	Ti_2CO_2

Table 3. Comparison of various etching techniques in advantages and disadvantages

Etching method	Advantages	Disadvantages
HF etching	Suitable for many types of MAX. Mature process equipment and operating conditions for various MAX.	Hazardous HF needed. Excessive etching possible. The structure of layered structure may be destroyed. Long residual time (over 8 h). Further modification needed for application.
Fluoride salt and HCl etching	The surface, morphology, and chemical reactivity of MXene may be modified. Possible to further process MXene into a composite.	when the pH approaches neutral, results in spontaneous delamination. Lithium is a rare resource. AlF ₃ ·3H ₂ O impurity formed in the product.
Electrochemical etching	Operation condition is mild. Experimental setup is simple. <i>In-situ</i> activation possible.	Mass production is difficult. Efficiency is low. Potential should be precisely controlled.
Hydrothermal etching	Completely avoid using fluorine agent. High reaction rate leads to high efficiency. Low temperature (less 250°C). Mature equipment, process, and operating condition.	Easy to form oxide purity. Long residual time (usually over 6 h). Further activation needed.
Molten salt etching	Rend the surface of MXene hydrophobic. Termination groups are variable with molten salt applied. High solubility of various ionic compounds. Single thermal process. <i>In-situ</i> activation possible.	High temperature needed. Residual other metals usually can not be avoid. Salt recycling challenge. Lack of optimum process and mature equipment. Use of hash salt corrosive equipment.

However, this method usually suffers from the recycling salt, optimum/general process and mature equipment. Meanwhile, the equipment corrosion from the utilization of harsh salt should be further resolved. For convenience, Table 3 summarizes the merits and shortcomings of these etching techniques discussed above.

Besides advantages and disadvantages in operation, properties of materials are often dependent on the process of synthesis. MXenes are not exceptions. Generally, different methods lead to different termination groups in the final MXene products. In the aspect of thermoelectric application, MXenes obtained by HF and fluoride salt assisted etching usually deliver poor performance because the termination groups are F⁻, which is a strong electronegative element, implying a strong electron absorption ability. As a result, the electrons in-F atoms terminated MXene are usually trapped. For another thing, the presence of the-F atom would also prevent cations accessing into the MXene interspace, limiting the electron injection effect and providing low carrier concentration. For hydrothermal etching, it endows MXene with abundant -OH termination groups, which is hydrophilic and readily forms hydrogen bond with H₂O. Owing to the strong inter-affinity, chemically bonded H₂O is difficult to remove, which hinders the thermoelectric performance of MXene. For electrochemical etching, Ti in MXene easily react with electrolyte leading to accessive etching, yielding TiO₂ which is located at the edge of MXene sheets. As a result, the carrier transport between the MXene sheets may be prevented. As for molten salt etching technique, it inherently requires a high temperature, which has risks of sintering MXene sheets. In addition, the residual metal elements (such as Cu, and Zn) is difficult to be distributed evenly, resulting in non-reproducibility of thermoelectric performance of MXene.

APPLICATION OF MXene BASED MATEIRALS IN THERMOELECTRIC FIELD

Thermoelectrics, capable of realizing mutual transformation of heat energy into electrical energy, are more preferred compared to other energy supply devices. Also thermoelectric devices gain several advantages which involve their high durability, robustness, scalable, and compact and neither contain any moving parts nor emit any harmful gases. The benefits of developing high performance thermoelectric materials/devices are many. On one hand, waste heat energy caused by fossil energy consumption is expected to be

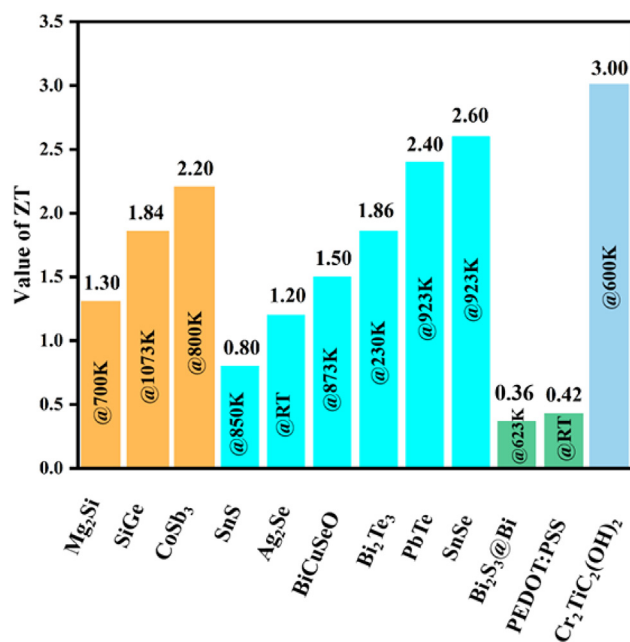


Figure 16. Comparison of figure of merit (ZT) achieved in various thermoelectric materials

SnS from ref. ¹²⁵, Ag₂Se from ref. ¹²⁶, Bi/Bi₂S₃ from ref. ¹²⁷, PEDOT: PSS from ref. ¹²⁸, Cr₂TiC₂(OH)₂ from ref. ¹²⁹, others from ref. ¹³⁰

recovered and converted into electric energy, which in turn reserves fossil energy resource and avoids some environmental concerning. It is confirmed that the utilization efficiency of the global primary energy consumption is only about one-third, and majority of the energy is lost through various inefficiencies. Among all kinds of energy wastes, the major loss has been confirmed to be waste heat. Furthermore, some advanced devices could be constructed, such as temperature sensors and fire warning devices. As we know that the thermoelectric effects depend on temperature differences between two legs. For some energy-intensive production industries, the working temperature is significant for safety. Also, the temperature above a critical value may lead to fire disaster. If a suitable thermoelectric device is connected to a warning light, the light may be turned on when the temperature is near the critical one. On the other hand, with the emergence of the flexible electronics and revolutionary changes in electronic devices, thermoelectrics are expected to charge/power these devices utilizing the intrinsic temperature differences between the human body and the environment avoiding using long wires, which are necessary in tradition external power supplies. In addition, utilizing thermoelectric modules make solar desalination feasible, which is preferred in obtaining drinkable water from seawater. ^{123,124}

As mentioned in the introduction section, MXene based materials have attracted increasing attention owing to their outstanding thermoelectric efficiency. Recent developments have renewed the interest in enlarging the family of MXenes and tuning the structure of MXenes to make them excellent electric conductivity but poor thermal conductivity. Furthermore, many MXene based composites possess stacked layers of a laminated structure with different molecule/ion intercalation have been reported to exhibit excellent thermoelectric properties. As outlined in Figure 16, we will discuss the thermoelectric applications of MXene based materials by classifying them into pristine MXene and MXene based composites including MXene/carbon, MX/polymer and MXene/inorganic.

Pristine MXene for thermoelectric application

Thermoelectric devices refer to the direct transformation of heat into electricity, making it an effective and reliable energy technology for microelectronics. Because of the low dimensionality, MXenes demonstrate significantly different electronic structure and magnetic properties as their corresponding MAX phases, endowing them great potential in thermoelectric energy harvesting. This has been verified by both theoretical predication and experimental research. In 2012, a series of MXenes, including Ti₂CO₂, Hf₂CO₂, Zr₂CO₂,

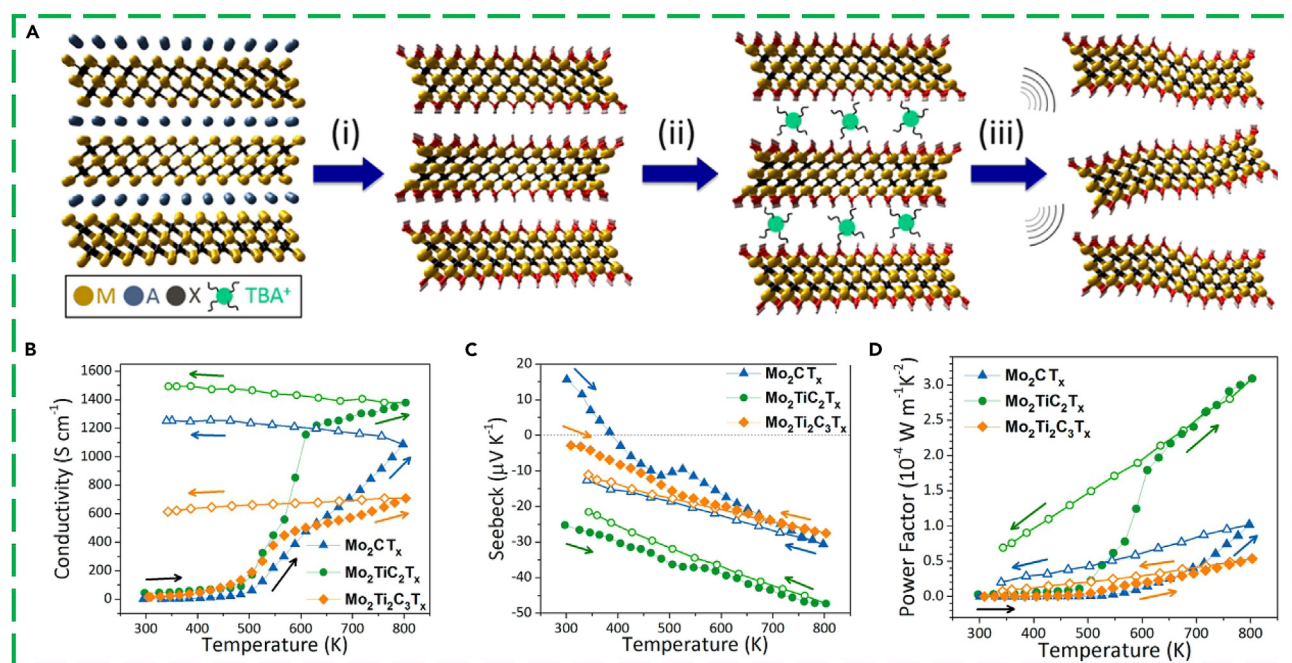


Figure 17. Mo-based MXenes preparation steps and electrical and thermoelectric properties

(A) Schematic illustration for the synthesis of MXene. (i) Selective etching of the A-element in the layered precursor materials, (ii) intercalation of organic molecules, tetrabutylammonium cations (TBA⁺), (iii) exfoliation of 2D MXene flakes by molecule exchange with water and ultrasonication.

(B–D) thermoelectric parameters of MXenes: (B) conductivity, (C) Seebeck coefficient, and (D) power factor. Reproduced from ref. ²¹ with permission. Copyright 2017 American Chemical Society.

Sc₂CF, Sc₂C(OH)₂, and Sc₂CO₂, were expected to possess semiconductor character with band gaps between 0.24 and 1.8 eV by Khazaei et al. using a set of first principle calculations.¹³¹ In 2014, a later calculation study revealed that Mo₂CF₂ (with fluorineterminated surface) have superior thermoelectric power factor among the other 35 different functionalized M₂XT_x MXene systems.¹³² With time passing, experimental evidence came to accumulate. In 2017, Kim et al. measured the electric and thermoelectric properties of three compositions of Mo-based MXenes (Mo₂CT_x, Mo₂TiC₂T_x, and Mo₂Ti₂C₃T_x). As displayed Figure 17A, the preparation of these Mo-based MXenes involves three steps. Initially, the corresponding MAX phases (Mo₂Ga₂C, Mo₂TiAlC₂, and Mo₂Ti₂AlC₃) were etched by HF to remove Al atoms. By washing with deionized water several times, multilayer MXenes (HF-etched powders) can be gained. Afterward, the multilayer MXenes were treated with tetrabutylammonium hydroxide (TBAOH), which leads to exfoliation of 2D MXene suspensions. Meanwhile, the tetrabutylammonium cation (TBA⁺) may be intercalated between the negatively charged MXene sheets, followed by further washing and sonication. The authors further checked the thermoelectric properties of three Mo-based MXenes. As shown in Figures 17B–17D, the electrical conductivity of all three Mo-based MXene papers varied with the change of temperature. In particular, they are resistive in the pristine state near room temperature, whereas there is a rapid increase of their electrical conductivity during the first heating cycle. This phenomenon could be ascribed to the loss of water molecules, which leads to a gradual enhancement of the conductivity at low temperatures (300–500 K). If the temperature continues to increase, owing to the formation of graphite from the thermal decomposition of TBA⁺ intercalant at around 500–600 K, the onset of rapid conductivity increase sharply. This is well in accordance with the reported thermal decomposition temperature of TBA⁺ intercalant in graphite, which is around 480 K. It is well known that a high temperature usually leads to a high graphitization of carbon, which is expected to further increase the electrical conductivity. Expectedly, the conductivity really increases when the temperature is above 600 K. However, the increase rate is very slow. This observation can be attributed to the decomposition of remaining TBA⁺ and the possible thermal-induced loss of surface termination groups. The variation of electrical conductivity with temperature was further confirmed by TGA with DSC and XRD. As for the seebeck coefficient, one can see from Figure 17C that all three MXenes exhibit negative values of the Seebeck coefficients, indicating n-type behavior. In contrast to the electrical conductivity, no drastic transitions on temperature are observed for the Seebeck coefficient, whereas only a

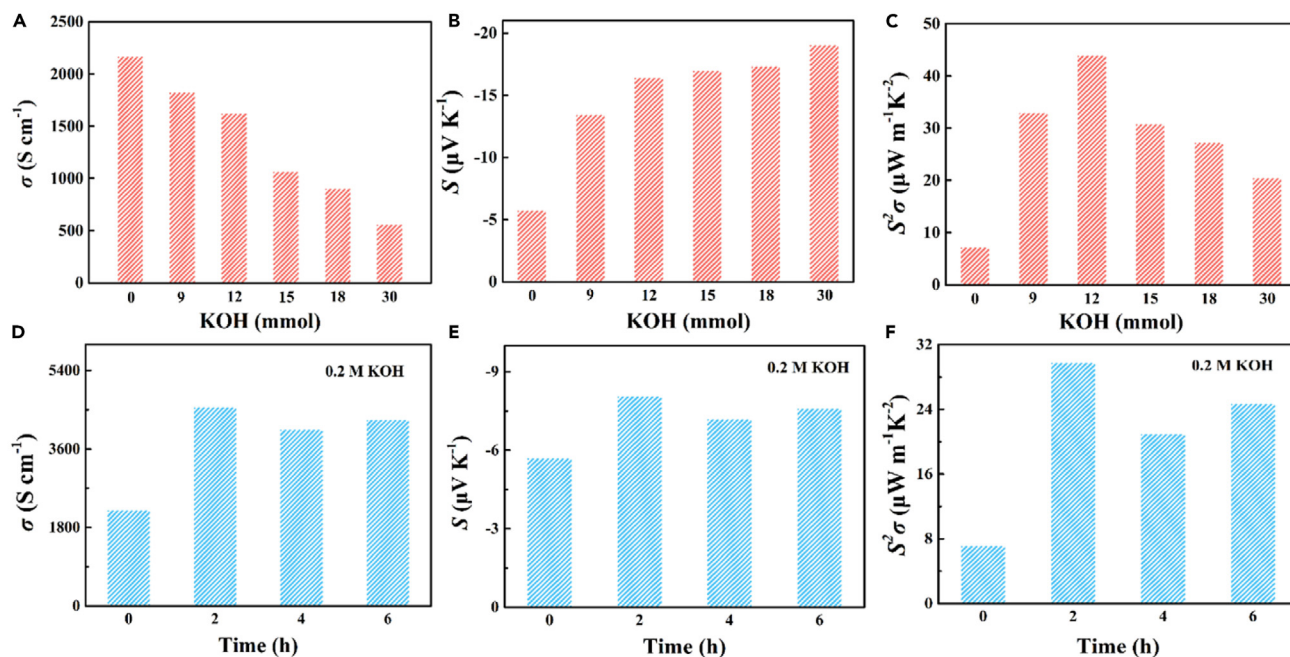


Figure 18. Effect of surface terminate modification on the thermoelectric performance of $Ti_3C_2T_x$

(A–C) concentration of KOH.

(D–F) hydrothermal time. Reproduced from ref. ¹³³ with permission. Copyright 2020 Elsevier.

slow change during the first heating cycle is observed. Such result in turn verified that the reason for the rapid increase in the electrical conductivity above ~ 500 K is likely corresponded to the enhanced electrical network between MXene nanosheets rather than irreversible changes of each MXene flakes. In particular, during the temperature of 500–550 K, a trend of increasing Seebeck coefficient was observed for Mo_2CT_x samples, revealing an interesting transition from p-type to n-type on thermal annealing.²¹

As mentioned in section 1, MXenes are usually prepared from selective etching A atoms from their parent MAX. The etching process as well as the post treatment process has significant impact on the performance of the final MXenes. Liu et al. have performed a systematic investigation on the influence of post hydrothermal treatment, including the acidity of the medium, treating time and the alkali resource on the thermoelectric performance of $Ti_3C_2T_x$. By treating $Ti_3C_2T_x$ with different electrolytes, different termination groups may be obtained. In their research, KOH, NaOH, $NH_3 \cdot H_2O$ and KCl at different concentrations were used as treating agent. They found that the effects of the treating agent are complicated. Both the concentration and treating time are crucial for the final performance. Take KOH as an example; the conductivity of the final $Ti_3C_2T_x$ decreased with the increase of KOH concentration, whereas the Seebeck coefficient increased (Figures 18A–B). As for the power factor ($S^2\sigma$), the modified MXene film displayed a high power factor of $44.98 \text{ mW m}^{-1} K^{-2}$ at room temperature (Figure 18C). Once the concentration of KOH was set at 0.2 M, the treating time of 2h was verified to be best to given the highest conductivity and Seebeck coefficient (Figure 18D–18E). The sample obtained at the treating time of 2 h supplies high conductivity and Seebeck coefficient; thus, the highest power factor was obtained by treating $Ti_3C_2T_x$ for 2h (Figure 18F). Besides the concentration of the post treatment agent and the treating time, in their work, Liu et al. further investigated the type of treating agent affecting the thermoelectric properties of $Ti_3C_2T_x$. They found that strong electrolytes provide a high electrical conductivity compared with weak electrolyte. Owing to the intercouple effect among the Seebeck coefficient and conductivity, the temperature effect is interesting. A high temperature leads to low conductivity whereas the Seebeck coefficient increased with the treating temperature. This phenomenon could be ascribed to the enhanced surface termination modification effect. At high temperatures, more -OH and -F functional groups were effectively removed, leading to the increase of the number of -O functional groups.¹³³ By first-principle calculations and Boltzmann theory respectively, Omube et al. predicted that Yttrium carbide MXenes (Y_2CT_2 , T = F, Br, OH, H) attain high and moderate figures of merit and Seebeck coefficients. Particularly, Y_2CH_2 was expected to have the

largest value of $ZT = 0.97$, which can be compared to 10% Carnot cycle efficiency.¹³⁴ Recently, by organic molecule intercalation and thermal treatment, Huang et al. demonstrated that $\text{Mo}_2\text{TiC}_2\text{T}_x$ and Nb_2CT_x MXenes could be controlled into n- and p-type, respectively. The thermoelectric power factor of $\text{Mo}_2\text{TiC}_2\text{T}_x$ and Nb_2CT_x MXenes was shown to be 13.26 and 11.06 $\mu\text{W}/(\text{mK}^2)$ at room temperature, respectively. In this work, they further designed and fabricated an all-MXene flexible and integrated thermoelectric nanogenerator by combing $\text{Ti}_3\text{C}_2\text{T}_x$ MXene as a contact electrode. The fabricated thermoelectric nanogenerators using 20 p-n units could produce an output voltage and power of 35.3 mV and 33.9 nW, respectively, under a temperature difference of 30°C.¹³⁵

As theory predicted, the termination groups on the surface of the MXene may determine the nature of MXene to some extent. For example, the intrinsic Cr_2TiC_2 (without termination groups) is n-type semiconductor, whereas Cr_2TiC_2 with -F and -OH are p-type semiconductor. Obviously, such different properties are expected to give different thermoelectric properties. Combining the first-principles calculations with semiclassical Boltzmann theory in BoltzTraP code, and the linearized phonon Boltzmann transportation equation (BTE) using third-order IFCs as the input in ShengBTE code, Jing et al. discovered that ordered $\text{Cr}_2\text{TiC}_2\text{T}_2$ MXenes (T = -F or -OH) are promising TE materials with high ZT values. As shown in Figure 19A, the ZT values of hole-doped $\text{Cr}_2\text{TiC}_2(\text{OH})_2$ and $\text{Cr}_2\text{TiC}_2\text{F}_2$ are much higher than that of Cr_2TiC_2 . In particular, $\text{Cr}_2\text{TiC}_2(\text{OH})_2$ delivers high ZT value up to 3.00 at 600 K and 2.58 at room temperature, which are comparable to those the very recently reported record-high ZT value of SnSe.¹³⁶ A further thermoelectric conversion efficiency revealed that p-type $\text{Cr}_2\text{TiC}_2(\text{OH})_2$ and $\text{Cr}_2\text{TiC}_2\text{F}_2$ are found to be higher than that of n-type Cr_2TiC_2 . The different thermoelectric properties of these $\text{Cr}_2\text{TiC}_2\text{T}_2$ MXenes are absolutely ascribed to the surface functionalization, which plays the crucial role in both the electronic structure and lattice phonon dispersion in MXenes. In general, to get better thermoelectric performance, the MXenes are expected to deliver semiconducting electronic structure with relatively high electrical conductivity and very small lattice conductivity. Despite significantly reducing the lattice thermal conductivity by introducing the large size of the surface functionalization group, the electronic band gap and the characteristics of band are determined both by transition metals and surface groups.¹²⁹

Besides directly providing thermal energy to create temperature differences between two sides of thermoelectric materials, there are some additional strategies to create temperature difference, such as absorbing microwave, sunshine, and electromagnetic wave. It has been demonstrated that MXene possess a 100% internal light-to-heat conversion efficiency. Based on electromagnetic energy conversion mechanism, He et al. designed a thermoelectric generator driven by electromagnetic wave, as depicted in Figure 20A. In this thermoelectric generator, the composites consisting of 80 wt % D- $\text{Ti}_3\text{C}_2\text{T}_x$ with a thickness of 1 mm are coated on the surface of the aluminum alloy. P-type and N-type semiconductors are connected at each end. The choice of the aluminum alloy has several advantages. For one thing, aluminum alloy has a high thermal conductivity, which are benefit to transfer heat rapidly to P-type and N-type semiconductors, reducing heat loss. For another thing, the electrical nonconductivity of the aluminum alloy prevents electron transmission between P-type and N-type semiconductors. Based on the Seebeck effect, a circuit between P-type and N-type semiconductors will be formed owing to the the temperature difference, which will be suitable for power supply of low power electric devices. As a consequence, the electromagnetic energy is converted into power energy. Figure 20A shows the relevant operational mechanism. Figures 20C–20F show the thermoelectric performance of the device. One can see from Figure 20C and d that the electrical conductivity of the composite is much dependent on the mass ratio of D- $\text{Ti}_3\text{C}_2\text{T}_x$. The higher mass ratio of D- $\text{Ti}_3\text{C}_2\text{T}_x$ provides a higher electrical conductivity. The composite containing 80 wt % D- $\text{Ti}_3\text{C}_2\text{T}_x$ delivers a high electrical conductivity up to 0.6 S m^{-1} . The conductivity mechanism is mainly attributed to the conductive network as shown in the inset of Figure 20D. Meanwhile, the distance among D- $\text{Ti}_3\text{C}_2\text{T}_x$ is usually related to the D- $\text{Ti}_3\text{C}_2\text{T}_x$ concentration. A smaller may be obtained at a high D- $\text{Ti}_3\text{C}_2\text{T}_x$ concentration, promoting the electron transportation. As a result, the higher the D- $\text{Ti}_3\text{C}_2\text{T}_x$ concentration, the greater is the the conductivity. In addition, the conduction loss (ϵ''_c) and polarization loss (ϵ''_p) of D- $\text{Ti}_3\text{C}_2\text{T}_x/\text{wax}$ composites were further studied. As shown in Figure 20E and f, both ϵ''_c and ϵ''_p of D- $\text{Ti}_3\text{C}_2\text{T}_x/\text{wax}$ composites were dependent on the frequency. In particular, a higher frequency leads to a lower ϵ''_c and ϵ''_p . This result is ascribed to the definition that ϵ''_c and frequency are inversely proportional to each other. Unexpectedly, when the D- $\text{Ti}_3\text{C}_2\text{T}_x$ concentration is below 40 wt %, a zero value of ϵ''_c is observed. As for ϵ''_p of D- $\text{Ti}_3\text{C}_2\text{T}_x/\text{wax}$ composites, owing to the polarization no obvious relaxation peaks were observed.

Besides electromagnetic wave, light irradiation is also capable to generate heat. Under temperature degradation, ions may also move toward a certain direction. Inspired by this, Hong et al. developed a subnanometer ion

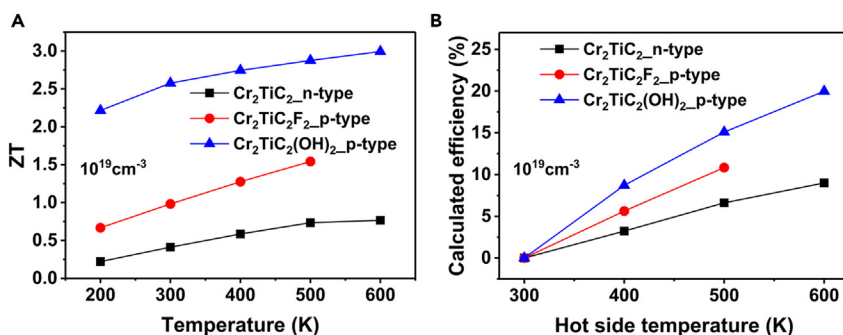


Figure 19. Thermoelectric figure of merit (ZT) and TE conversion efficiency for Cr₂TiC₂ and Cr₂TiC₂T₂ (T = -F and -OH)

(A) ZT value between 200 and 600 K and (B) thermoelectric conversion efficiency in the same temperature range. Reproduced from ref. ¹²⁹ with permission. Copyright 2019 American Chemical Society.

channels, converting external temperature changes to electric signals via preferential diffusion of cations under a thermal gradient. The device configuration was schematically illustrated in Figure 21A. The device is consisting of two Ag/AgCl electrodes which are connected by a polymer electrolyte containing arrays of MXene channels and cations and anions. On one side (position 1 in the figure) the light irradiation was utilized to induce high temperature. The temperature gradient and derived photothermal voltages may allow the transport of ions across the MXene channels. As revealed by Figure 21B, the temperature gradient increases with increasing the light intensity. Moreover, prolonging the light irradiation time can also provide a temperature gradient, leading to a proportional open-circuit voltage (ΔV). As a result, a positive ionic Seebeck coefficient will be yielded. Owing to the rapid photothermal heating of nanoconfined fluids, an instantaneous thermo-osmotic motion is expected to occur. To check the effect of light irradiation source, the position of light and the intensity of the light were further investigated. The result was displayed in Figure 21C, the light irradiation position has no impact on the

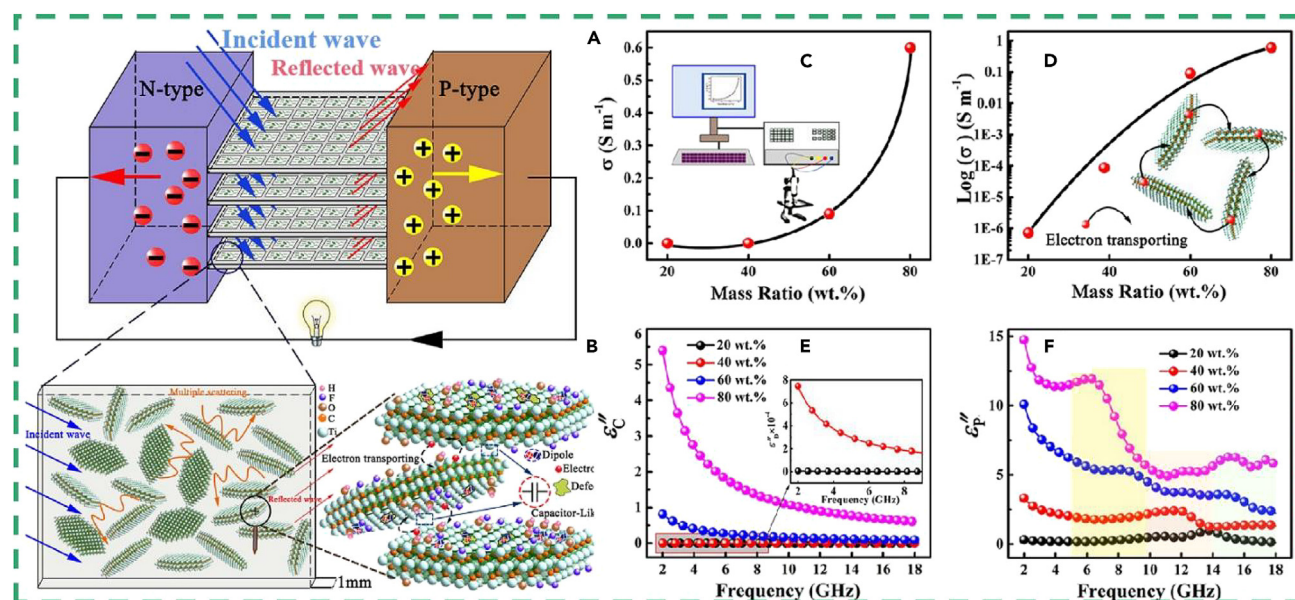


Figure 20. Thermoelectric properties of D-Ti₃C₂T_x composites for thermoelectric generators

(A) Schematic illustration of a thermoelectric generator driven by electromagnetic wave.

(B) Relevant operational mechanism.

(C and D) DC conductivity (σ) and (d) log₁₀ DC conductivity (σ) vs. mass ratio of D-Ti₃C₂T_x/wax composites. The inset of (C) shows Keithley 4200-SCS semiconductor characterization system. The inset of (D) is the schematic diagram of electron transportation.

(E) Conduction loss (ϵ''_c) and (F) polarization loss (ϵ''_p) for D-Ti₃C₂T_x/wax composites. Reproduced from ref. ²³ with permission. Copyright 2019 American Chemical Society.

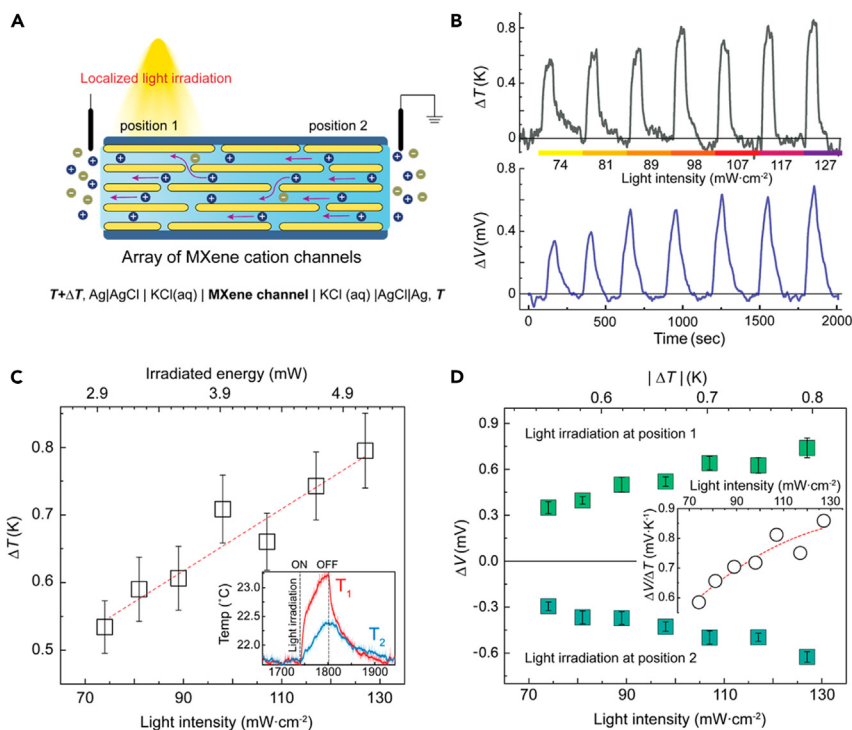


Figure 21. Light irradiation induces ion transport in MXene to generate heat

(A) Schematic illustration for the constructing a thermoelectric device using light irradiation as a heat source.

(B) Time-dependent temperature gradient and photothermal voltages when irradiated at position 1. The light is irradiated for 60s at each light intensity.

(C) Proportional increment of temperature gradient at elevated light intensity. Inset shows time-dependent temperature changes at positions 1 and 2, respectively, under light illumination of 127 mW·cm⁻².

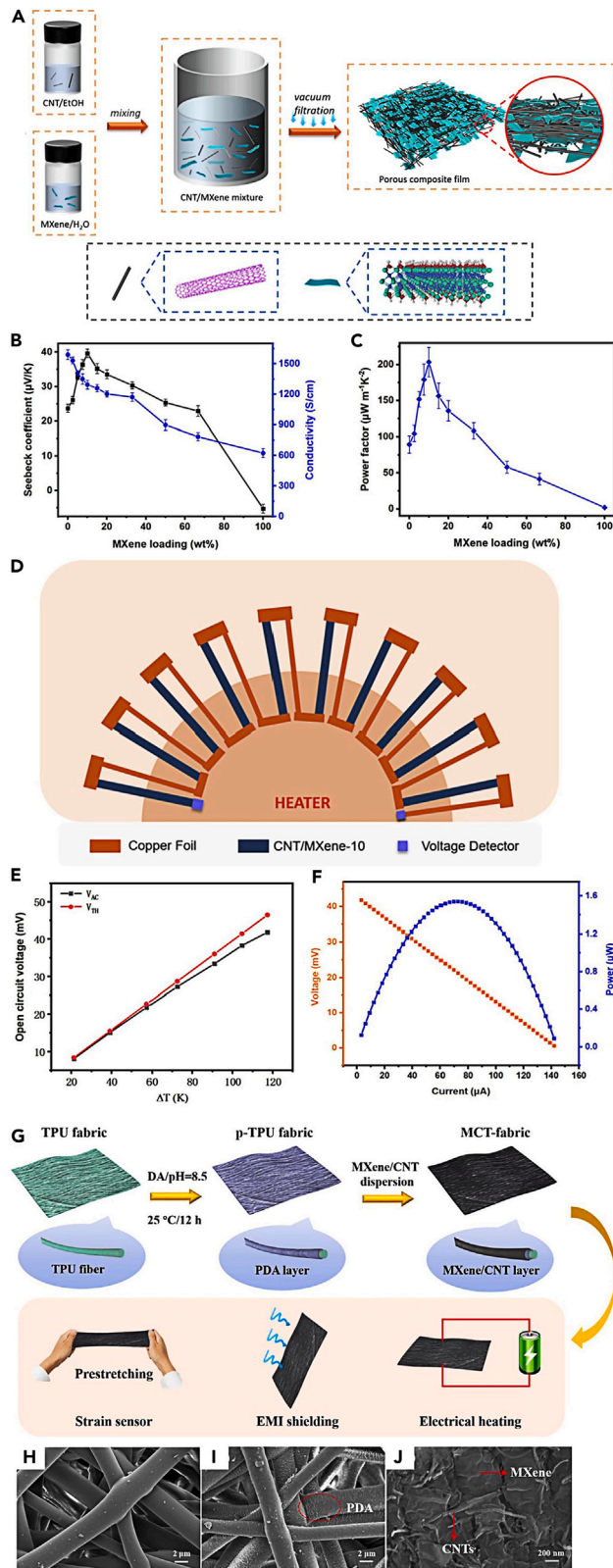
(D) Photothermal voltages under elevated light intensity at different irradiation positions. Inset displays the calculated ionic Seebeck coefficient from the photothermal voltages, independently of the irradiation positions. Reproduced from ref. ¹³⁷ with permission. Copyright 2023 American Chemical Society.

temperature gradient (ΔT), which increases proportionally to the energy of irradiated light. When varying light intensities, a stable thermal flux could be identified on condition that the MXene channel is locally irradiated. Obviously, this conductive thermal feature is responsible for driving the stable temperature difference across the interlayer water in the transverse cation channels. Under elevated light intensity, the voltage usually includes two fractions, thermal voltage and thermoelectric voltage. As shown in Figure 21D, this thermoelectric device produces both the different polarity of the thermal voltage and the ionic thermoelectric voltage. The former is dependent on the irradiation position. The latter shows a proportionate rise under elevated light intensity.¹³⁷

Besides above highlighted examples, there have been some more achievements gained in developing MXene based thermoelectric devices. Table 4 listed the thermoelectric properties of recent reported pristine MXene, which further evidenced that MXene is a promising thermoelectric material. It should be noted

Table 4. Thermoelectric properties of some representative MXene based thermoelectric devices reported during the past years

MXene	Test condition	Seebeck coefficient	Thermal conductivity	ZT value	Reference
Ti ₂ CO ₂	300 K	750 $\mu V/K$	18.42 W/mK	0.98	Sarikurt et al. ¹³⁸
Mo ₂ C/Mo ₂ Ti ₂ C ₃	room temperature	308 $\mu V/K$; -25 $\mu V/K$	0.37 W/mK; 0.45 W/mK	1.7×10^{-5} ; 2.6×10^{-4}	Park et al. ²⁵
Sc ₂ C	900 K	300 $\mu V/K$	4 W/mK	0.5	Kumar et al. ¹³⁹
Ti ₂ CO ₂	300 K	-	43.95 W/mK	-	Guo et al. ¹⁴⁰
Ti ₃ C ₂ Tx	5.8 K (ΔT)	78.4 $\mu V/K$	-	-	Xu et al. ¹⁴¹



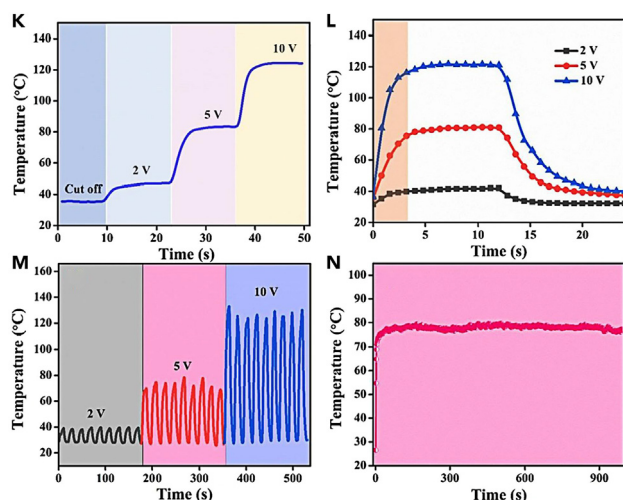


Figure 22. Preparation of swcnts /MXene composites and thermoelectric parameters

(A) Schematic illustration for the synthesis of SWCNT/MXene composite. Temperature-dependent Seebeck coefficient and electrical conductivity (B), and power factor (C) of SWCNT/MXene composites with different wt % MXene.

(D) Schematic diagram of the thermoelectric device consisting of 10 couples of legs.

(E and F) Open circuit voltage as a function of temperature gradient and (F) Voltage–current and power–current curves. Reproduced from ref. ¹⁴⁶ with permission. Copyright 2022 Elsevier.

(G) Schematic illustration for the preparation of multifunctional MCT-fabric. SEM images of pristine TPU (H), p-TPU fabric (I), and MCT-fabric (J). Joule heating performance of MCT-fabric under gradient-increasing voltage (K). Cyclic heating-cooling performance of MCT-fabric cycles under a voltage of 2, 5 and 10 V (L and M). Long-term temperature-time curve of MCT-fabric at a voltage of 5 V for 1000 s (N). Reproduced from ref. ¹⁴⁷ with permission. Copyright 2022 Elsevier.

that some critical parameters, such as power factor, figure of merit (ZT) still have much space to improve compared to some traditional inorganic thermoelectric materials.

Although promising prospect, it should be pointed out that pristine MXene as thermoelectric materials suffers from several disadvantages. For one thing, instability of MXene to atmospheric oxidation in harsh environments or high temperatures is a significant concern. For another thing, the performance of MXenes should be further boosted for satisfying practical requirement. Finally, MXenes, possessing typical nature of ceramics, are usually fragile, so the mechanical stability should further be improved. In addition, for wearable devices, the flexibility is necessary. Thus, it is expected that more research on constructing flexible MXene based composite for thermoelectric application will be attractive.

MXene/carbon composites for thermoelectric application

Benefiting from their high charge carrier mobility, unique 1D electronic band structure, having both metallic and semiconducting tubes and ease processing, carbon nanotubes (CNTs) are one of the most promising flexible thermoelectric materials. Compared to polymers and inorganic semiconductors, CNTs provides a series of advantages, such as more versatility because of its excellent electrical conductivity, tunable thermopower by facile p- and n-doping, and light weightness. Great progress has been made in utilizing CNTs and their hybrid composites to construct thermoelectric devices because of their ease processability, scalability, and low density.^{142–145} Unfortunately, the thermoelectric properties of CNTs are currently restrained by their low Seebeck coefficient and high thermal conductivity. Recently, many groups are devoted to making composites with appropriate organic or inorganic materials, energy-filtering effect to improve the thermoelectric properties of CNTs by boosting Seebeck coefficient and decrease the thermal conductivity with little sacrificing of electrical conductivity. For example, Wei et al. prepared a series of three-dimensional (3D) hollow structured SWCNT/MXene films. Figure 22A demonstrate the synthetic process of SWCNT/MXene films, which is very simple because only a mechanical mixing of two solutions (CNT/EtOH and MXene/H₂O) is needed followed by vacuum filtration. Owing to the energy filtering effect at interfaces, the SWCNT/MXene composites are demonstrated to possess higher Seebeck coefficient compared to SWCNTs does. As demonstrated in Figures 22B and 22C, the thermoelectric parameters, such as Seebeck coefficient, electrical conductivity, and power factor

of SWCNT/MXene composites are much dependent on the mass loading ratio of MXene on the composite. At MXene loading of 10 wt %, SWCNT/MXene-10 possessed the highest thermoelectric performance. It is verified by calculation that the Seebeck coefficient and ZT value are about 2 times and 20 times higher than that of the neat SWCNTs, respectively. Figure 22D demonstrated the schematic photograph of a thermoelectric device based on the SWCNT/MXene-10, in which 10 legs of SWCNT/MXene-10 was used. The performance of the device was presented in Figures 22E and 22F. The open circuit voltage under actual test condition (V_{AC}) is demonstrated to be very close to the theoretically calculated values (V_{TH}). Moreover, a good linear relationship between the V_{AC} and the temperature difference was observed, which reached the maximum of 41.84mV at the temperature difference of 117.3 K. Significantly, the device delivered a high theoretical power (P_{TH}) of about 1.54 μ W at temperature difference of 117.3 K. By dividing the power output by area of the thermoelectric module (10 cm²), the power density of the device was calculated to be 0.15 μ W cm⁻².¹⁴⁶ Recently, Zhang et al. deposited the hybrid of Ti₃C₂T_x MXene and carbon nanotubes (CNTs) on polyurethane (TPU) non-woven fabric (MCT-fabric) via a dip-coating approach. Based on the synergistic MXene/CNTs conductive coating and pre-stretching induced ultrasensitive microcrack structure, the as-prepared MCT-fabric possesses several functions, such as strain sensor, superior EMI shielding effectiveness, and rapid Joule heating response. The synthetic procedure, characterization, and Joule heating performance of MCT-fabric were displayed in Figures 22G–22N.¹⁴⁷

In another work, Ding et al. constructed a series of composites consisting of MXene and SWCNTs with sandwich structure. As revealed by Figure 23A, the composite films possess the typically compact and well-aligned 2D layered structure by the composition of single-layer and few-layer. Such result is helpful to provide a higher electrical conductivity and lower thermal conductivity owing to the phonon scattering at the junction interface. In this work, the authors prepared sample with three structures, Ti₃C₂T_x-SWCNTs, Ti₃C₂T_x-SWCNTs-Ti₃C₂T_x (SWCNTs was located between two Ti₃C₂T_x layers), and SWCNTs-Ti₃C₂T_x-SWCNTs (Ti₃C₂T_x was located between two SWCNTs layers). Figure 23B presents the energy diagrams of these three composite structures. The band gaps in SWCNT and Ti₃C₂T_x are greatly different (4.13 eV and 3.90 eV, respectively), leading to ease forming a Schottky barrier between Ti₃C₂T_x and SWCNTs. The consequence was that the Seebeck coefficient of the composite is much higher than that of pristine SWCNTs. The increase of the Seebeck coefficient could be ascribed to the scattering off the low-energy carriers. Furthermore, the electrical conductivity is much dependent on the ratio of SWCNTs as well as the structure itself. In particular, for each structure the electrical conductivity decreased with increasing the mass ratio of SWCNTs. Of interest, at a given mass ratio of SWCNTs, Ti₃C₂T_x-SWCNTs-Ti₃C₂T_x shows the highest electrical conductivity. Figures 23C–23E presents the power factor of these composites when applied in thermoelectric devices. The results demonstrate that Ti₃C₂T_x-SWCNTs-Ti₃C₂T_x film with 50% SWCNTs generates a pretty sizable power factor. Compared to pristine Ti₃C₂T_x and SWCNTs, the value was boosted 26 times and 5 times, which was up to 77.9 μ W/(mK²).¹⁴⁸

Traditional thermoelectric devices suffer from several issues such as high cost and insufficient performance at ambient temperature, restricting their widespread applications. As a result, thermocells, also known as thermoelectrochemical cells or thermogalvanic cells, represent an alternative to convert low-grade waste heat into electrical energy. In particular, a thermocell is capable of convert body heat energy into electrical energy. The energy conversion in a typical thermocell relies on the thermoelectrochemical Seebeck effect. The voltages of thermocells reach the order of mV/K under room temperature. Recently, Wei et al. reported a ternary composite composed of Ti₃C₂T_x, SWCNT, and PANI (T-S-P), which can be easily prepared via a facile vacuum filtration method. The ternary T-S-P composite electrode showed notably improved thermoelectrochemical performance compared to the widely adopted noble platinum electrodes. Notably, the as-fabricated T-S-P electrode showed excellent catalytic activity for the temperature-dependent redox reactions. As displayed in Figure 24A, a square-shaped thermocell was assembled using the T-S-P ternary composite using two copper electrodes in contact with an electrolyte solution. Electricity may be created when the electrochemical redox potential is supplied by the temperature difference between two sides. For a given electrochemical reaction in this system it can be ascribed as below.



Moreover, owing to the good thinness, flexibility, and porosity, the ternary T-S-P composite electrode showed superior advantages when circumventing the electrolyte diffusion issue. In their work, a practical thermocell was further assembled, which is capable of powering electronics under the small temperature difference between

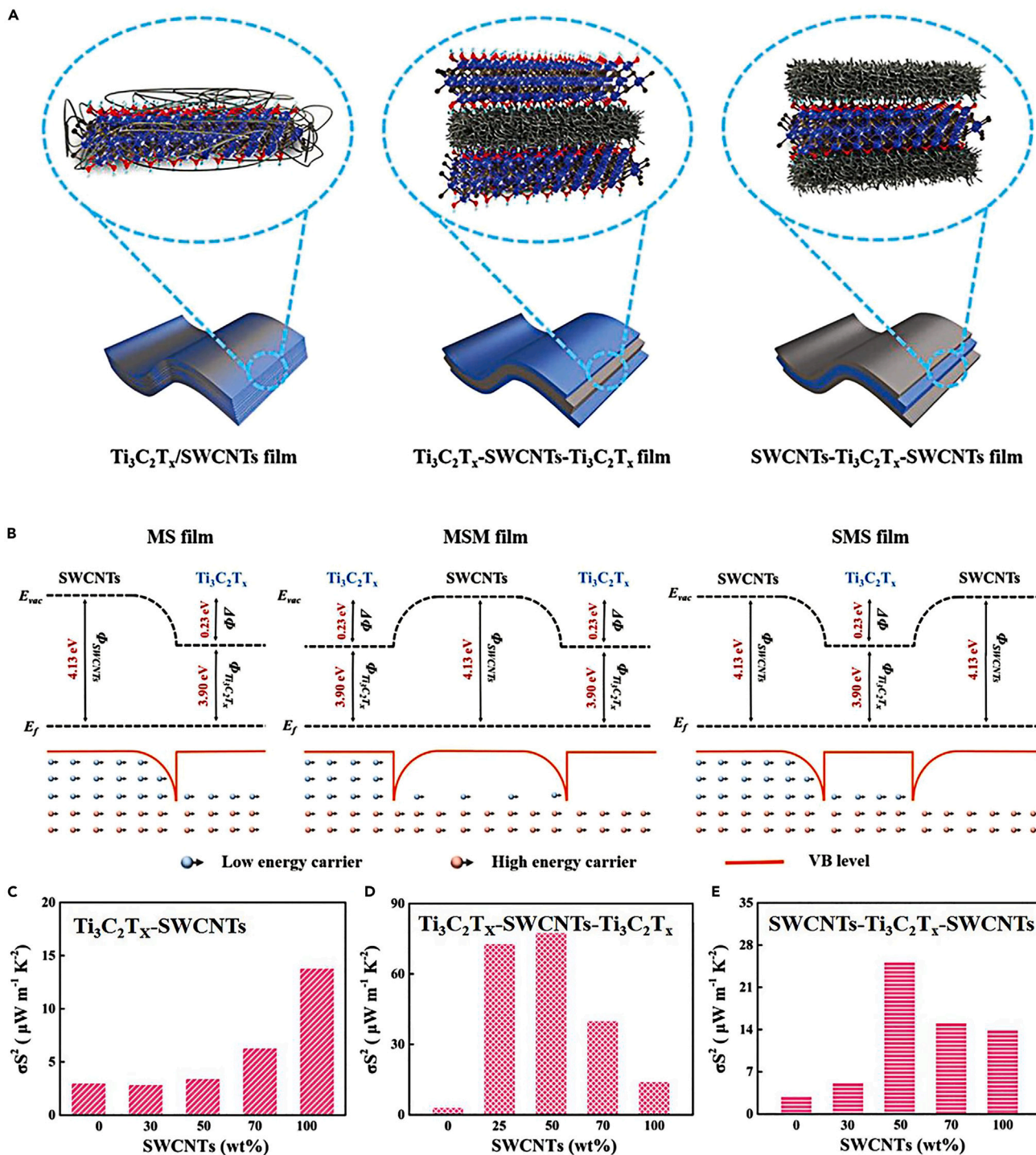


Figure 23. Thermoelectric properties of sandwich structured MXene/SWCNTs composites

(A) Schematic structures, (B) Energy diagrams, and (C ~ E) power factors of $\text{Ti}_3\text{C}_2\text{T}_x$ -SWCNTs, $\text{Ti}_3\text{C}_2\text{T}_x$ -SWCNTs- $\text{Ti}_3\text{C}_2\text{T}_x$, and SWCNTs- $\text{Ti}_3\text{C}_2\text{T}_x$ -SWCNTs. Reproduced from ref. ¹⁴⁸ with permission. Copyright 2020 John Wiley & Sons.

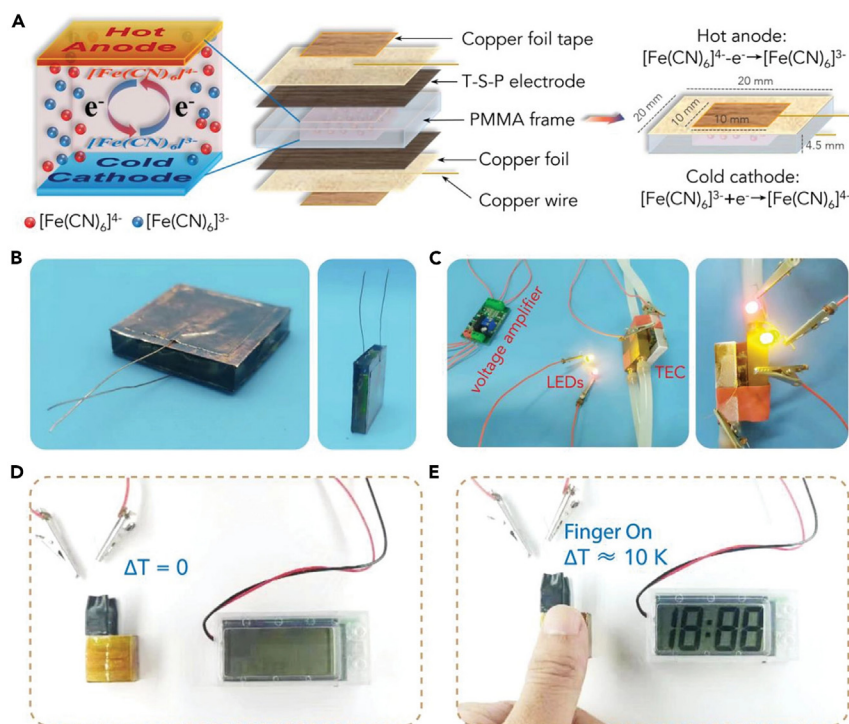


Figure 24. Preparation and thermoelectrochemical properties of $\text{Ti}_3\text{C}_2\text{T}_x$, Swcnts and PANI (T-S-P) ternary composites

(A) Schematic configuration of the square TEC based on T-S-P composite electrode.

(B) Optical images of the as-fabricated square TEC.

(C) Demonstration of using the square TEC to light up two LED bulbs under the temperature difference of 30 K with the assistance of a voltage amplifier.

(D and E) Demonstration of using the square TEC to power an electronic timer by harvesting human body heat. The timer was immediately powered on once the thumb touched one side of the square TEC. The applied temperature difference between the human body and the ambient environment was $\approx 10 \text{ K}$. Reproduced from ref. ²⁷ with permission. Copyright 2023 John Wiley & Sons.

human body and the ambient, as revealed in Figures 24B–24E. These results demonstrated that such T-S-P ternary composite have great potential in harvesting/converting body heat into electrical energy.²⁷

Graphene, which is composed of a monolayer of sp^2 hybridized carbon atoms, has also attracted intensive interests from broad areas of chemistry, physics, and materials science, among others. Interest in graphene's thermoelectric applications has engendered a large pile of publications and a speeding up of research pace.^{149–151} Literature investigation has evidenced that incorporating MXene into graphene is an effective strategy to further improve the thermoelectric performance, trying to make use of the inherently excellent electrical conductivity and superior charge transport properties of inorganic components. To date some progress has been achieved in thermoelectric properties of graphene/MXene composites. Saeidi-Javash et al. have reported the thermoelectric effect of $\text{Ti}_3\text{C}_2\text{T}_x$ -graphene nanosheet, which could be used to construct multifunctional bimodal sensors with integrated multiple sensing capabilities, including structural health monitoring, and wearable applications. Such a multifunctional sensor is based on determine the detecting the direct-current Seebeck voltage across the printed device pattern. The bimodal sensor based on the printed $\text{Ti}_3\text{C}_2\text{T}_x$ -graphene nanosheet was constructed through printing technique, as schematically presented in Figures 25A–25C, which includes four steps. The first two steps are exfoliation processes to prepare graphene and $\text{Ti}_3\text{C}_2\text{T}_x$ MXene, and the latter two steps are printing processes to deposit graphene and $\text{Ti}_3\text{C}_2\text{T}_x$ MXene onto the substrate. Figures 25D and 25E display the images of the printed bimodal sensors with vertical and horizontal strain sensors on polyimide substrates. The developed sensor demonstrates excellent sensing capability beyond conventional single-modality sensors besides providing prominent spatial resolution utilizing the microscale printed patterns. Figure 25F presents the thermoelectric voltages of six printed thermocouples (TC1-TC6), which increases linearly as a function of the

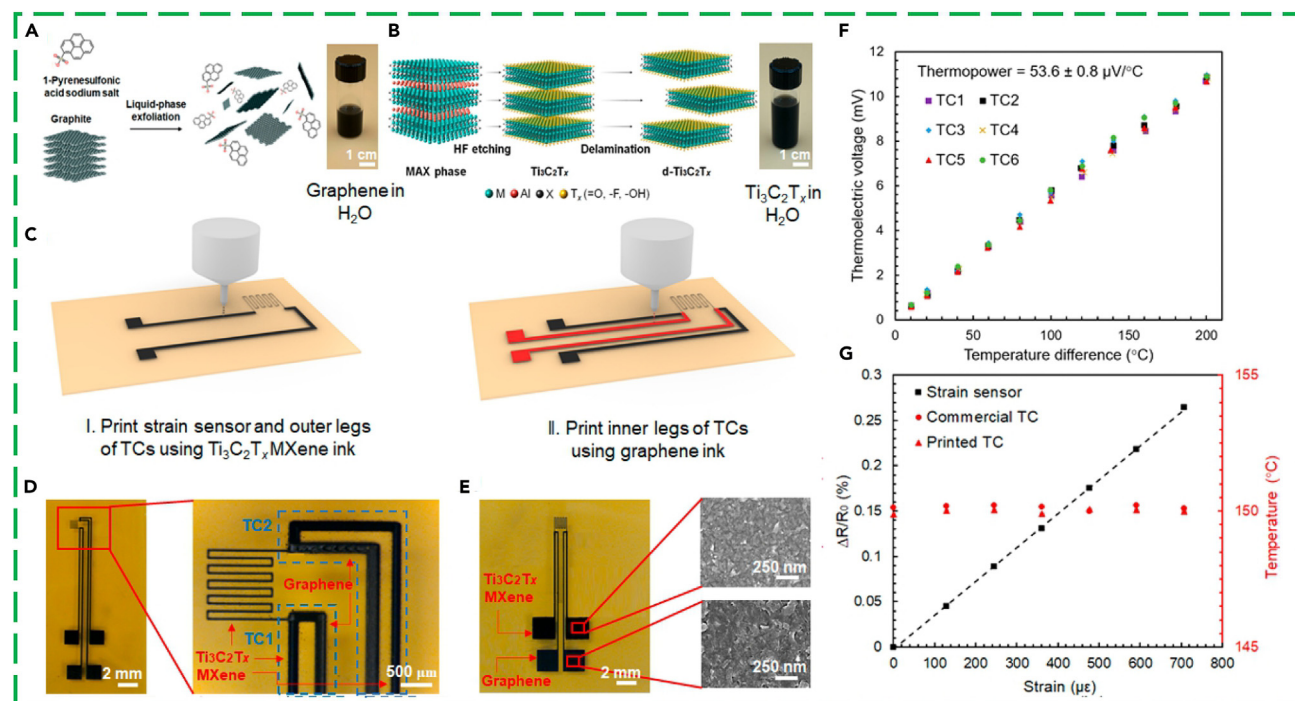


Figure 25. Preparation and thermoelectrochemical properties of $\text{Ti}_3\text{C}_2\text{T}_x$ -graphene nanosheets

(A and B) Liquid-phase exfoliation of graphite into graphene and (B) selective etching of Ti_3AlC_2 for the preparation of $\text{Ti}_3\text{C}_2\text{T}_x$ MXene.

(C) Schematic illustration of the bimodal sensor fabrication process flow including (I) printing the strain sensor and outer legs of the temperature sensors using $\text{Ti}_3\text{C}_2\text{T}_x$ MXene ink and (II) printing the inner legs of temperature sensors using graphene ink.

(D) Printed bimodal sensor with horizontal strain sensors.

(E) Printed bimodal sensor with vertical strain sensors and top view of SEM images of printed graphene and $\text{Ti}_3\text{C}_2\text{T}_x$ MXene films after annealing.

(F) Thermoelectric voltage of TC1-TC6 thermocouples.

(G) Simultaneous measurement of the strain and temperature at 150°C . Reproduced from ref. ¹⁵² with permission. Copyright 2021 American Chemical Society.

temperature difference. A maximum output voltage of 11 mV is obtained under ΔT of 200°C with a competitive thermopower output of $53.6 \mu\text{V}/^\circ\text{C}$ with ultrahigh accuracy and stability during both steady-state and transient thermal cycling tests. In addition, the sensor provided an outstanding platform to measure strain as shown in Figure 25G.¹⁵²

Compositing with carbon based materials, such as SWCNT, and graphene, supplies several merits to MXene. First, the carbon materials are characterized by high electronic conductivity, which is favorable for boosting the comprehensive thermoelectric performance of MXene. In addition, carbon materials can be molded into flexible, lightweight films that endow the final device with high specific energy density. Of significance, the introduction of carbon based materials would protect MXene from environmental oxidation, improving the reliability of MXene based thermoelectric devices.

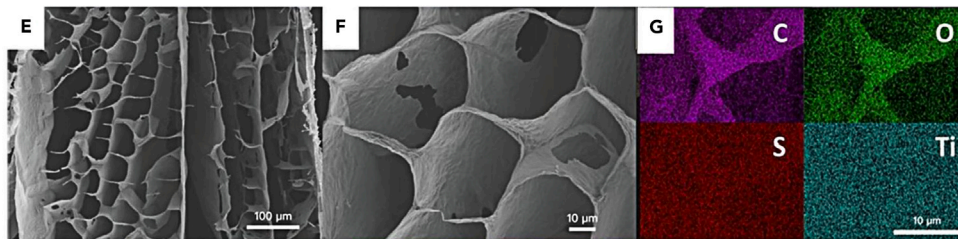
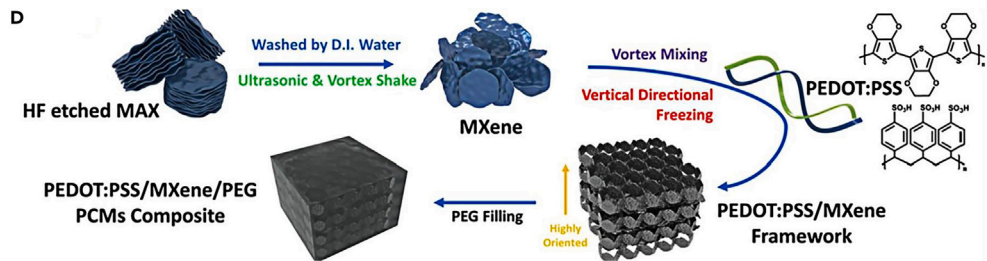
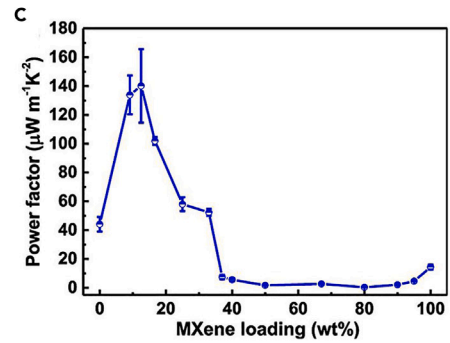
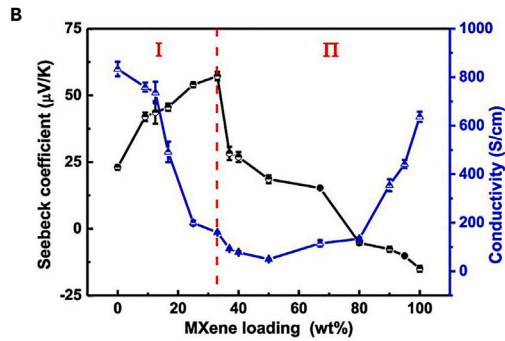
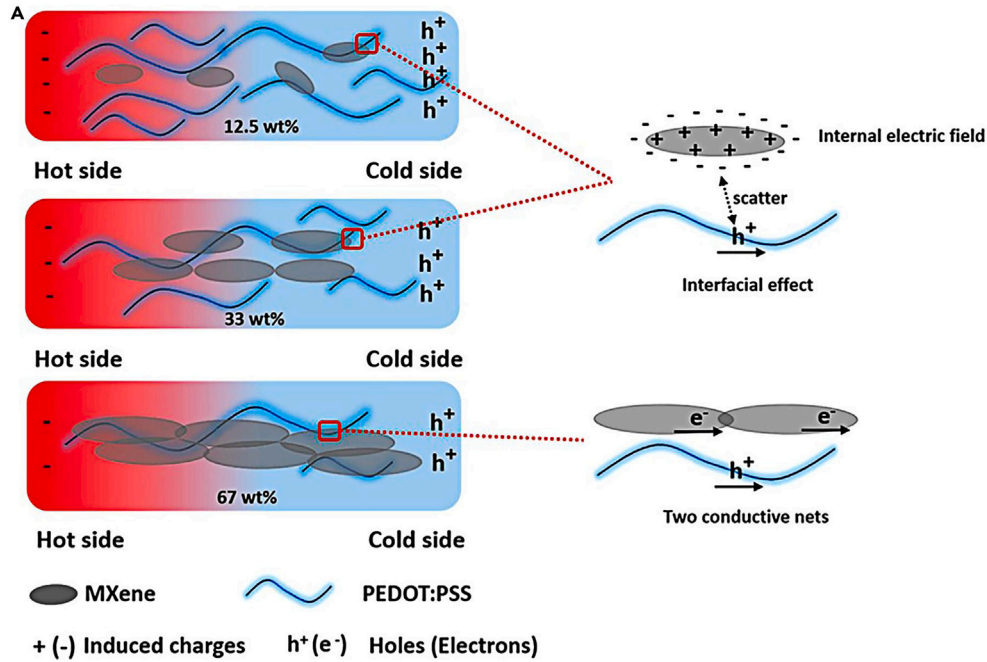
MXene/polymer composites for thermoelectric application

It has been demonstrated that composites consisting of p-type and n-type thermoelectric materials are expected to deliver high Seebeck coefficient, leading to an improved thermoelectric properties. Conducting polymers also possess some other advantages applied in electronic devices. The introduction of polymer containing composites to construct thermoelectric devices is expected to improve solution mixing, thermal conductivity, long-term stability, mechanical flexibility, and wear-ability, leading to a wide application.¹⁵³⁻¹⁵⁶ In particular, conducting polymers themselves possess excellent electrical conductivity, showing great prospect in boosting the performance of MXenes. Guan et al. prepared $\text{Ti}_3\text{C}_2\text{T}_x/\text{PEDOT:PSS}$ nanocomposites by drop casting a solution of PEDOT:PSS and MXene in water and DMSO. The prepared $\text{Ti}_3\text{C}_2\text{T}_x/\text{PEDOT:PSS}$ composites are capable of being applied to construct flexible and wearable thermal sensors, which could be connected to fingertips, and demonstrated real time and rapid thermal response

to cold or heat sources in a self-powered mode. It is well known that $\text{Ti}_3\text{C}_2\text{T}_x$ is typically belonged to n-type semiconductor, whereas PEDOT:PSS is p-type. By combining two such materials in one moiety, the electrons are readily to be transformed to PEDOT:PSS from $\text{Ti}_3\text{C}_2\text{T}_x$, as schematically illustrated in Figure 26A. As a consequence, an internal electric field will be created, preventing the movement of carriers with low energy. Meanwhile, a high Seebeck coefficient will be obtained though the electrical conductivity seems to be decrease. As presented in Figure 26B, the Seebeck coefficient of the composites increases with the lifting MXene loading when the loading amount of MXene is low. Such result can be ascribed the energy filtering because the Fermi level of MXene is lower than PEDOT:PSS by 0.2 eV Figure 26C provided the power factors of $\text{Ti}_3\text{C}_2\text{T}_x$ /PEDOT:PSS composites with different amount of $\text{Ti}_3\text{C}_2\text{T}_x$, among which an optimal power factor is 144–155 $\mu\text{W}/(\text{mK}^2)$.²⁴

In another work, Jin et al. prepared a composite consisting of MXene (etching MAX with HF) and PEDOT:PSS with zigzag modification of PEG (PEDOT:PSS/MXene/PEG) though vertical directional freezing and vacuum infiltrating, as illustrated by Figure 26D. The as-prepared PEDOT:PSS/MXene/PEG possesses a multi-hierarchical honeycomb like structure (Figure 26E and 23F). The EDS mapping (Figure 26G) undiscovered that the filling of PEG does not cause significant damage to the structure of PEDOT:PSS/MXene. The PEDOT:PSS/MXene/PEG composite integrates the function of heat management and EMI shielding into a single packaging material. The thermal conductivity of the PEDOT:PSS/MXene/PEG composite was verified to be dependent on the filling contents of PEG. As revealed by Figure 26H, the more PEG filled the lower thermal conductivity obtained. The thermal conductivity of PEDOT:PSS/MXene/PEG composites ranges from 0.30 to 0.36 $\text{W m}^{-1}\text{K}^{-1}$ as the absolute content of MXene increases, suggesting that a higher MXene content results in a higher heat exchange efficiency with outer by means of heat conduction. Figure 26I presents illustrates the components of a heterogeneous asynchrony photo-thermal-electric (PTE) conversion system. Figure 26J presents relationship among the open-circuit voltage (OCV) of the system and the temperature of the composite. One can see that the phase status changes of the composite have significant impact on the OCV of the conversion system. On initial illumination the OCV of composite ramps up rapidly. Followed by the initiation stage, the phase transition of PEG will occur, during which the OCV falls back. Once the phase transition stage is finished, the OCV signal shows a plateau. However, after the plateau stage, the system of the composite may reach heat buffer period, in which the quick drop off of the OCV for conversion system is observed. The minimum OCV occurs at the termination of illumination, which is determined to be around 5 mV. As a consequence, by combining MXene, PEDOT:PSS and PEG together, it is plausible to construct an integrated PTE conversion system in the form of heat converter and heat buffer, resulting in photo-voltaic transformation with a delay property.¹⁵⁷

Polyimide (PI) is a large family of common polymers which show promising application in a variety of fields. Recently, PI has been demonstrated to be a versatile modifying agent to adjust the performance of MXenes. Different from conducting polymers, PI may have no contribution to the electrical conductivity of MXenes, whereas PI is capable of lower the thermal conductivity of MXenes. As a consequence, by precisely controlling the structure and composition of MXene/PI composite, a desired thermoelectric performance may be obtained. Jiang et al. developed a dip-coating method to prepare PI/MXene aerogel (Figure 27A). As shown in Figure 27B, once a temperature difference between the two ends of the PI/MXene, the migration of electrons from the hot side to the cold side will occur. The thermoelectric voltage may increase up to 2.15 mV by increasing the temperature difference increasing. Such a thermoelectric voltage is enough to power a temperature recorder. The linear fitting function between the thermoelectric voltage and the temperature difference is plotted in Figure 27C. The stability of the PI/MXene temperature-sensor was also investigated in their work, which was demonstrated to be satisfied. In addition, when the temperature recorder is replaced with a fire alarm device (such as a warning light), the device may work well. As depicted in Figure 27D, when there is a fire near the the device, a temperature difference between the two side of PI/MXene may be provided. As a result, the fire alarm will provide information of on fire or off fire. As a warning device, the repeatable warn is an important parameter for practice application. As shown in Figure 27E, the trigger time of the first and fifth fire warning was 4.03 s and 2.98 s, respectively. Furthermore, in Jiang et al.'s work, they also investigated the effect of PAA on the fire-warning trigger time of PI@MXene (Figure 27F). The result showed that the increase number of PI skeleton was not conducive to forming the conductive pathway and hindered the electrons migration in PI@MXene. the fire warning trigger time gradually increased with the increase content of PAA in the product. In addition, the dip-coating times also have impact on the performance of PI/MXene. Increasing dip-coating times are expected to form more conductive pathways through coating more MXene nanosheet on the aerogels. As a result, a decreased trigger time of PI@MXene was obtained with increasing the dip-coating time (Figure 27G).¹⁵⁸



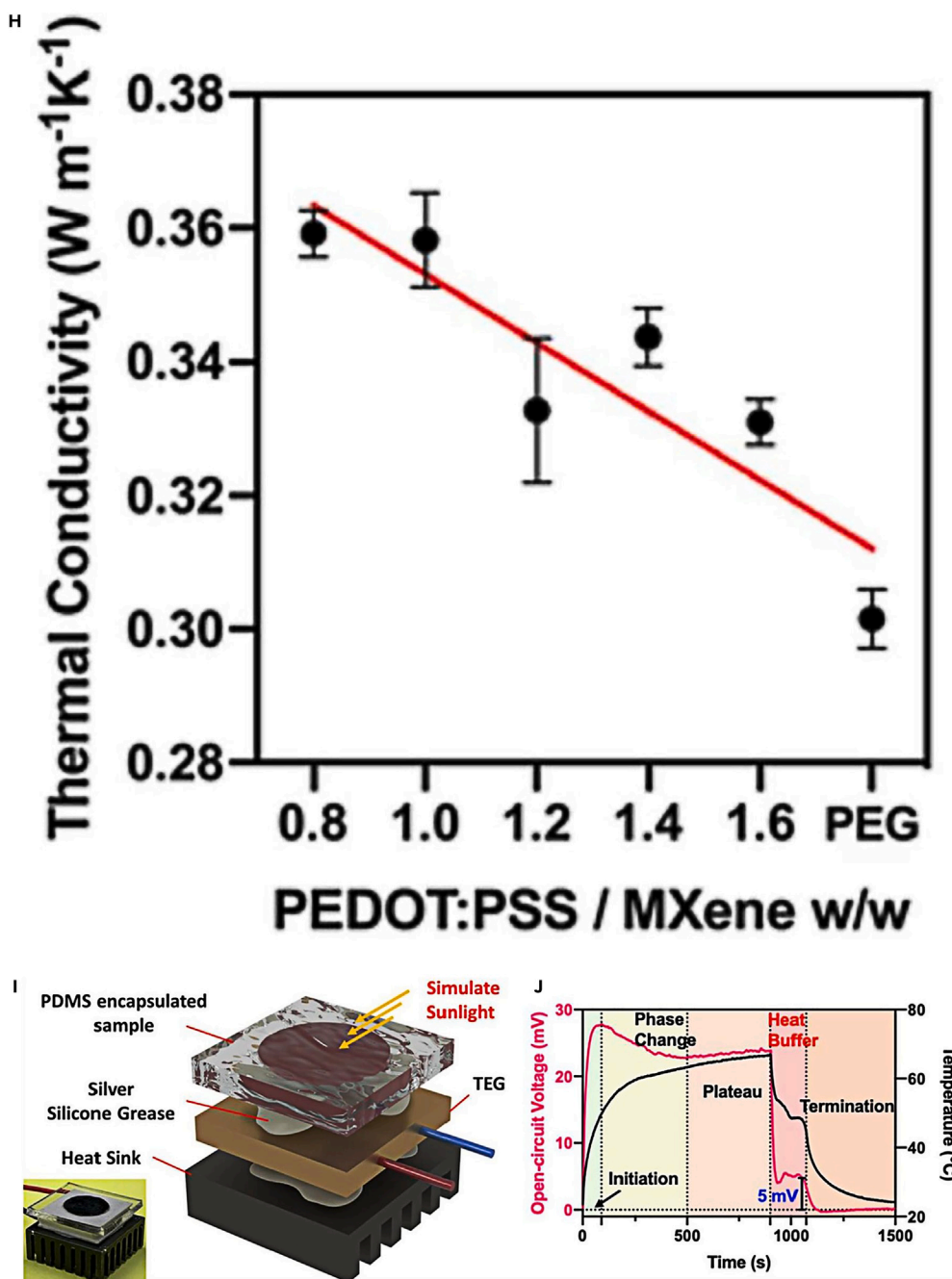


Figure 26. Preparation of $\text{Ti}_3\text{C}_2\text{T}_x/\text{PEDOT:PSS}$ nanocomposites

(A) Schematic illustration of the interface effect in $\text{Ti}_3\text{C}_2\text{T}_x/\text{PEDOT:PSS}$ composites.

(B and C) Seebeck coefficient and electrical conductivity, and (c) power factor of $\text{Ti}_3\text{C}_2\text{T}_x/\text{PEDOT:PSS}$ composites at different $\text{Ti}_3\text{C}_2\text{T}_x$ loading (wt %).

Reproduced from ref. ²⁴ with permission. Copyright 2020 American Chemical Society.

(D) Synthetic process of PEDOT:PSS/MXene/PEG PCMs composite.

(E and F) The inner morphologies of PEDOT:PSS/MXene (w/w = 1) framework.

(G and H) The EDS mapping results of PEDOT:PSS/MXene framework and PEDOT:PSS/MXene/PEG composite (H) The effect of PEG contents on the thermal conductivity of PEDOT:PSS/MXene.

(I) Illustration of real thermoelectric generator device based on PEDOT:PSS/MXene using sunlight as heat source.

(J) Time-dependent open-circuit voltage of the device. Reproduced from ref. ¹⁵⁷ with permission. Copyright 2022 Elsevier.

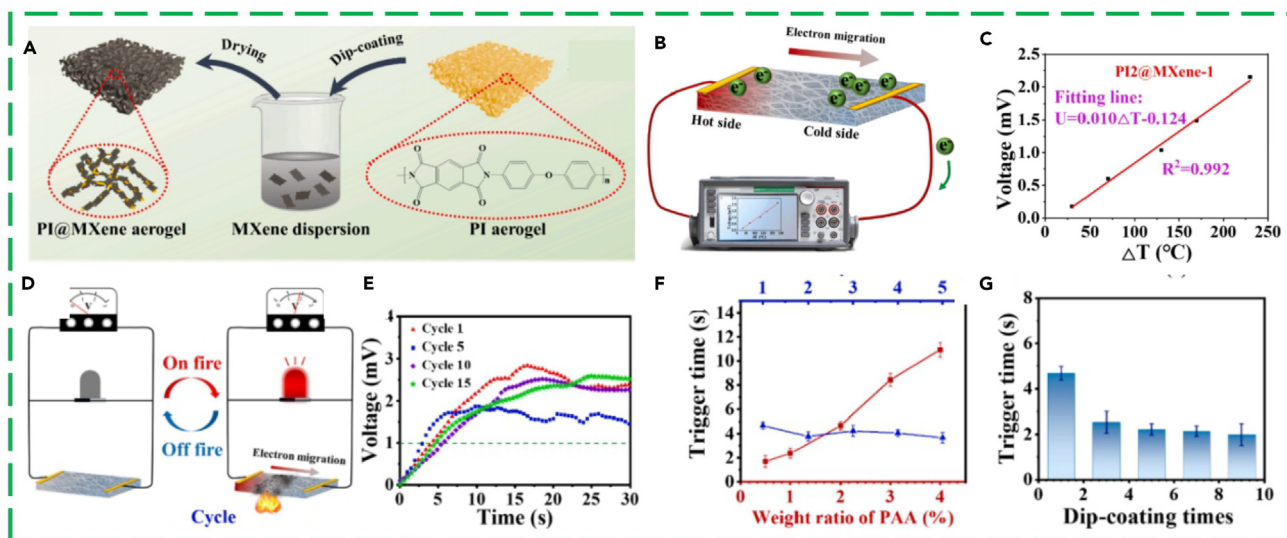


Figure 27. Polyimide (PI) compounded with MXenes to modulate thermoelectrochemical properties

(A) Schematic illustration for the preparation of PI@MXene aerogel composite.

(B) The diagram of a thermoelectric generator based on PI@MXene aerogel composite.

(C) Plot of voltage versus the temperature gradient.

(D) The diagram of working mechanism of the fire alarming device. The performance of the constructed fire alarm device: cycle performance (E), PAA ratio dependent trigger time (F) and dip-coating times dependent trigger time (G). Reproduced from ref. ¹⁵⁸ with permission. Copyright 2018 Elsevier.

Recently, Ma et al. developed a series of flame alarm wallpapers (FAWs) based on the composite of lignocellulose nanofibrils (LCNF) and $Ti_3C_2T_x$ MXene. The composite preparation process is similar to the work of Jiang et al., as displayed in Figure 28 a and b. The suspension of pre-synthesized $Ti_3C_2T_x$ MXene was mixed with LCNF suspension to form sandwich-like FAW which consists of MXene and LCNF with layered structures. It is noted that in their work ammonium polyphosphate (APP) was used to catalyze the char formation in the composite. Similar with Jiang et al.'s work, the sandwich-like composite can also assemble into fire alarm (Figures 28C and 28D). Once the temperature around the device is high enough to induce the flame, the device will shift to fire on state, providing fire alarming. In their work, they found that LCNF layer containing 15% APP delivers a trigger sensitivity and thermal oxidation capacity. Compared to traditional flame alarm device, LCNF/MXene based FAW shares a superior fire alarm response (0.32 s) and a continuous alarm signal (about 3073.0 s) as shown in Figure 28E. In addition, owing to the the good flexibility of LCNF, ideal repeatable warning performance, excellent heat insulation ability and strong char-forming properties in a fire. One of the disadvantages of this sandwich-like strategy lies in the lack of sensing temperature. To decrease the loss of the incident of flame, hopefully some effective measurements are expected to take for stopping the occurrence of fire disaster. Of course, new platforms for the construction of MXene-based multifunctional FAW might be offered, which is of great value in broadly addressing the fire hazard problem of traditional wallpapers. Recently, Zeng et al. developed an enhanced thermopower flame-retardant cotton fabric (HTE@CF) by dip-coating of MXene, tannic acid (TA), and calcium chloride ($CaCl_2$) via layer-by-layer assembly. Their investigation reveals that the HTE@CF possesses a high thermoelectric voltage of 3.72 mV, and the Seebeck coefficient more than $39.4 \mu V/K$. What's more, the HTE@CF displayed accurate temperature response and sensitive fire-warning performance. When being burned, the fire-warning system may be triggered within 3 s. Meanwhile, the limiting oxygen index (LOI) of HTE@CF was determined to be as high as 35.3%. Significantly, HTE@CF preserved stable structure even when exposed to the flame for 60 s. These results demonstrated outstanding flame retardancy of HTE@CF. Furthermore, the high conductivity of MXene and $CaCl_2$ endowed HTE@CF good piezoresistive sensing capability.¹⁵⁹

Considering the thermoelectric characteristic and excellent conductivity of MXene nanosheets, Wang et al. constructed a high fire safety cotton fabric (denoted as MXene/CCS@CF) by coating MXene nanosheet and carboxymethyl chitosan (CCS) via an eco-friendly layer-by-layer assembly method. The as-prepared MXene/CCS@CF exhibits temperature sensing, fire-warning, piezoresistivity, and Joule heating performance. When utilized to construct a temperature sensor, the MXene/CCS@CF yields outstanding

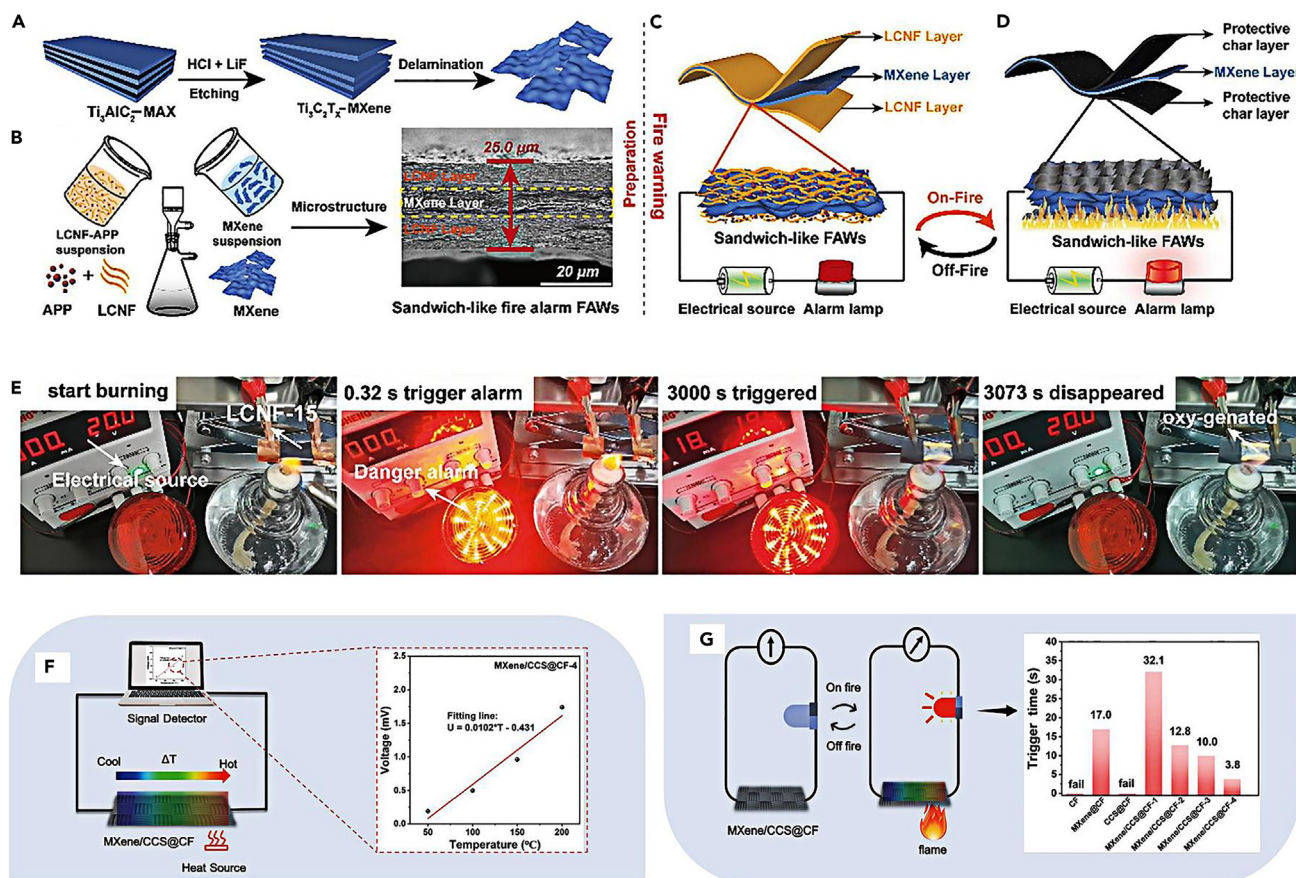


Figure 28. Modulation of thermoelectrochemical properties of lignocellulosic nanoprimer (LCNF) composite with $Ti_3C_2T_x$ MXene

(A–G) The schematic of MXene (A) sandwich-like fire alarm FAWs (B). The early fire warning performances and proposed working mechanism (C, D) Fire-alarm response time and fire duration time (E) of sandwich-like fire alarm FAWs. Reproduced from ref. ¹⁶⁰ with permission. Copyright 2023 Elsevier. Schematic of construction for (F) temperature sensing circuit and (G) fire-warning circuit based on MXene/CCS@CF composites. Reproduced from ref. ¹⁶¹ with permission. Copyright 2021 American Chemical Society.

performance. As is schemed in Figure 28F, the output voltage of MXene/CCS@CF regularly increased with raising the temperature. A nearly linear relationship between the voltage and temperature was observed, fitting the equation of $U = 0.102T - 0.413$ (Figure 28F). Utilizing such liner relationship, the temperature difference between two points of MXene/CCS@CF could be accurately calculated, giving a reliable temperature sensor. The signal of the temperature difference can be converted into voltage. When the temperature was higher than the ignition of combustible materials, a fire might occur. As a consequence, Thereby, the trigger voltage to alarm the fire danger could be set at an early stage. Furthermore, the synergistic effect between MXene and CCS was also investigated, and the result revealed that the mass ratio of CCS has impact on the performance of the flame retardant device. One can see from Figure 28G that MXene/CCS@CF-1 (5 mg/mL CCS solution was used) delivers the most excellent performance. The limited oxygen index of MXene/CCS@CF was as high as 45.5%, and the char length was only 33 mm in vertical burning test. In addition, MXene/CCS@CF could detect a variety of human motions. Moreover, the controllable electrothermal performance renders MXene/CCS@CF as a potential portable heater. MXene/CCS@CF could calculate the temperature difference between the two points of MXene/CCS@CF according to the voltage. Besides, it could trigger the fire-warning system in a very short time when being burned.

Considering MXenes capable of generating electrical signals when the temperature gradient matches well with the output voltage, fire-warning/temperature sensing circuit may be scheduled.

Besides PI and LCNF, many other polymers, such as PVA, PU, PET, have also reported to composite with MXene, which provided the flame retardant.¹⁶² Table 5 list some recent work on MXene based materials

Table 5. Summary and comparison of various MXene-based flame warning systems by utilizing modified MXene as flame warning

Materials information	Alarm response time (s)	Repeatable flame alarm/s	Duration time (s)	Reference
APP/LCNF/MXene	0.32	✓	3073	Ma et al. ¹⁶⁰
PVP/PEG/MXene	1.8	✓	–	Mao et al. ¹⁶³
MXene/CCS@CF	3.8	✓	–	Wang et al. ¹⁶¹
PU/MXene paper	11	✓	–	Zhang et al. ¹⁶⁴
MXene/GO film	1	–	90	Li et al. ¹⁶⁵
MXene/Aramid	10	✓	43	Peng et al. ¹⁶⁶
CNC/MXene	2.1	–	–	Zhang et al. ¹⁶⁷
polyimide/MXene	4.03	✓	–	Zhao et al. ¹⁶⁸
CAS/TA/MXene film	0.982	✓	–	Mao et al. ¹⁶⁹
MXene/Cellulose	<4	✓	–	Zeng et al. ¹⁷⁰
SiO ₂ /PVP/MXene	5	–	2	Li et al. ¹⁷¹
PA/MXene/GO	2	–	–	Li et al. ¹⁷²

for flame alarm application as well as some tradition flame alarm system. Through Table 5 one can see that in most composites MXene provides anti-dripping performance. Take PVA/MXene as an in case example, owing to a physical barrier of MXene sheet, a real flame retardant purpose has difficulty in reaching PVA sample. Similarly, the coated PU with sufficient amount of MXene could reach the rapid self-extinguishing and maintain the original shape even after combustion. Furthermore, incorporated into otherthermally stable substrate, such as polyimide aerogel, cellulose nanofiber, and graphene MXene nanosheets were incorporated into some thermally stable substrates, whereas the composite architectures presented excellent thermal stability and fire-resistance without catching fire.

In another work, Du et al. developed a solar-thermal electricity conversion device by combination of polydopamine-decorated MXene (P-MXene) and biomass-derived phase change materials (PCM). The materials synthesis process includes two sections, synthesis of P-MXene and preparation of eMPCMs (erythritol impregnated into P-MXene/cellulose nanofiber (CNF) hybrid aerogels). The detail synthetic procedures could be schemed in Figures 29A and 29B. The as-prepared P-MXene composites possess 2D-layered structures, which exhibit superior photothermal effects and excellent oxidation stability. After the functionalization process, the as-prepared porous and interconnected 3D eMPCMs avoid liquid leakage during phase transition. By attaching the eMPCMs specimen to a commercial thermoelectric generator equipped with a finned cooler, a solar-thermal-electricity conversion measurement device was fabricated by radiated under a solar simulator with an irradiation intensity of 250 mW/cm² as shown in Figure 29C. A voltage monitor linked with a computer was utilized to record the electric voltage of the eMPCM specimen under irradiation. Figure 29D depicted the electric voltage evolution curves of the ePCM and eMPCMS during solar-thermal-electricity conversion. Owing to the proportional relationship between electric voltage and temperature difference, the output electric voltage behavior of the eMPCMs was expected to be similar to the temperature evolution curves under light irradiation. By prolonging the light irradiation time, the voltage of the eMPCMs may rapidly increase. This could be attributed to the efficient photothermal energy conversion capacity of the PMXene nanosheets. In addition, the mass ratio of P-MXene to CNF in P-MXene/CNF hybrid aerogel was found to have significant impact on the voltage of the device. The result demonstrated that at the mass ratio of 1:1 (eMPCM-4) delivered the highest voltages of 0.63 V.¹⁷³

The benefits of incorporating polymers into MXene are many. On one hand, polymers with hydrophobic carbon backbones yields small sizes in the interlayer space dramatically decrease the thermal conductivity and increase thermoelectric power factor. On the other hand, the flexibility of polymers endows MXene based thermoelectric device wearable and has shown promising potential in body heat management. It should be noted that many polymers are not stable at high temperatures (such as above 800°C) owing to carbonization. It is out of question that more attention would be paid to develop light weight and high temperature tolerant devices.

MXene/inorganic composites for thermoelectric application

Bismuth telluride based alloys are historically reported thermoelectric materials with the best ZT value at room temperature, which are the most utilized candidates. Unfortunately, the large-scale application for power

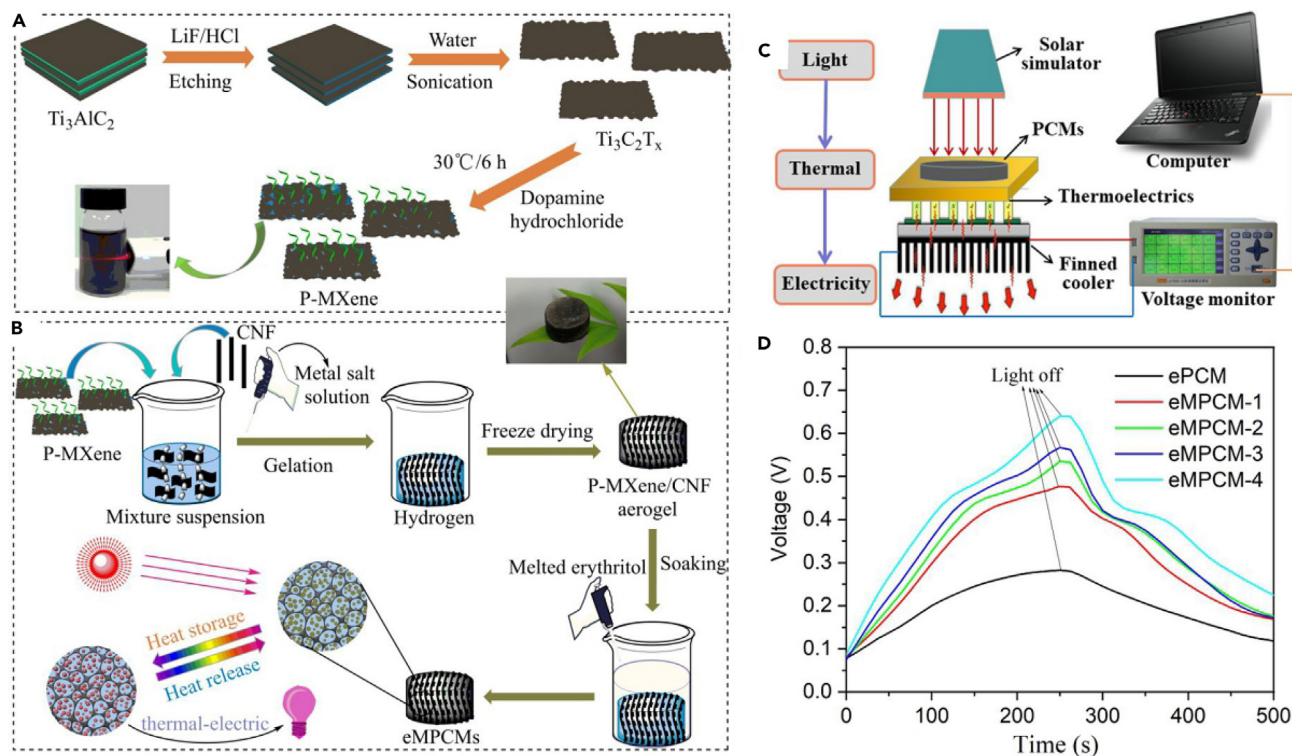
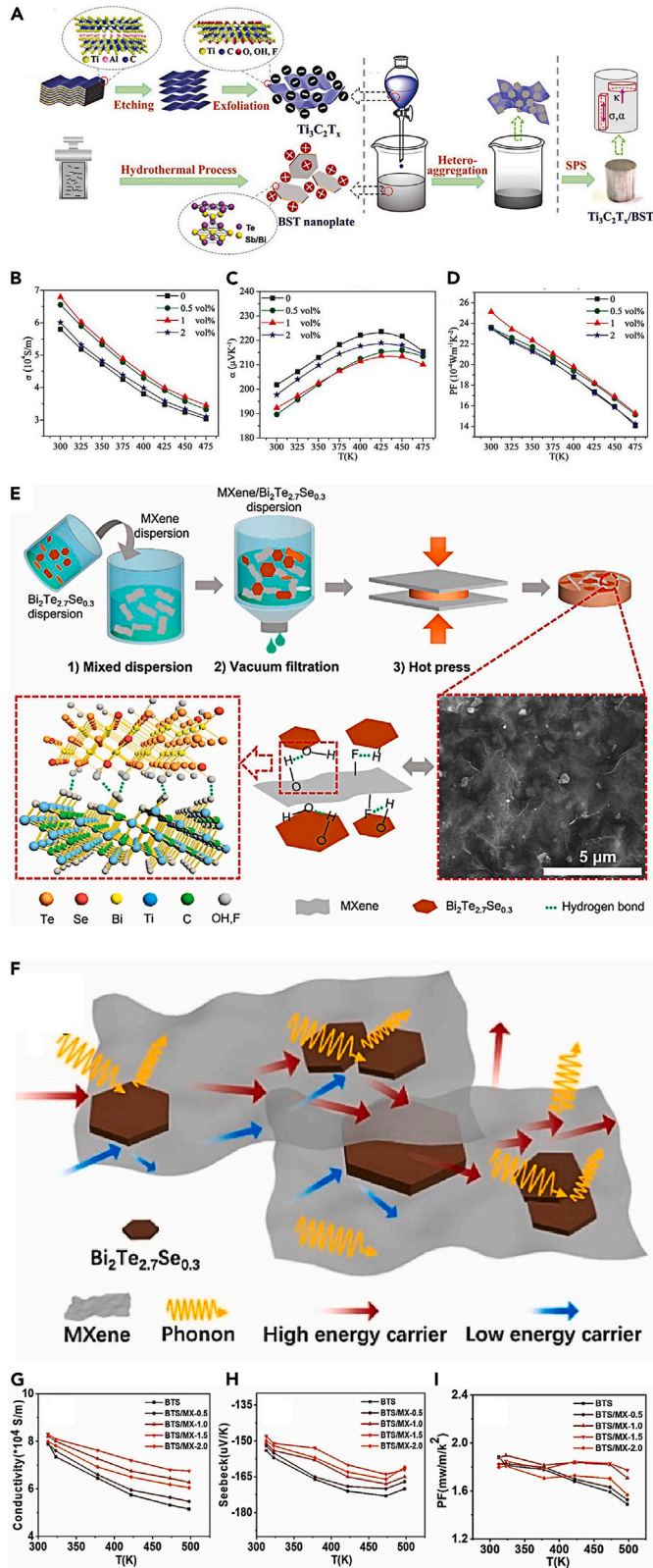


Figure 29. Modulation of thermoelectrochemical properties by polydopamine-modified MXene (P-MXene) complexed with biomass-derived phase change materials (PCM)

(A–C) Schematic illustration for the synthesis of P-MXene (A) and eMPCMs (B). Schematic illustration of the measurement setup for solar-thermal-electricity conversion (C). Temperature evolution curves of ePCM and eMPCMs during solar-thermal-electricity conversion measurement.

(D) Temperature evolution curves of ePCM and eMPCMs during solar-thermal-electricity conversion measurement. Reproduced from ref.¹⁷³ with permission. Copyright 2022 American Chemical Society.

generation is limited by their their unsatisfactory thermoelectric performances in wide-temperature range severely. Some strategies have been demonstrated to be efficient to further boost their ZT in the entire temperature range (or average ZT), including intrinsic defect engineering, nanostructuring and texturing have been developed.^{174–177} In particular, incorporating the nanoscale second phase, such as zero-dimensional nanoparticles/nanodots,^{178,179} 1D carbon nanotubes,¹⁸⁰ 2D graphene,¹⁸¹ a thin Co-P layer,¹⁸² thin ZnO layer,¹⁸³ and so on, are expected to supply abundant hetero-interfaces and grain boundaries, which could dramatically change the carriers and phonon transport behavior in the composites, resulting in the enhancement of ZT in a wide temperature range. Among all incorporated nanoscale second phases, 2D ones are preferred because of their general compatibility with many materials. As for MXene based materials, there have been several examples on MXene/BST composites for thermoelectric applications. For example, Lu et al. fabricated $\text{Ti}_3\text{C}_2\text{T}_x/\text{BST}$ composites using the p-type $\text{Bi}_{0.4}\text{Sb}_{1.6}\text{Te}_3$ (BST) as the matrix and a highly conductive MXene of $\text{Ti}_3\text{C}_2\text{T}_x$ as the second phase. The synthetic process of $\text{Ti}_3\text{C}_2\text{T}_x/\text{BST}$ composites is schemed as shown in Figure 30A, which includes a self-assembly protocol combined with spark plasma sintering (SPS). In the as-prepared $\text{Ti}_3\text{C}_2\text{T}_x/\text{BST}$ composites, the 2D MXene was homogeneously dispersed in the BST matrix, resulting in the improved power factor and greatly reduced thermal conductivity. Similar to V_2VI_3 compounds with low thermal conductivity in the out-of-plane direction induced by the texturing effect, the $\text{Ti}_3\text{C}_2\text{T}_x/\text{BST}$ composites were also confirmed to possess anisotropic thermoelectric properties. In particular, the thermoelectric performance in the out-of-plane direction is superior over the in-plane direction. This work also further revealed the effect of $\text{Ti}_3\text{C}_2\text{T}_x$ on the thermoelectric performance of $\text{Ti}_3\text{C}_2\text{T}_x/\text{BST}$. The result indicated that both the conductivity and the Seebeck coefficient of $\text{Ti}_3\text{C}_2\text{T}_x/\text{BST}$ composites were greatly dependent on the loading amount of $\text{Ti}_3\text{C}_2\text{T}_x$, so was the power factor and ZT. Figure 30B presented the temperature-dependent electrical conductivity of $\text{Ti}_3\text{C}_2\text{T}_x/\text{BST}$ composites, it was found that the overall electrical conductivity increased with the addition of $\text{Ti}_3\text{C}_2\text{T}_x$ nanosheet. When the loading fraction of $\text{Ti}_3\text{C}_2\text{T}_x$ was 1 vol %, the maximum electrical conductivity of $6.9 \times 10^4 \text{ S m}^{-1}$ was achieved, which is about 17% higher than that of pristine BST. Because BST is n-type semiconductor, which exhibits



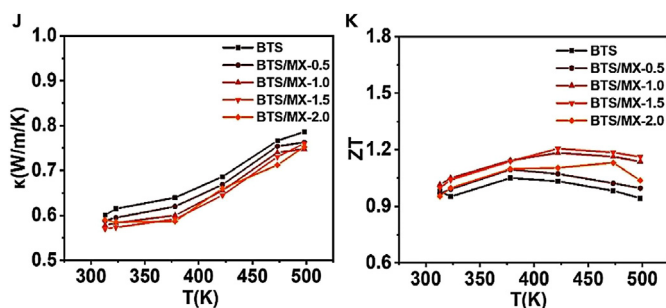


Figure 30. MXene/BST and BTS/MXene composite modulates thermoelectrochemical properties

(A) Schematic illustration for the preparation of $\text{Ti}_3\text{C}_2\text{T}_x$ nanosheets and BST nanoplates.

(B) Self-assembly process for preparing $\text{Ti}_3\text{C}_2\text{T}_x/\text{BST}$ composite powder.

(C) Densification of $\text{Ti}_3\text{C}_2\text{T}_x/\text{BST}$ composite and the illustration of specimens for measuring different properties. (D)

Temperature dependence of power factor for $\text{Ti}_3\text{C}_2\text{T}_x/\text{BST}$ composites with various loading. Reproduced from ref. ¹⁸⁴ with permission. Copyright 2019 John Wiley & Sons.

(E) Synthetic process of BTS/MXene composites.

(F) schematic representation of EMI shielding mechanisms for the BTS/MXene composites. Thermoelectric performance characterization results of BTS/MXene composites, electrical resistivity (G), Seebeck coefficient (H), power factors (I), total thermal conductivity (J) and ZT (K) Reproduced from ref. ¹⁸⁵ with permission. Copyright 2022 Elsevier.

negative Seebeck coefficient. As displayed in Figure 30C, owing to the highly increased carrier density, a much lower Seebeck coefficient for the composites was obtained. Usually the impurity scattering or barrier energy scattering is responsible for the limited reduction of Seebeck coefficient in the composites. A thermoelectric device using $\text{Ti}_3\text{C}_2\text{T}_x/\text{BST}$ composites as p-type legs and commercial Bi_2Te_3 as n-type legs were studied. As shown in Figure 30D, owing to the enhanced electrical conductivity and moderately decreased Seebeck coefficient, the $\text{Ti}_3\text{C}_2\text{T}_x/\text{BST}$ composites supplied the increased power factor (PF) compared to pristine BST. As a consequence, an improved peak ZT up to 1.3 and an average ZT value of 1.23 was obtained from 300 to 475 K. What is more, the stability and mechanical performances of $\text{Ti}_3\text{C}_2\text{T}_x/\text{BST}$ composites were also confirmed to be better than pristine BST, satisfying the requirements for practical applications. In addition, a high thermoelectric conversion efficiency of up to 7.8% is obtained under a temperature gradient of 237 K with the newly developed thermoelectric composites. ¹⁸⁴

Besides BST, currently, BTS (such as $\text{Bi}_2\text{Te}_{2.7}\text{Se}_{0.3}$ compound) also has been considered as an efficient n-type room temperature thermoelectric material. Zhang et al. demonstrated that the incorporation of $\text{Ti}_3\text{C}_2\text{T}_x$ MXene is favor for improving the thermoelectric performance of $\text{Bi}_2\text{Te}_{2.7}\text{Se}_{0.3}$. They found that the lattice thermal conductivity for nanocomposite samples is reduced from 0.77 to 0.41 W/(mK) at 380 K, and the electrical conductivity increases dramatically owing to the increased carrier concentration. As a consequence, a peak ZT of 0.68 is obtained for $\text{Bi}_2\text{Te}_{2.7}\text{Se}_{0.3}/0.1$ wt % $\text{Ti}_3\text{C}_2\text{T}_x$, which is enhanced by 48% compared with pristine $\text{Bi}_2\text{Te}_{2.7}\text{Se}_{0.3}$. ¹⁸⁶ In another work, Jiao et al. also prepared $\text{Bi}_2\text{Te}_{2.7}\text{Se}_{0.3}/\text{Ti}_3\text{C}_2\text{T}_x$ (BTS/MXene) composites. The preparation process is schematically presented in Figure 30E, which involves two steps, mixing BTS and MXene dispersion followed by vacuum-assisted filtration and hot pressing. Thermoelectric investigation evidenced that the BTS/MXene composites offer impressive thermoelectric conversion properties. The improved thermoelectric performance can be ascribed to the high conductivity of MXene and the blocking of low-energy carriers and the scattering of phonons at the interface, as displayed in Figures 30F–30K present the thermoelectric parameters of BTS/MXene composites. Under optimal composition, BTS/MXene composite involving 1.5 wt % MXene offers a peak dimensionless figure of merit (ZT) of 1.2 from 313 to 498 K. ¹⁸⁵

Besides bismuth based compounds, tin (Sn) based materials are reported to possess middle temperature exhibit thermoelectric performance because it exhibits intrinsically low lattice thermal conductivity because of the strong anharmonicity of lattice vibration. Thanks to the low κ_l of $0.23 \text{ W m}^{-1} \text{ K}^{-1}$, giving a high zT of 2.6 at 923 K, so its combination with MXene has achieved high, good and unique thermoelectric functions. ^{187,188} Zhang et al. reported that the incorporation of 2D $\text{Ti}_3\text{C}_2\text{T}_x$ MXene into SnSe matrix can efficiently increase the carrier mobility and concentration, leading to an improved electrical conductivity in the temperature range of 323–523 K. As shown in Figure 31A, the fabrication of SnSe/ $\text{Ti}_3\text{C}_2\text{T}_x$ composites was achieved through an *in-situ* precipitation. By changing the mass ratio of $\text{SnCl}_2 \cdot 2\text{H}_2\text{O}$ to $\text{Ti}_3\text{C}_2\text{T}_x$ MXene, a

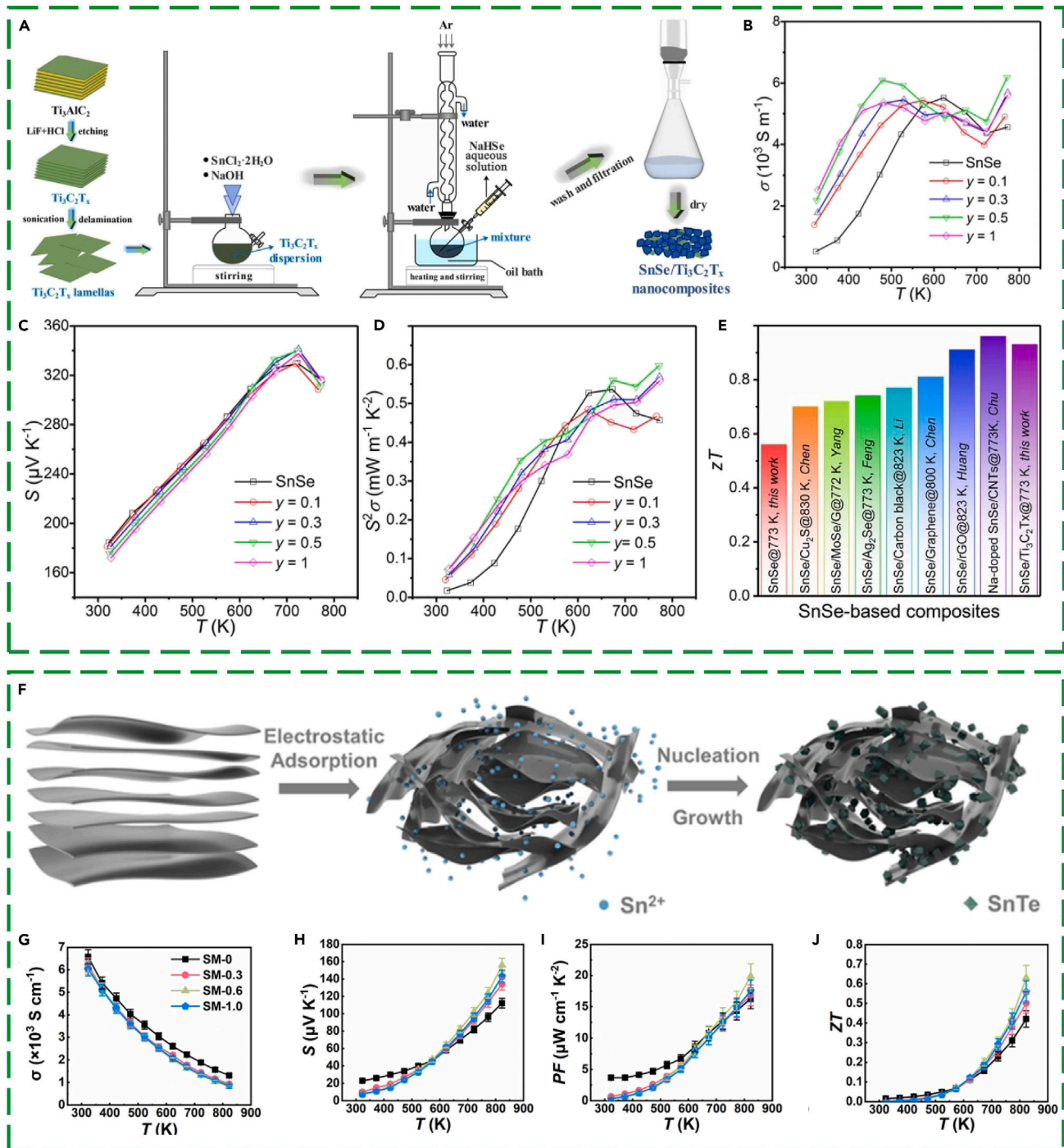


Figure 31. Modulation of thermoelectrochemical properties of tin (Sn) based materials compounded with MXene

(A) Synthetic process of SnSe/Ti₃C₂T_x nanocomposites. Temperature-dependent thermoelectric performances of SnSe/Ti₃C₂T_x nanocomposites.

(B) electrical conductivity.

(C) Seebeck coefficient.

(D and E) power factor, and (E) ZT value and a comparison with other literature. Reproduced from ref. ¹⁸⁹ with permission. Copyright 2022 Elsevier.

(F) Synthetic process of SnTe/Ti₃C₂T_x composites. Temperature-dependent thermoelectric performances of SnTe/Ti₃C₂T_x composites.

(G–J) electrical conductivity, (H) Seebeck coefficient, (I) power factor, and (J) ZT value. Reproduced from ref. ¹⁹⁷ with permission. Copyright 2021 Elsevier.

series of SnSe/Ti₃C₂T_x composites can be obtained. They further revealed that the mass fraction of Ti₃C₂T_x MXene in the composites has significant impact on the thermoelectric performance of Ti₃C₂T_x MXene. One can see from Figure 31B that the combination of Ti₃C₂T_x MXene does not change the temperature-dependent variation trend of electrical conductivity (σ) of SnSe. No matter what ratio of Ti₃C₂T_x MXene to SnSe, the σ value increases gradually when the temperature rises from 323 K to a certain peak temperature (named as T_p , the value of which, varying from 473 K to 623 K, depends on the x value). Such variation trend is ascribed to energy barrier-enhanced carrier scattering at grain boundaries. Also, at the temperature range of T_p to 723 K, the σ decreases continuously; as the temperature elevates beyond 723 K, another increase in σ is observed. One may also note that the σ value of the composites below their T_p is obviously higher than that of pristine SnSe, indicating that the incorporation of Ti₃C₂T_x MXene is favor for improving thermoelectric performance. Figures 31C and 31D presented the Seebeck coefficient (S) and power factor ($S^2\sigma$) of all samples. Excitedly, both the S value and $S^2\sigma$ value are boosted compared to those of pristine SnSe. As for the zT values, the research revealed a peak value of 0.93 at 773 K for SnSe/Ti₃C₂T_x composite with addition of 0.3 wt % Ti₃C₂T_x. Such result is much more advantageous than other SnSe based materials, as demonstrated in Figure 31E.¹⁸⁹ To further increase the concentration of carriers in SnSe₂, which is expected to increase the thermoelectric properties, halogen element doping was tried by many professional groups to optimize the carrier concentration. For example, Wei et al. developed Br-doped SnSe₂/Ti₃C₂T_x composites by a hydrothermal method combined with solid-state synthesis. They gained high carrier concentration of SnSe_{1.97}Br_{0.03/0.4} wt % Ti₃C₂T_x, which is enlarged by three orders of magnitude compared with pristine SnSe₂. What's more, the first-principles calculations revealed that the electrons transfer from the MXene layers into the SnSe₂ matrix was facilitated at elevated temperature. Benefitting from above merits, a peak zT is obtained along out-of-plane direction at 818 K in SnSe_{1.97}Br_{0.03/0.4} wt % Ti₃C₂T_x sample when tested as thermoelectric materials.¹⁹⁰

In another work, Jiang et al. utilized a similar method to prepare SnTe/Ti₃C₂T_x composites, which also concluded a similar result that the thermoelectric performance of SnTe can be enhanced by incorporating MXene. Figures 31F–31J present the synthetic process and thermoelectric performance of SnTe/Ti₃C₂T_x composites. It should be pointed out that the synthesis of SnTe/Ti₃C₂T_x composites was carried out in ethylene glycol but not water, which is different from the work of SnSe/Ti₃C₂T_x composites by Zhang et al. Such preparation difference may be attributed to the different precursors are utilized in their work. For SnTe/Ti₃C₂T_x composites, elementary Te powder was utilized as Te precursor, which should be reduced to Te(II) to form SnTe. Of interest, ethylene glycol as an organic solvent possessing two-OH in its molecule structure can simultaneously act as reducing agent. The case for SnSe/Ti₃C₂T_x composites is different, where NaHSe was utilized as Se(II) precursor.¹⁹¹

As we mentioned before, waste heat covers low grade and high grade, however, most metal chalcogenides, can only serve to recovery low grade waste heat in the low temperature range. Materials with earth abundant and nontoxicity and high chemical/physical/thermal stability are desired to provide large scale power generation using high grade heat at high temperatures. Taking this goal in mind, oxides are outstanding candidates for high-temperature thermoelectric power generation. Among various available materials, donor-doped SrTiO₃ (STO) have turned out to be one of the best candidate because they possess excellent thermoelectric performance with $ZT = 0.6$. To further boost thermoelectric performance of STO for practical applications, constructing heterostructure or composite with other moieties has been demonstrated to be effective. Recently, Dixit et al. prepared STN-MXene composite using a spark plasma sintering process. Their investigation revealed that incorporating Ti₃C₂T_x MXene in a matrix of SrTi_{0.85}Nb_{0.15}O₃ facilitates the delocalization of electrons leading to better than single-crystal-like electron mobility in polycrystalline composites. Figure 32 showed the thermoelectric properties of the as-prepared MXene-STN composite. One can see from Figures 32A and 32B that the thermal conductivities (both electronic thermal conductivity and lattice thermal conductivity) of STN + MXene composites showed a significant increase in compared to pristine STN, which is different from the huge surge in electrical conductivity obtained in these composites. This phenomenon can be ascribed to the presence of highly conductive MXene. As a result, the incorporation of MXene into STN matrix is favor for increase the ZT value as verified in Figure 32C. It should be noted that the percentage of MXene in the final composite has significant impact on the thermoelectric property. Here they applied a quality factor, B , as an indicator parameter. The higher value of B implied the better performance of the composite. as shown in Figure 32D, it was concluded that the composite containing 1% MXene delivers the most excellent performance. In addition, a practical thermoelectric device composed of four legs was constructed and satisfied results were also obtained. The

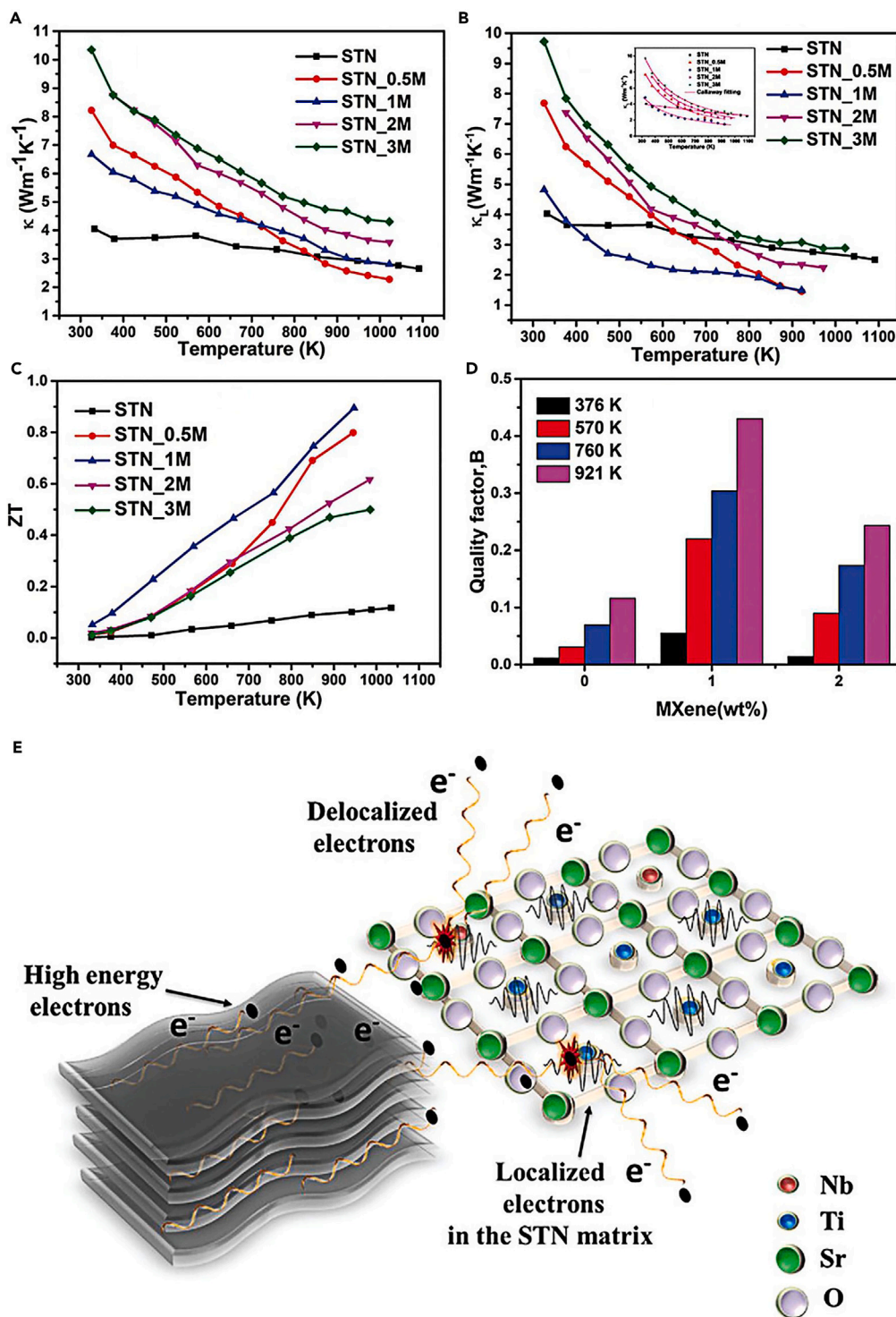


Figure 32. Thermal properties and quality factor analysis

Plot of change in (A) thermal conductivity with temperature.

(B) lattice thermal conductivity with temperature and the Debye Callaway model fitting for all the composites in the inset.

(C) Change in ZT with temperature. (D) Quality factor of pure STN and composite samples at different temperatures. (E) Schematically showing MXene facilitating the delocalization of electrons in the STN matrix by imparting strain and providing high energy electrons. Reproduced from ref. ¹⁹² with permission. Copyright 2023 John Wiley & Sons.

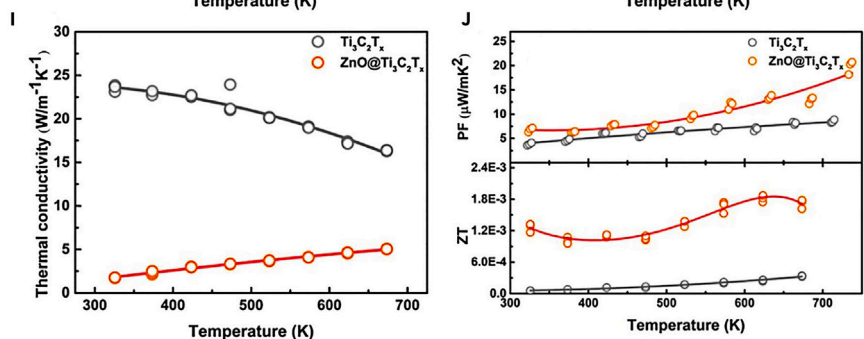
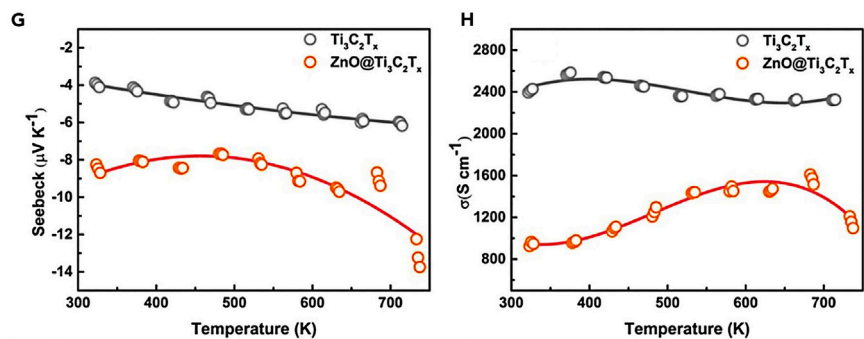
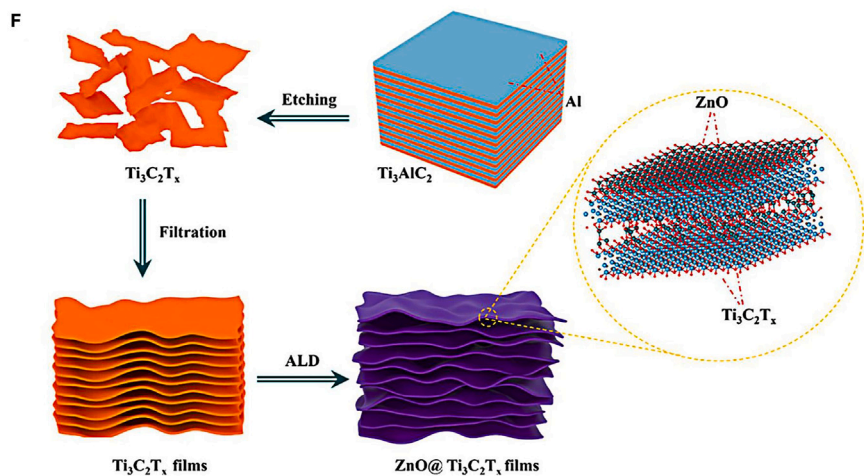
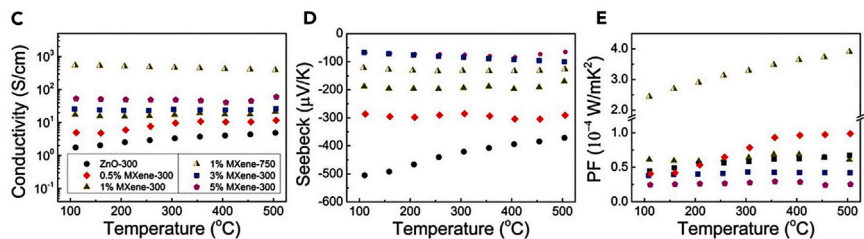
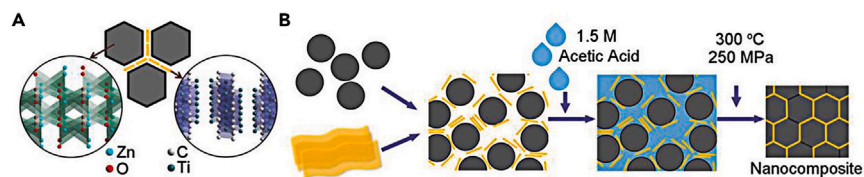


Figure 33. ZnO- $\text{Ti}_3\text{C}_2\text{T}_x$ nanomaterial composite modulates thermoelectrochemical properties

(A) Grain boundary of ZnO- $\text{Ti}_3\text{C}_2\text{T}_x$ nanocomposites.

(B) synthesis of ZnO- $\text{Ti}_3\text{C}_2\text{T}_x$ nanocomposites by cold sintering process, and (C–E) thermoelectric performance of ZnO- $\text{Ti}_3\text{C}_2\text{T}_x$ nanocomposites.

(C) electrical conductivity.

(D) Seebeck coefficient, (E) power factor. Reproduced from ref.²² with permission. Copyright 2018 John Wiley & Sons.

(F) Schematic illustration for growing ZnO layer on $\text{Ti}_3\text{C}_2\text{T}_x$ film ($\text{ZnO@Ti}_3\text{C}_2\text{T}_x$) via atomic layer deposition (ALD) technique.

(G–I) thermoelectric performance comparison of pristine ZnO and $\text{ZnO@Ti}_3\text{C}_2\text{T}_x$, (G) Seebeck coefficient, (H) electrical conductivity, (I) thermal conductivity, and (J) power factor and ZT value. Reproduced from ref.²⁰⁰ with permission. Copyright 2022 American Chemical Society.

underlying physical mechanism for the improvement of thermoelectric performance of MXene/STN could be ascribed to massive surge in electrical conductivity. As shown in Figure 32E, electrons coming out of MXene attain much higher momentum because of highly conductivity of MXene. Owing to the presence of STN matrix, part of these high-energy electrons injected into the STN matrix could be transferred to the Anderson localized electrons, which move above the mobility edge to attain the itinerant states.¹⁹²

ZnO is another potential candidate for thermoelectric energy conversion owing to its high abundance, low cost, nontoxicity, and thermal stability.^{193–198} However, pristine ZnO usually supplies a low electrical conductivity because of the low carrier concentration, limiting its thermoelectric application. Compositing with 2D materials is considered to be a feasible route to increasing the carrier concentration, thus improving the electrical conductivity. Meanwhile, the dispersion of 2D materials along grain boundaries of ZnO is expected to provide abundant interfaces, which may efficiently increase lattice scattering, leading to the decrease of thermal conductivity. To date, some researchers have demonstrated that incorporating MXenes into ZnO is an interest of research for thermoelectric application by increasing the carrier concentration accompanied by reducing the thermal conductivity because of phonon-boundary scattering at interfaces, thereby greatly improving the thermoelectric performances. For instance, Guo et al. synthesized ZnO- $\text{Ti}_3\text{C}_2\text{T}_x$ nanocomposites by a cold sintering process. As schematically presented in Figure 33A, the prepared ZnO- $\text{Ti}_3\text{C}_2\text{T}_x$ nanocomposites are rich in grain boundary, which are benefited for improving the electrical conductivity as well as mechanical stability of ZnO. The preparation process is shown in Figure 33B, in which three steps are involved. First, a homogeneous dispersed $\text{Ti}_3\text{C}_2\text{T}_x$ solution was mixed and sonicated with the ZnO, which is followed by a freeze-dried treatment. Subsequently, by adding 17–20 wt % 1.5 M acetic acid, the ZnO and $\text{Ti}_3\text{C}_2\text{T}_x$ would be mixed homogeneous. Finally, the wetted ZnO- $\text{Ti}_3\text{C}_2\text{T}_x$ powders were pressed in a die under a pressure of 250MPa at a relative low temperature (less than 700°C) for 1 h. Compared to traditionally high temperature (usually over 800°C), this cold sintering process avoids interdiffusion between MXene and ceramics and oxidation of MXene in air. When applied for thermoelectric devices, the ZnO- $\text{Ti}_3\text{C}_2\text{T}_x$ nanocomposites exhibits better thermoelectric properties than pristine ZnO in terms of electrical conductivity, Seebeck coefficient, and power factor, as shown in Figures 33C–33E. It is noted that both the mass percentage of $\text{Ti}_3\text{C}_2\text{T}_x$ nanocomposites in ZnO- $\text{Ti}_3\text{C}_2\text{T}_x$ nanocomposites and the temperature used in cold sintering process have significant impact on the thermoelectric performance of ZnO- $\text{Ti}_3\text{C}_2\text{T}_x$ nanocomposites. The experiment results reveal that the sample containing 1% $\text{Ti}_3\text{C}_2\text{T}_x$ treated at 750°C yields the best performance.²² The improved thermoelectric performance with heat treatment may be ascribed to the change of the concentration of dominant native donors in ZnO, which has also been confirmed by others.¹⁹⁹ Considering the fact that 2D MXene can provide huge specific area and are easily oxidized in the air, Yan et al. developed an atomic layer deposition technique to grow ZnO layer on MXene layer ($\text{ZnO@Ti}_3\text{C}_2\text{T}_x$), as shown in Figure 33F. By adjusting the cycle number of atomic layer deposition, the thickness of ZnO layer could be accurately controlled. Owing to spaces between layers in MXene, both the out surface and inner surface of MXene are covered by ZnO. A comparison thermoelectric performance investigation reveals that $\text{ZnO@Ti}_3\text{C}_2\text{T}_x$ is superior over pristine $\text{Ti}_3\text{C}_2\text{T}_x$, as shown in Figures 33G–33J.²⁰⁰ It is noted that both $\text{ZnO@Ti}_3\text{C}_2\text{T}_x$ and pristine $\text{Ti}_3\text{C}_2\text{T}_x$ give negative Seebeck coefficient. On increasing the temperature from 300 to 700 K, $\text{Ti}_3\text{C}_2\text{T}_x$ possesses a gradual increase in the Seebeck coefficient from -3.87 to -6.17 $\mu\text{V/K}$. Comparatively, $\text{ZnO@Ti}_3\text{C}_2\text{T}_x$ presents a stronger increase tendency (-8.42 to -13.74 $\mu\text{V/K}$). In addition, $\text{ZnO@Ti}_3\text{C}_2\text{T}_x$ still showed continuous enhancement of the Seebeck coefficient at 650 K. The electrical conductivity of $\text{ZnO@Ti}_3\text{C}_2\text{T}_x$ in fact is lower than that of $\text{Ti}_3\text{C}_2\text{T}_x$. The decrease of electrical conductivity could be ascribed to the generation of some acceptor defects such as V_{Zn} and O_i , which are able to reduce the free-electron concentration.²⁰¹ In addition, the thicker ZnO layer on the surface of $\text{Ti}_3\text{C}_2\text{T}_x$ is expected to yields more acceptor defects, leading to a dramatic decrease in the electrical conductivity. By reducing the thickness of ZnO layers or using more complex composition management, the overall electrical conductivity may be further improved.

Currently, fully transparent thermoelectric devices are gaining more and more research interest, where developing p-type transparent thermoelectric materials is necessary. Owing to its prominent

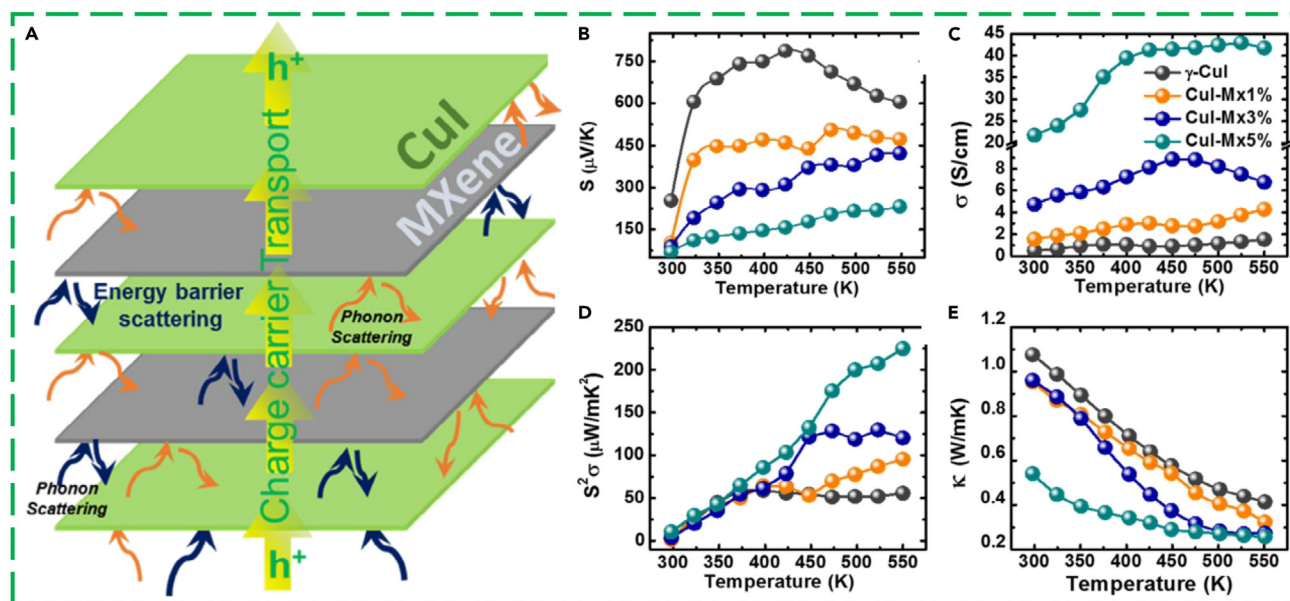


Figure 34. CuI/Ti₃C₂ nanomaterial composite modulates thermoelectrochemical properties

(A) Schematic illustration for the effect of interlaced architecture for energy barrier scattering between CuI and Ti₃C₂, respectively. Temperature-dependent thermoelectric properties of CuI/Ti₃C₂.

(B) Seebeck coefficient.

(C) electrical conductivity, (D) power factor, and (E) thermal conductivity with respect to the Ti₃C₂ nanoinclusion vol %, respectively. Reproduced from ref. ²⁶ with permission. Copyright 2021 John Wiley & Sons.

hole-transport property, earth-abundant copper iodide (CuI), as a p-type semiconducting material with a defect-tunable band gap of 0.9–1.9 eV, has been extensively explored for their transparent and high hole mobility nature.^{202,203} In particular, CuI thin films are reported to possess the largest figure of merit for transparent thermoelectric thin films with 0.22.²⁰⁴ Similar to other p-type semiconductors, however, the electrical conductivities of CuI at room temperature usually are poor, leading to unsatisfied thermoelectric performance at room temperature. Usually tuning the electrical conductivity of materials is expected to be an efficient strategy to improve the thermoelectrical properties. It is confirmed that both the carrier density and scatter phonons can be enhanced by introduction of secondary phase. In particular, nanoinclusions of low-dimension type with a larger phase boundary is preferred, leading to effective transport channeling of the charge carriers and in turn enhancing the thermopower. In addition, because of different bonding and vibrational spectra of the host matrix and nanoinclusions, the thermal conductivity of composites is persistently low, benefiting to yield high performance thermoelectric device. Karthikeyan et al. prepared a CuI/Ti₃C₂ composite via Ti₃C₂ interlacing or nanoinclusion process followed by a hot press treatment. As presented in Figure 34A, the combination of CuI and Ti₃C₂ can add cause alterations in the effective mass of the matrix band structure. The CuI/Ti₃C₂ composite exhibits effective charge transfer channeling and interfacial energy barrier scattering, which is induced in the interlaced architecture of CuI/Ti₃C₂ composite. On the basis of energy scattering theory, energy-dependent charge carrier scattering or channeling occurs at the interface barrier of secondary-phase nanoinclusions, allowing only the charges with higher energy to penetrate through the interface. Figures 34B–34E shows the the Seebeck coefficient, *S* (b), electrical conductivity, σ (c), and the power factor ($S^2\sigma$) (d), and thermal conductivity measured as a function of temperature for CuI/Ti₃C₂ composite at different temperatures. For pristine CuI, the variation of Seebeck coefficient with temperature is complex, which includes three stages. The first stage is below 350 K, in which the Seebeck coefficient increases with temperature linearly. When the temperature is between 350 K and 425 K, the Seebeck coefficient increases slowly. The maximum Seebeck coefficient of CuI at 425 K is 760 μV/K at 425 K. The last stage is located at the temperature zone above 425 K, in which the Seebeck coefficient decreases with the temperature. For CuI/Ti₃C₂ composite, the Seebeck coefficient decreases with the percentage of Ti₃C₂ in the composite. All composites gave lower Seebeck coefficient than pristine CuI. A minimum value of 233 μV/K is obtained for CuI/Ti₃C₂ composite with 5 vol % Ti₃C₂ at 550 K. The electrical conductivity of pristine CuI increases or stays almost constant with increasing temperature, whereas the

introduction of Ti_3C_2 has significant positive effect on the electrical conductivity of CuI. In particular, the electrical conductivity of CuI/ Ti_3C_2 composite with 5 vol % Ti_3C_2 increases fast with temperature initially and then stay almost at 42 S/cm. This value significantly promotes the boost of their corresponding power factor. Particularly of the CuI/ Ti_3C_2 composite with 5 vol % Ti_3C_2 delivers a very large power factor up to $225 \mu\text{W}/(\text{mK}^2)$ at 5500 K, which is much larger than that of pristine CuI and $55 \mu\text{W}/(\text{mK}^2)$ at 360 K. This huge increase in the power factor of the CuI/ Ti_3C_2 composite is absolutely ascribed to the interlacing morphology and densification process. The thermal conductivity of pristine CuI and CuI/ Ti_3C_2 composite with different amount of Ti_3C_2 are shown in Figure 34E. One can see that the thermal conductivity decreases with the increase of Ti_3C_2 . This decrease could be ascribed to the scattering of phonon transport via the energy barrier scattering.²⁶

By compositing with traditional inorganic thermoelectric materials, many desirable advantages may be obtained. For example, charge transport in these inorganic/MXene composites is expected to be dominated by electron mobility. It is confirmed that the electrons transfer from the MXene layers into the inorganic matrix can be dramatically facilitated by elevated temperature. Owing to the intrinsically low lattice thermal conductivity of inorganic matrix, a peak zT close to unity may be achieved. In addition, thermoelectric devices serving the purpose in a high-temperature range may be obtained by MXene/inorganic combination.

CONCLUSION AND PERSPECTIVES

In conclusion, this review summarized state-of-the-art research progress on the synthesis of MXene and its application in thermoelectric devices. It is out of the question that MXene has become a promising family in 2D materials benefiting from the compact layered structure, high thermal stability, and abundant active groups. By precisely controlling the termination groups and the interlayer distances the thermoelectric performance of pristine MXene can be greatly boosted to some extent. Also, by composite with other functional materials, such as carbon nanotube, polymers, and inorganic nanomaterials, more and more MXene based thermoelectric devices have been reported. Despite significant advances and received growing attention in the last decade, some issues remain unresolved in both MXene synthesis and thermoelectric device construction.

For the synthesis of MXene family, there are several challenges in the next decade. (1) The scientific community is supposed to identify new precursors. Currently, the syntheses of MXene are much dependent on parent MAX precursor. It is belonged to top-down process from MAX to MXene. The synthesis of MAX usually consumes a large amount of energy, which leads to serious environment issues. Going forward, more elemental composition, safer process, low cost, more mass production is desired. In addition, if possible, MXene may be obtained by down to top method, such as from reaction between metal precursor and carbon precursor (CO_2 might be the most preferred). (2) The family of MXene might be enlarged further. For one thing, great progress has been made on the synthesis of carbide MXenes, preparation of nitrides is trailing behind. For another thing, the n value in $\text{M}_{n+1}\text{A}_n\text{X}$ needs to be further enlarged, which is currently no more than 4. (3) Entropy engineering might be involved in next decades. By introducing multi-transition metals into the M sites in MXene, more promising properties may come about. Entropy engineering allows enlarging the family of MXenes. Perhaps for this goal two strategies are effective. One is presynthesize multimetal containing MAX parent phase, followed by etching to yield multimetal containing MXene. The second strategy refers to post introduction of more metal element into the single metal containing MXene via cation exchange.

MXene-based materials possess excellent electrical transport properties, and advantages such as adjustable termination groups, capable of compositing with various moieties, such as polymers, carbons, and inorganics to improve the mechanical strength and good temperature stability. The most significant achievement in MXene-based thermoelectrics was their higher ZT value achieved for pristine MXenes. Significantly, the high conductivity of MXenes is dominated by electron mobility, which in turn leads to high thermal conductivity, unfavorable to high thermoelectric performance. As a result, there is a great scope for zT improvement by electronic engineering through compositing with other materials. In this way, MXene based materials are expected to meet the requirements of practical applicability. For example, for high-temperature thermoelectric devices, MXene/inorganics were evaluated with better thermomechanical properties and high-temperature stability, whereas MXene/polymer composites were more preferred for wearable thermoelectrics. For future trends, both opportunities and challenges exist as listed below.

- (1) Techniques to test and improve the thermal property of MXene based materials at the working temperature should be needed. This is important to prevent electromigration or diffusion of the

interconnect/conducting stripes or buffer layer occurs into the thermoelectric material, worsening its properties on long-term operations.

- (2) The human body releases approximately 60–180 W of heat, depending on body activity. Accordingly, if efficient wearable thermoelectric devices could convert just a tiny fraction of this energy (less than 0.1%) into electrical power, then, enough power would be produced to supply wearable devices (e.g., health sensors, wearables, etc.). As a consequence, more attention should be paid to develop lightweight, conformable, and breathable MXene based composites to meet the practical requirements of wearable thermoelectric devices.
- (3) 3D spatial information might be considered. For example, fire alarm devices are required to respond in time. Usually, the distance between the position of fire occurrence and the alarm device are several or hundreds/thousands of meters. The reliability and stability of the fire alarm devices should be further improved.
- (4) Multi-field effect might be serious considered. There are at least two reasons to take multi-field effect into account when constructing thermoelectric devices. For one thing, the heat source can be photo- or magnetic- or microwave induced. These heat sources are expected to provide an additional field, which may affect the performance of the device. For another thing, thermoelectric device in future may be used in space, where gravity field may be not available.
- (5) Finally, more comprehensive theoretical and experimental strategies are needed to take full advantage of MXenes merits. Combining theoretical and experimental investigation, it is expected to boost the performance of MXenes, meeting the comprehensive requirement in converting/storing clean energy and developing flexible electronic devices.

ACKNOWLEDGMENTS

The authors acknowledge the financial support from the National Natural Science Foundation of China (21403091).

AUTHOR CONTRIBUTIONS

M.Y.Z designed, conceived, and drafted the manuscript, while C.C.L and L.R.L were responsible for image embellishment, table organization, and literature formatting changes. All authors revised the manuscript and approved the final version.

DECLARATION OF INTERESTS

The authors declare no competing financial interest.

REFERENCES

1. Bu, Z., Zhang, X., Hu, Y., Chen, Z., Lin, S., Li, W., Xiao, C., and Pei, Y. (2022). A record thermoelectric efficiency in tellurium-free modules for low-grade waste heat recovery. *Nat. Commun.* 13, 237. <https://doi.org/10.1038/s41467-021-27916-y>.
2. Wang, D., Zhu, X., Cui, C., Dong, M., Jiang, H., Li, Z., Liu, Z., Zhu, W., and Wang, J.G. (2013). Efficiency and optimal performance evaluation of organic Rankine cycle for low grade waste heat power generation. *Energy* 53, 343–353. <https://doi.org/10.1016/j.energy.2012.11.010>.
3. Benz, S.A., Menberg, K., Bayer, P., and Kurylyk, B.L. (2022). Shallow subsurface heat recycling is a sustainable global space heating alternative. *Nat. Commun.* 13, 3962. <https://doi.org/10.1038/s41467-022-31624-6>.
4. Liu, B., and Rajagopal, D. (2019). Life-cycle energy and climate benefits of energy recovery from wastes and biomass residues in the United States. *Nat. Energy* 4, 700–708. <https://doi.org/10.1038/s41560-019-0430-2>.
5. Ying, P., He, R., Mao, J., Zhang, Q., Reith, H., Sui, J., Ren, Z., Nielsch, K., and Schierning, G. (2021). Towards tellurium-free thermoelectric modules for power generation from low-grade heat. *Nat. Commun.* 12, 1121. <https://doi.org/10.1038/s41467-021-21391-1>.
6. Straub, A.P., Yip, N.Y., Lin, S., Lee, J., and Elimelech, M. (2016). Harvesting low-grade heat energy using thermo-osmotic vapour transport through nanoporous membranes. *Nat. Energy* 1, 16090. <https://doi.org/10.1038/nenergy.2016.90>.
7. Bell, L.E. (2008). Cooling, heating, generating power, and recovering waste heat with thermoelectric systems. *Science* 321, 1457–1461. <https://doi.org/10.1126/science.1158899>.
8. Zhang, Q., Deng, K., Wilkens, L., Reith, H., and Nielsch, K. (2022). Micro-thermoelectric devices. *Nat. Electron.* 5, 333–347. <https://doi.org/10.1038/s41928-022-00776-0>.
9. Yan, Q., and Kanatzidis, M.G. (2022). High-performance thermoelectrics and challenges for practical devices. *Nat. Mater.* 21, 503–513. <https://doi.org/10.1038/s41563-021-01109-w>.
10. Shuai, J., Mao, J., Song, S., Zhang, Q., Chen, G., and Ren, Z. (2017). Recent progress and future challenges on thermoelectric Zintl materials. *Mater. Today Phys.* 1, 74–95. <https://doi.org/10.1016/j.mtphys.2017.06.003>.
11. He, R., Schierning, G., and Nielsch, K. (2018). Thermoelectric devices: a review of devices, architectures, and contact optimization. *Adv. Mater. Technol.* 3, 1700256. <https://doi.org/10.1002/admt.201700256>.
12. Behnia, K. (2015). *Fundamentals of Thermoelectricity* (Oxford University Press). <https://doi.org/10.1093/acprof:oso/9780199697663.001.0001>.

13. Luo, H., Li, X., Wang, Y., Jin, Y., Yao, M., and Yang, J. (2022). High-throughput screening of room temperature active Peltier cooling materials in Heusler compounds. *npj Comput. Mater.* 8, 199. <https://doi.org/10.1038/s41524-022-00887-4>.
14. Shi, X.-L., Zou, J., and Chen, Z.-G. (2020). Advanced thermoelectric design: from materials and structures to devices. *Chem. Rev.* 120, 7399–7515. <https://doi.org/10.1021/acs.chemrev.0c00026>.
15. Naguib, M., Kurtoglu, M., Presser, V., Lu, J., Niu, J., Heon, M., Hultman, L., Gogotsi, Y., and Barsoum, M.W. (2011). Two-dimensional nanocrystals produced by exfoliation of Ti_3AlC_2 . *Adv. Mater.* 23, 4248–4253. <https://doi.org/10.1002/adma.201102306>.
16. Ghidui, M., Lukatskaya, M.R., Zhao, M.-Q., Gogotsi, Y., and Barsoum, M.W. (2014). Conductive two-dimensional titanium carbide ‘clay’ with high volumetric capacitance. *Nature* 516, 78–81. <https://doi.org/10.1038/nature13970>.
17. Deysher, G., Shuck, C.E., Hantanasirisakul, K., Frey, N.C., Foucher, A.C., Maleski, K., Sarycheva, A., Shenoy, V.B., Stach, E.A., Anasori, B., and Gogotsi, Y. (2020). Synthesis of Mo_4VAIC_4 MAX phase and two-dimensional Mo_4VC_4 MXene with five atomic layers of transition metals. *ACS Nano* 14, 204–217. <https://doi.org/10.1021/acsnano.9b07708>.
18. Fu, Z., Wang, N., Legut, D., Si, C., Zhang, Q., Du, S., Germann, T.C., Francisco, J.S., and Zhang, R. (2019). Rational design of flexible two-dimensional MXenes with multiple functionalities. *Chem. Rev.* 119, 11980–12031. <https://doi.org/10.1021/acs.chemrev.9b00348>.
19. Mathis, T.S., Maleski, K., Goad, A., Sarycheva, A., Anayee, M., Foucher, A.C., Hantanasirisakul, K., Shuck, C.E., Stach, E.A., and Gogotsi, Y. (2021). Modified MAX phase synthesis for environmentally stable and highly conductive Ti_3C_2 MXene. *ACS Nano* 15, 6420–6429. <https://doi.org/10.1021/acsnano.0c08357>.
20. Gogotsi, Y., and Huang, Q. (2021). MXenes: two-dimensional building blocks for future materials and devices. *ACS Nano* 15, 5775–5780. <https://doi.org/10.1021/acsnano.1c03161>.
21. Kim, H., Anasori, B., Gogotsi, Y., and Alshareef, H.N. (2017). Thermoelectric properties of two-dimensional molybdenum-based MXenes. *Chem. Mater.* 29, 6472–6479. <https://doi.org/10.1021/acs.chemmater.7b02056>.
22. Guo, J., Legum, B., Anasori, B., Wang, K., Lelyukh, P., Gogotsi, Y., and Randall, C.A. (2018). Cold sintered ceramic nanocomposites of 2D MXene and zinc oxide. *Adv. Mater.* 30, 1801846. <https://doi.org/10.1002/adma.201801846>.
23. He, P., Cao, M.-S., Shu, J.-C., Cai, Y.-Z., Wang, X.-X., Zhao, Q.-L., and Yuan, J. (2019). Atomic layer tailoring titanium carbide MXene to tune transport and polarization for utilization of electromagnetic energy beyond solar and chemical energy. *ACS Appl. Mater. Interfaces* 11, 12535–12543. <https://doi.org/10.1021/acsami.9b00593>.
24. Guan, X., Feng, W., Wang, X., Venkatesh, R., and Ouyang, J. (2020). Significant enhancement in the seebeck coefficient and power factor of p-type poly(3,4-ethylenedioxythiophene):poly(styrenesulfonate) through the incorporation of n-type MXene. *ACS Appl. Mater. Interfaces* 12, 13013–13020. <https://doi.org/10.1021/acsami.9b21185>.
25. Park, T., Cho, K., and Kim, S. (2021). Thin-film thermoelectric generators comprising molybdenum-based MXenes pn modules. *Adv. Mater. Technol.* 6, 2100590. <https://doi.org/10.1002/admt.202100590>.
26. Karthikeyan, V., Theja, V.C.S., De Souza, M.M., and Roy, V.A.L. (2022). Hierarchically interlaced 2D copper iodide/MXene composite for high thermoelectric performance. *Phys. Status Solidi RRL* 16, 2100419. <https://doi.org/10.1002/pssr.202100419>.
27. Wei, S., Ma, J., Wu, D., Chen, B., Du, C., Liang, L., Huang, Y., Li, Z., Rao, F., Chen, G., and Liu, Z. (2023). Constructing flexible film electrode with porous layered structure by MXene/SWCNTs/PANI ternary composite for efficient low-grade thermal energy harvest. *Adv. Funct. Mater.* 33, 2209806. <https://doi.org/10.1002/adfm.202209806>.
28. Huang, W., Hu, L., Tang, Y., Xie, Z., and Zhang, H. (2020). Recent advances in functional 2D MXene-based nanostructures for next-generation devices. *Adv. Funct. Mater.* 30, 2005223. <https://doi.org/10.1002/adfm.202005223>.
29. Qin, T., Wang, Z., Wang, Y., Besenbacher, F., Otyepka, M., and Dong, M. (2021). Recent progress in emerging two-dimensional transition metal carbides. *Nano-Micro Lett.* 13, 183. <https://doi.org/10.1007/s40820-021-00710-7>.
30. Aslam, M.K., Niu, Y., and Xu, M. (2021). MXenes for non-lithium-ion (Na, K, Ca, Mg, and Al) batteries and supercapacitors. *Adv. Energy Mater.* 11, 2000681. <https://doi.org/10.1002/aenm.202000681>.
31. Pang, J., Chang, B., Liu, H., and Zhou, W. (2022). Potential of MXene-based heterostructures for energy conversion and storage. *ACS Energy Lett.* 7, 78–96. <https://doi.org/10.1021/acsenergylett.1c02132>.
32. Jin, C., and Bai, Z. (2022). MXene-based textile sensors for wearable applications. *ACS Sens.* 7, 929–950. <https://doi.org/10.1021/acssensors.2c00097>.
33. Ayodhya, D. (2023). A review of recent progress in 2D MXenes: synthesis, properties, and applications. *Diam. Relat. Mater.* 132, 109634. <https://doi.org/10.1016/j.diamond.2022.109634>.
34. Sherryina, A., and Tahir, M. (2021). Role of Ti_3C_2 MXene as prominent Schottky barriers in driving hydrogen production through photoinduced water splitting: a comprehensive review. *ACS Appl. Energy Mater.* 4, 11982–12006. <https://doi.org/10.1021/acsaem.1c02241>.
35. Jamil, F., Ali, H.M., and Janjua, M.M. (2021). MXene based advanced materials for thermal energy storage: a recent review. *J. Energy Storage* 35, 102322. <https://doi.org/10.1016/j.est.2021.102322>.
36. Peng, C., Wei, P., Chen, X., Zhang, Y., Zhu, F., Cao, Y., Wang, H., Yu, H., and Peng, F. (2018). A hydrothermal etching route to synthesis of 2D MXene (Ti_3C_2 , Nb_2C): enhanced exfoliation and improved adsorption performance. *Ceram. Int.* 44, 18886–18893. <https://doi.org/10.1016/j.ceramint.2018.07.124>.
37. Li, L., Zhou, A., Xu, L., Li, Z., and Wang, L. (2013). Synthesis of high pure Ti_3AlC_2 and Ti_2AlC powders from TiH_2 powders as Ti source by tube furnace. *J. Wuhan Univ. Technol.-Materials Sci. Ed.* 28, 882–887. <https://doi.org/10.1007/s11595-013-0786-2>.
38. Lapauw, T., Tunca, B., Cabioch, T., Lu, J., Persson, P.O.Å., Lambrinou, K., and Vleugels, J. (2016). Synthesis of MAX phases in the Hf-Al-C system. *Inorg. Chem.* 55, 10922–10927. <https://doi.org/10.1021/acs.inorgchem.6b01398>.
39. Tunca, B., Lapauw, T., Karakulina, O.M., Batuk, M., Cabioch, T., Hadermann, J., Delville, R., Lambrinou, K., and Vleugels, J. (2017). Synthesis of MAX phases in the Zr-Ti-Al-C system. *Inorg. Chem.* 56, 3489–3498. <https://doi.org/10.1016/j.ceramint.2022.11.041>.
40. Jiang, Q., Zeng, X., and Hu, C. (2022). A promising layered thermoelectric metallic ceramic with ultra-high temperature stability: $\text{Mo}_2\text{Ti}_2\text{AlC}_3$. *J. Alloys Compd.* 922, 166212. <https://doi.org/10.1016/j.jallcom.2022.166212>.
41. Nemani, S.K., Zhang, B., Wyatt, B.C., Hood, Z.D., Manna, S., Khaledialidusti, R., Hong, W., Sternberg, M.G., Sankaranarayanan, S.K.R.S., and Anasori, B. (2021). High-entropy 2D carbide MXenes: TiVNBMoC_3 and TiVCrMoC_3 . *ACS Nano* 15, 12815–12825. <https://doi.org/10.1021/acsnano.1c02775>.
42. Zhou, J., Tao, Q., Ahmed, B., Palisaitis, J., Persson, I., Halim, J., Barsoum, M.W., Persson, P.O.Å., and Rosen, J. (2022). High-entropy laminate metal carbide (MAX phase) and its two-dimensional derivative MXene. *Chem. Mater.* 34, 2098–2106. <https://doi.org/10.1021/acs.chemmater.1c03348>.
43. Cui, C., Hu, M., Zhang, C., Cheng, R., Yang, J., and Wang, X. (2018). High-capacitance $\text{Ti}_3\text{C}_2\text{Tx}$ MXene obtained by etching submicron Ti_3AlC_2 grains grown in molten salt. *Chem. Commun.* 54, 8132–8135. <https://doi.org/10.1039/C8CC04350G>.
44. Gogotsi, Y.G., and Andrievski, R.A. (1999). *Materials Science of Carbides, Nitrides And Borides* (Springer). <https://doi.org/10.1007/978-94-011-4562-6>.

45. Li, S., Song, J., Che, Y., Jiao, S., He, J., and Yang, B. (2023). Advances in molten salt synthesis of non-oxide materials. *Energy Environ. Mater.* 6, e123. <https://doi.org/10.1002/eeem.2.12339>.
46. Bärmann, P., Haneke, L., Wrogegmann, J.M., Winter, M., Guillon, O., Placke, T., and Gonzalez-Julian, J. (2021). Scalable synthesis of MAX phase precursors toward titanium-based MXenes for lithium-ion batteries. *ACS Appl. Mater. Interfaces* 13, 26074–26083. <https://doi.org/10.1021/acsami.1c05889>.
47. Roy, C., Banerjee, P., and Bhattacharyya, S. (2020). Molten salt shielded synthesis (MS₃) of Ti₂AlN and V₂AlC MAX phase powders in open air. *J. Eur. Ceram. Soc.* 40, 923–929. <https://doi.org/10.1016/j.jeurceramsoc.2019.10.020>.
48. Siebert, J.P., Bischoff, L., Lepple, M., Zintler, A., Molina-Luna, L., Wiedwald, U., and Birkel, C.S. (2019). Sol-gel based synthesis and enhanced processability of MAX phase Cr₂GaC. *J. Mater. Chem. C* 7, 6034–6040. <https://doi.org/10.1039/C9TC01416K>.
49. Siebert, J.P., Patarakun, K., and Birkel, C.S. (2022). Mechanistic insights into the nonconventional sol-gel synthesis of MAX phase M₂GeC (M = V, Cr). *Inorg. Chem.* 61, 1603–1610. <https://doi.org/10.1021/acs.inorgchem.1c03415>.
50. Siebert, J.P., Mallett, S., Juelsholt, M., Pazniak, H., Wiedwald, U., Page, K., and Birkel, C.S. (2021). Structure determination and magnetic properties of the Mn-doped MAX phase Cr₂GaC. *Mater. Chem. Front.* 5, 6082–6091. <https://doi.org/10.1039/D1QM00454A>.
51. Hamm, C.M., Bocarsly, J.D., Seward, G., Kramm, U.I., and Birkel, C.S. (2017). Non-conventional synthesis and magnetic properties of MAX phases (Cr/Mn)₂AlC and (Cr/Fe)₂AlC. *J. Mater. Chem. C* 5, 5700–5708. <https://doi.org/10.1039/C7TC00112F>.
52. Siebert, J.P., Flores, M., and Birkel, C.S. (2022). Shape control of MAX phases by biopolymer sol-gel synthesis: Cr₂GaC thick films, microspheres, and hollow microspheres. *ACS Org. Inorg. Au* 2, 59–65. <https://doi.org/10.1021/acsorginorgau.1c00022>.
53. Kumar, A., Dutta, S., Kim, S., Kwon, T., Patil, S.S., Kumari, N., Jeevanandham, S., and Lee, I.S. (2022). Solid-state reaction synthesis of nanoscale materials: strategies and applications. *Chem. Rev.* 122, 12748–12863. <https://doi.org/10.1021/acs.chemrev.1c00637>.
54. Liu, Z., Waki, T., Tabata, Y., and Nakamura, H. (2014). Mn-doping-induced itinerant-electron ferromagnetism in Cr₂GeC. *Phys. Rev. B* 89, 054435. <https://doi.org/10.1103/PhysRevB.89.054435>.
55. Arole, K., Blivin, J.W., Bruce, A.M., Athavale, S., Echols, I.J., Cao, H., Tan, Z., Radovic, M., Lutkenhaus, J.L., and Green, M.J. (2022). Exfoliation, delamination, and oxidation stability of molten salt etched Nb₂CTz MXene nanosheets. *Chem. Commun.* 58, 10202–10205. <https://doi.org/10.1039/D2CC02237K>.
56. Eklund, P., Rosen, J., and Persson, P.O.Å. (2017). Layered ternary M_{n+1}AX_n phases and their 2D derivative MXene: an overview from a thin-film perspective. *J. Phys. D Appl. Phys.* 50, 113001–113015. <https://doi.org/10.1088/1361-6463/aa57bc>.
57. Eklund, P., Beckers, M., Jansson, U., Högberg, H., and Hultman, L. (2010). The Mn+1AX_n phases: materials science and thin-film processing. *Thin Solid Films* 518, 1851–1878. <https://doi.org/10.1016/j.tsf.2009.07.184>.
58. Gonzalez-Julian, J., Onrubia, S., Bram, M., and Guillon, O. (2016). Effect of sintering method on the microstructure of pure Cr₂AlC MAX phase ceramics. *J. Ceram. Soc. Japan* 124, 415–420. <https://doi.org/10.2109/jcersj2.15263>.
59. Tunca, B., Lapauw, T., Delville, R., Neuville, D.R., Hennet, L., Thiaudière, D., Ouisse, T., Hadermann, J., Vleugels, J., and Lambrinou, K. (2019). Synthesis and characterization of double solid solution (Zr,Ti)₂(Al,Sn)C MAX phase ceramics. *Inorg. Chem.* 58, 6669–6683. <https://doi.org/10.1021/acs.inorgchem.9b00065>.
60. Dubois, S., Cabioch, T., Chartier, P., Gauthier, V., and Jaouen, M. (2007). A new ternary nanolaminate carbide: Ti₃SnC₂. *J. Am. Ceram. Soc.* 90, 2642–2644. <https://doi.org/10.1111/j.1551-2916.2007.01766.x>.
61. Wang, S., Cheng, J., Zhu, S., Ma, J., Qiao, Z., Yang, J., and Liu, W. (2017). A novel route to prepare a Ti₃SnC₂/Al₂O₃ composite. *Scr. Mater.* 131, 80–83. <https://doi.org/10.1016/j.scriptamat.2017.01.013>.
62. Fashandi, H., Dahlqvist, M., Lu, J., Palisaitis, J., Simak, S.I., Abrikosov, I.A., Rosen, J., Hultman, L., Andersson, M., Lloyd Spetz, A., and Eklund, P. (2017). Synthesis of Ti₃AuC₂, Ti₃Au₂C₂ and Ti₃IrC₂ by noble metal substitution reaction in Ti₃SiC₂ for high-temperature-stable Ohmic contacts to SiC. *Nat. Mater.* 16, 814–818. <https://doi.org/10.1038/nmat4896>.
63. Fashandi, H., Lai, C.C., Dahlqvist, M., Lu, J., Rosen, J., Hultman, L., Greczynski, G., Andersson, M., Lloyd Spetz, A., and Eklund, P. (2017). Ti₂Au₂C and Ti₃Au₂C₂ formed by solid state reaction of gold with Ti₂AlC and Ti₃AlC₂. *Chem. Commun.* 53, 9554–9557. <https://doi.org/10.1039/C7CC04701K>.
64. Cuskelly, D.T., and Kisi, E.H. (2016). Single-step carbothermal synthesis of high-purity MAX phase powders. *J. Am. Ceram. Soc.* 99, 1137–1140. <https://doi.org/10.1111/jace.14170>.
65. Hamm, C.M., Schäfer, T., Zhang, H., and Birkel, C.S. (2016). Non-conventional synthesis of the 413 MAX phase V₄AlC₃. *Z. Anorg. Allg. Chem.* 642, 1397–1401. <https://doi.org/10.1002/zaac.201600370>.
66. Kubitzka, N., Reitz, A., Zieschang, A.-M., Pazniak, H., Albert, B., Kalha, C., Schlueter, C., Regoutz, A., Wiedwald, U., and Birkel, C.S. (2022). From MAX phase carbides to nitrides: synthesis of V₂GaC, V₂GaN, and the carbonitride V₂GaC_{1-x}N_x. *Inorg. Chem.* 61, 10634–10641. <https://doi.org/10.1021/acs.inorgchem.2c00200>.
67. Naguib, M., Mashtalir, O., Carle, J., Presser, V., Lu, J., Hultman, L., Gogotsi, Y., and Barsoum, M.W. (2012). Two-dimensional transition metal carbides. *ACS Nano* 6, 1322–1331. <https://doi.org/10.1021/nn204153h>.
68. Wang, H.-W., Naguib, M., Page, K., Wesolowski, D.J., and Gogotsi, Y. (2016). Resolving the structure of Ti₃C₂T_x MXenes through multilevel structural modeling of the atomic pair distribution function. *Chem. Mater.* 28, 349–359. <https://doi.org/10.1021/acs.chemmater.5b04250>.
69. Tran, M.H., Schäfer, T., Shahraei, A., Dürschnabel, M., Molina-Luna, L., Kramm, U.I., and Birkel, C.S. (2018). Adding a new member to the MXene family: synthesis, structure, and electrocatalytic activity for the hydrogen evolution reaction of V₄C₃T_x. *ACS Appl. Energy Mater.* 1, 3908–3914. <https://doi.org/10.1021/acsaem.8b00652>.
70. Wang, D., Si, J., Lin, S., Zhang, R., Huang, Y., Yang, J., Lu, W., Zhu, X., and Sun, Y. (2020). Achieving macroscopic V₄C₃T_x MXene by selectively etching Al from V₄AlC₃ single crystals. *Inorg. Chem.* 59, 3239–3248. <https://doi.org/10.1021/acs.inorgchem.9b03625>.
71. VahidMohammadi, A., Mojtavavi, M., Caffrey, N.M., Wanunu, M., and Beidaghi, M. (2019). Assembling 2D MXenes into highly stable pseudocapacitive electrodes with high power and energy densities. *Adv. Mater.* 31, 1806931. <https://doi.org/10.1002/adma.201806931>.
72. Cheng, Y., Wang, L., Li, Y., Song, Y., and Zhang, Y. (2019). Etching and exfoliation properties of Cr₂AlC into Cr₂CO₂ and the electrocatalytic performances of 2D Cr₂CO₂ MXene. *J. Phys. Chem. C* 123, 15629–15636. <https://doi.org/10.1021/acs.jpcc.9b03120>.
73. Meshkian, R., Näslund, L.Å., Halim, J., Lu, J., Barsoum, M.W., and Rosen, J. (2015). Synthesis of two-dimensional molybdenum carbide, Mo₂C, from the gallium based atomic laminate MQ₂Ga₂C. *Scripta Mater.* 108, 147–150. <https://doi.org/10.1016/j.scriptamat.2015.07.003>.
74. Anasori, B., Halim, J., Lu, J., Voigt, C.A., Hultman, L., and Barsoum, M.W. (2015). Mo₂TiAlC₂: a new ordered layered ternary carbide. *Scr. Mater.* 101, 5–7. <https://doi.org/10.1016/j.scriptamat.2014.12.024>.
75. Anasori, B., Dahlqvist, M., Halim, J., Moon, E.J., Lu, J., Hosler, B.C., Caspi, E.N., May, S.J., Hultman, L., Eklund, P., et al. (2015). Experimental and theoretical characterization of ordered MAX phases Mo₂TiAlC₂ and Mo₂Ti₂AlC₃. *J. Appl. Phys.* 118, 094304. <https://doi.org/10.1063/1.4929640>.
76. Liu, R., and Li, W. (2018). High-thermal-stability and high-thermal-conductivity Ti₃C₂T_x MXene/poly(vinyl alcohol) (PVA) composites. *ACS Omega* 3, 2609–2617.

- <https://doi.org/10.1021/acsomega.7b02001>.
77. Guo, Y., Wang, T., Yang, Q., Li, X., Li, H., Wang, Y., Jiao, T., Huang, Z., Dong, B., Zhang, W., et al. (2020). Highly efficient electrochemical reduction of nitrogen to ammonia on surface termination modified $Ti_3C_2T_x$ MXene nanosheets. *ACS Nano* 14, 9089–9097. <https://doi.org/10.1021/acsnano.0c04284>.
 78. Guo, W., Surya, S.G., Babar, V., Ming, F., Sharma, S., Alshareef, H.N., Schwingenschlöggl, U., and Salama, K.N. (2020). Selective toluene detection with Mo_2CT_x MXene at room temperature. *ACS Appl. Mater. Interfaces* 12, 57218–57227. <https://doi.org/10.1021/acsnano.0c16302>.
 79. Naguib, M., Mochalin, V.N., Barsoum, M.W., and Gogotsi, Y. (2014). ChemInform abstract: 25th anniversary article: MXenes: a new family of two-dimensional materials. *Adv. Mater.* 26, 992–1005. <https://doi.org/10.1002/adma.201304138>.
 80. Hermawan, A., Zhang, B., Taufik, A., Asakura, Y., Hasegawa, T., Zhu, J., Shi, P., and Yin, S. (2020). CuO nanoparticles/ $Ti_3C_2T_x$ MXene hybrid nanocomposites for detection of toluene gas. *ACS Appl. Nano Mater.* 3, 4755–4766. <https://doi.org/10.1021/acsnano.0c00749>.
 81. Xie, X., Xue, Y., Li, L., Chen, S., Nie, Y., Ding, W., and Wei, Z. (2014). Surface Al leached Ti_3AlC_2 as a substitute for carbon for use as a catalyst support in a harsh corrosive electrochemical system. *Nanoscale* 6, 11035–11040. <https://doi.org/10.1039/C4NR02080D>.
 82. Peng, Q., Guo, J., Zhang, Q., Xiang, J., Liu, B., Zhou, A., Liu, R., and Tian, Y. (2014). Unique lead adsorption behavior of activated hydroxyl group in two-dimensional titanium carbide. *J. Am. Chem. Soc.* 136, 4113–4116. <https://doi.org/10.1021/ja500506k>.
 83. Yang, Z., Liu, A., Wang, C., Liu, F., He, J., Li, S., Wang, J., You, R., Yan, X., Sun, P., et al. (2019). Improvement of gas and humidity sensing properties of organ-like MXene by alkaline treatment. *ACS Sens.* 4, 1261–1269. <https://doi.org/10.1021/acssensors.9b00127>.
 84. Luo, S., Wu, Z., Zhao, J., Luo, Z., Qiu, Q., Li, Z., Wu, H., Xing, G., and Wu, C. (2022). ZIF-67 derivative decorated MXene for a highly integrated flexible self-powered photodetector. *ACS Appl. Mater. Interfaces* 14, 19725–19735. <https://doi.org/10.1021/acsnano.2c03148>.
 85. Naguib, M., Halim, J., Lu, J., Cook, K.M., Hultman, L., Gogotsi, Y., and Barsoum, M.W. (2013). New two-dimensional niobium and vanadium carbides as promising materials for Li-ion batteries. *J. Am. Chem. Soc.* 135, 15966–15969. <https://doi.org/10.1021/ja405735d>.
 86. Tian, W., Vahidmohammadi, A., Wang, Z., Ouyang, L., Beidaghi, M., and Hamed, M.M. (2019). Layer-by-layer self-assembly of pillared two-dimensional multilayers. *Nat. Commun.* 10, 2558. <https://doi.org/10.1038/s41467-019-10631-0>.
 87. Sun, C., Zuo, P., Sun, W., Xia, R., Dong, Z., Zhu, L., Lv, J., Deng, G., Tan, L., and Dai, Y. (2020). Self-assembly of alternating stacked 2D/2D $Ti_3C_2T_x$ MXene/ZnMnNi LDH van der Waals heterostructures with ultrahigh supercapacitive performance. *ACS Appl. Energy Mater.* 3, 10242–10254. <https://doi.org/10.1021/acsaem.0c02077>.
 88. Kim, H., Kee, J., Seo, D.R., Lee, Y., Ahn, C.W., and Koo, J. (2020). Large-area 2D-MXene nanosheet assemblies using Langmuir-schaefer technique: wrinkle formation. *ACS Appl. Mater. Interfaces* 12, 42294–42301. <https://doi.org/10.1021/acsnano.0c10990>.
 89. Adepu, V., Kunchur, A., Kolli, C.S.R., Siddhartha, S., Mattela, V., and Sahatiya, P. (2022). High-performance visible light photodetector based on 1D SnO_2 nanofibers with a $Ti_3C_2T_x$ (MXene) electron transport layer. *Nano Mater.* 5, 6852–6863. <https://doi.org/10.1016/j.mssp.2022.107161>.
 90. Wang, Z., Yu, K., Gong, S., Mao, H., Huang, R., and Zhu, Z. (2021). Cu_3BiS_3 /MXenes with excellent solar-thermal conversion for continuous and efficient seawater desalination. *ACS Appl. Mater. Interfaces* 13, 16246–16258. <https://doi.org/10.1021/acsnano.0c22761>.
 91. Cockreham, C.B., Zhang, X., Li, H., Hammond-Pereira, E., Sun, J., Saunders, S.R., Wang, Y., Xu, H., and Wu, D. (2019). Inhibition of $AlF_3 \cdot 3H_2O$ impurity formation in $Ti_3C_2T_x$ MXene synthesis under a unique CoF_3/HCl etching environment. *ACS Appl. Energy Mater.* 2, 8145–8152. <https://doi.org/10.1021/acsaem.9b01618>.
 92. Wang, X., Garnero, C., Rochard, G., Magne, D., Morisset, S., Hurand, S., Chartier, P., Rousseau, J., Cabioch, T., Coutanceau, C., et al. (2017). A new etching environment (FeF_3/HCl) for the synthesis of two-dimensional titanium carbide MXenes: a route towards selective reactivity vs. water. *J. Mater. Chem.* 5, 22012–22023. <https://doi.org/10.1039/C7TA01082F>.
 93. Zhang, C.J., Kremer, M.P., Seral-Ascaso, A., Park, S.H., McEvoy, N., Anasori, B., Gogotsi, Y., and Nicolosi, V. (2018). Stamping of flexible, coplanar micro-supercapacitors using MXene inks. *Adv. Funct. Mater.* 28, 1705506. <https://doi.org/10.1002/adfm.201705506>.
 94. Firestein, K.L., Fernando, J.F.S., Zhang, C., Lewis, C.-E.M., and Golberg, D.V. (2022). Delaminated V_2C MXene nanostructures prepared via LiF salt etching for electrochemical applications. *ACS Appl. Nano Mater.* 5, 12117–12125. <https://doi.org/10.1021/acsnano.2c01838>.
 95. Guan, Y., Jiang, S., Cong, Y., Wang, J., Dong, Z., Zhang, Q., Yuan, G., Li, Y., and Li, X. (2020). A hydrofluoric acid-free synthesis of 2D vanadium carbide (V_2C) MXene for supercapacitor electrodes. *2D Mater.* 7, 025010. <https://doi.org/10.1088/2053-1583/ab6706>.
 96. Liu, F., Zhou, J., Wang, S., Wang, B., Shen, C., Wang, L., Hu, Q., Huang, Q., and Zhou, A. (2017). Preparation of high-purity V_2C MXene and electrochemical properties as Li-ion batteries. *Soc.* 164, A709–A713. <https://doi.org/10.1149/2.0641704jes>.
 97. Natu, V., Pai, R., Sokol, M., Carey, M., Kalra, V., and Barsoum, M.W. (2020). 2D Ti_3C_2Tz MXene synthesized by water-free etching of Ti_3AlC_2 in polar organic solvents. *Chem* 6, 616–630. <https://doi.org/10.1016/j.chempr.2020.01.019>.
 98. Jing, H., Yeo, H., Lyu, B., Ryou, J., Choi, S., Park, J.-H., Lee, B.H., Kim, Y.-H., and Lee, S. (2021). Modulation of the electronic properties of MXene ($Ti_3C_2T_x$) via surface-covalent functionalization with diazonium. *ACS Nano* 15, 1388–1396. <https://doi.org/10.1021/acsnano.0c08664>.
 99. Kumar, S., Lei, Y., Alshareef, N.H., Quevedo-Lopez, M.A., and Salama, K.N. (2018). Biofunctionalized two-dimensional Ti_3C_2 MXenes for ultrasensitive detection of cancer biomarker. *Biosens. Bioelectron.* 121, 243–249. <https://doi.org/10.1016/j.bios.2018.08.076>.
 100. Sun, W., Shah, S.A., Chen, Y., Tan, Z., Gao, H., Habib, T., Radovic, M., and Green, M.J. (2017). Electrochemical etching of Ti_2AlC to Ti_2CT_x (MXene) in low-concentration hydrochloric acid solution. *J. Mater. Chem.* 5, 21663–21668. <https://doi.org/10.1039/C7TA05574A>.
 101. Lukatskaya, M.R., Halim, J., Dyatkin, B., Naguib, M., Buranova, Y.S., Barsoum, M.W., and Gogotsi, Y. (2014). Room-temperature carbide-derived carbon synthesis by electrochemical etching of MAX phases. *Angew. Chem. Int. Ed.* 53, 4877–4880. <https://doi.org/10.1002/anie.201402513>.
 102. Pang, S.-Y., Wong, Y.-T., Yuan, S., Liu, Y., Tsang, M.-K., Yang, Z., Huang, H., Wong, W.-T., and Hao, J. (2019). Universal strategy for HF-free facile and rapid synthesis of two-dimensional MXenes as multifunctional energy materials. *J. Am. Chem. Soc.* 141, 9610–9616. <https://doi.org/10.1021/jacs.9b02578>.
 103. Yang, S., Zhang, P., Wang, F., Ricciardulli, A.G., Lohe, M.R., Blom, P.W.M., and Feng, X. (2018). Fluoride-free synthesis of two-dimensional titanium carbide (MXene) using a binary aqueous system. *Angew. Chem.* 57, 15491–15495. <https://doi.org/10.1002/anie.201809662>.
 104. Chen, J., Chen, M., Zhou, W., Xu, X., Liu, B., Zhang, W., and Wong, C. (2022). Simplified synthesis of fluoride-free $Ti_3C_2T_x$ via electrochemical etching toward high-performance electrochemical capacitors. *ACS Nano* 16, 2461–2470. <https://doi.org/10.1021/acsnano.1c09004>.
 105. Bond, W., Smith, C., Gibson, J., Willett, I., and Willett. (1995). The effect of sulfate and fluoride on the mobility of aluminum in soil. *Soil Res.* 33, 501–507. <https://doi.org/10.1071/SR9950883>.
 106. Sulka, G.D., and Parkoła, K. (2007). Temperature influence on well-ordered

- nanopore structures grown by anodization of aluminium in sulphuric acid. *Electrochim. Acta* 52, 1880–1888. <https://doi.org/10.1016/j.electacta.2006.07.053>.
107. Yang, S., Zhang, P., Wang, F., Ricciardulli, A.G., Lohe, M.R., Blom, P.W.M., and Feng, X. (2018). Fluoride-free synthesis of two-dimensional titanium carbide (MXene) using a binary aqueous system. *Angew. Chem.* 130, 15717–15721. <https://doi.org/10.1002/anie.201809662>.
108. Shi, H., Zhang, P., Liu, Z., Park, S., Lohe, M.R., Wu, Y., Shaygan Nia, A., Yang, S., and Feng, X. (2021). Ambient-stable two-dimensional titanium carbide (MXene) enabled by iodine etching. *Angew. Chem., Int. Ed.* 60, 8689–8693. <https://doi.org/10.1002/anie.202015627>.
109. Bernard, J., Chatenet, M., and Dalard, F. (2006). Understanding aluminum behaviour in aqueous alkaline solution using coupled techniques - Part I. Rotating ring-disk study. *Electrochim. Acta* 52, 86–93. <https://doi.org/10.1016/j.electacta.2009.06.038>.
110. Yang, F., Ge, Y., Yin, T., Guo, J., Zhang, F., Tang, X., Qiu, M., Liang, W., Xu, N., Wang, C., et al. (2020). Ti₃C₂T_x MXene quantum dots with enhanced stability for ultrafast photonics. *ACS Appl. Nano Mater.* 3, 11850–11860. <https://doi.org/10.1021/acsnano.0c02369>.
111. Xuan, J., Wang, Z., Chen, Y., Liang, D., Cheng, L., Yang, X., Liu, Z., Ma, R., Sasaki, T., and Geng, F. (2016). Organic-base-driven intercalation and delamination for the production of functionalized titanium carbide nanosheets with superior photothermal therapeutic performance. *Angew. Chem.* 55, 14569–14574. <https://doi.org/10.1002/anie.201606643>.
112. Li, T., Yao, L., Liu, Q., Gu, J., Luo, R., Li, J., Yan, X., Wang, W., Liu, P., Chen, B., et al. (2018). Fluorine-free synthesis of high-purity Ti₃C₂T_x (T=OH, O) via alkali treatment. *Angew. Chem., Int. Ed.* 57, 6115–6119. <https://doi.org/10.1002/anie.201800887>.
113. Jiang, Y., Tian, M., Wang, H., Wei, C., Sun, Z., Rummeli, M.H., Strasser, P., Sun, J., and Yang, R. (2021). Mildly oxidized MXene (Ti₃C₂, Nb₂C, and V₂C) electrocatalyst via a generic strategy enables longevous Li-O₂ battery under a high rate. *ACS Nano* 15, 19640–19650. <https://doi.org/10.1021/acsnano.1c06896>.
114. Li, M., Lu, J., Luo, K., Li, Y., Chang, K., Chen, K., Zhou, J., Rosen, J., Hultman, L., Eklund, P., et al. (2019). Element replacement approach by reaction with Lewis acidic molten salts to synthesize nanolaminated MAX phases and MXenes. *J. Am. Chem. Soc.* 141, 4730–4737. <https://doi.org/10.1021/jacs.9b00574>.
115. Zhao, Q., Zhang, C., Hu, R., Du, Z., Gu, J., Cui, Y., Chen, X., Xu, W., Cheng, Z., Li, S., et al. (2021). Selective etching quaternary MAX phase toward single atom copper immobilized MXene (Ti₃C₂Cl_x) for efficient CO₂ electroreduction to methanol. *ACS Nano* 15, 4927–4936. <https://doi.org/10.1021/acsnano.0c09755>.
116. Liu, L., Orbay, M., Luo, S., Duluard, S., Shao, H., Harmel, J., Rozier, P., Taberna, P.-L., and Simon, P. (2022). Exfoliation and delamination of Ti₃C₂T_x MXene prepared via molten salt etching route. *ACS Nano* 16, 111–118. <https://doi.org/10.1021/acsnano.1c08498>.
117. Ma, G., Shao, H., Xu, J., Liu, Y., Huang, Q., Taberna, P.-L., Simon, P., and Lin, Z. (2021). Li-ion storage properties of two-dimensional titanium-carbide synthesized via fast one-pot method in air atmosphere. *Nat. Commun.* 12, 5085. <https://doi.org/10.1038/s41467-021-25306-y>.
118. Dong, H., Xiao, P., Jin, N., Wang, B., Liu, Y., and Lin, Z. (2021). Molten salt derived Nb₂C_{T_x} MXene anode for Li-ion batteries. *Chemelectrochem* 8, 957–962. <https://doi.org/10.1002/celec.202100142>.
119. Huang, P., Ying, H., Zhang, S., Zhang, Z., and Han, W.-Q. (2022). Molten salts etching route driven universal construction of MXene/transition metal sulfides heterostructures with interfacial electronic coupling for superior sodium storage. *Adv. Energy Mater.* 12, 2202052. <https://doi.org/10.1002/aenm.202202052>.
120. Shen, M., Jiang, W., Liang, K., Zhao, S., Tang, R., Zhang, L., and Wang, J.-Q. (2021). One-pot green process to synthesize MXene with controllable surface terminations using molten salts. *Angew. Chem.* 60, 27013–27018. <https://doi.org/10.1002/anie.202110640>.
121. Huang, P., and Han, W.-Q. (2023). Recent advances and perspectives of Lewis acidic etching route: an emerging preparation strategy for MXenes. *Nano-Micro Lett.* 15, 68. <https://doi.org/10.1007/s40820-023-01039-z>.
122. Kamysbayev, V., Filatov, A.S., Hu, H., Rui, X., Lagunas, F., Wang, D., Klie, R.F., and Talapin, D.V. (2020). Covalent surface modifications and superconductivity of two-dimensional metal carbide MXenes. *Science* 369, 979–983. <https://doi.org/10.1126/science.aba8311>.
123. Karthick, K., Suresh, S., Hussain, M.M.M., Ali, H.M., and Kumar, C.S. (2019). Evaluation of solar thermal system configurations for thermoelectric generator applications: a critical review. *Sol. Energy* 188, 111–142. <https://doi.org/10.1016/j.solener.2019.05.075>.
124. Parsa, S.M., Yazdani, A., Javadi, D., Afrand, M., Karimi, N., and Ali, H.M. (2022). Selecting efficient side of thermoelectric in pyramid-shape solar desalination units incorporated phase change material (PCM), nanoparticle, turbulator with battery storage powered by photovoltaic. *J. Energy Storage* 51, 104448. <https://doi.org/10.1016/j.est.2022.104448>.
125. Zhou, B., Li, S., Li, W., Li, J., Zhang, X., Lin, S., Chen, Z., and Pei, Y. (2017). Thermoelectric properties of SnS with Na-doping. *ACS Appl. Mater. Interfaces* 9, 34033–34041. <https://doi.org/10.1021/acsnano.7b08770>.
126. Perez-Taborda, J.A., Caballero-Calero, O., Vera-Londono, L., Briones, F., and Martin-Gonzalez, M. (2018). High thermoelectric zT in n-type silver selenide films at room temperature. *Adv. Energy Mater.* 8, 1702024. <https://doi.org/10.1002/aenm.201702024>.
127. Ge, Z.-H., Qin, P., He, D., Chong, X., Feng, D., Ji, Y.-H., Feng, J., and He, J. (2017). Highly enhanced thermoelectric properties of Bi/Bi₂S₃ nanocomposites. *ACS Appl. Mater. Interfaces* 9, 4828–4834. <https://doi.org/10.1021/acsnano.7b14803>.
128. Kim, G.H., Shao, L., Zhang, K., and Pipe, K.P. (2013). Engineered doping of organic semiconductors for enhanced thermoelectric efficiency. *Nat. Mater.* 12, 719–723. <https://doi.org/10.1038/nature13184>.
129. Jing, Z., Wang, H., Feng, X., Xiao, B., Ding, Y., Wu, K., and Cheng, Y. (2019). Superior thermoelectric performance of ordered double transition metal MXenes: Cr₂TiC₂T₂ (T = -OH or -F). *J. Phys. Chem. Lett.* 10, 5721–5728. <https://doi.org/10.1021/acs.jpclett.9b01827>.
130. Tippireddy, S., Kumar, P.D.S., Das, S., and Mallik, R.C. (2021). Oxychalcogenides as thermoelectric materials: an overview. *ACS Appl. Energy Mater.* 4, 2022–2040. <https://doi.org/10.1021/acsaem.0c02770>.
131. Khazaei, M., Arai, M., Sasaki, T., Chung, C.-Y., Venkataraman, N.S., Estili, M., Sakka, Y., and Kawazoe, Y. (2013). Novel electronic and magnetic properties of two-dimensional transition metal carbides and nitrides. *Adv. Funct. Mater.* 23, 2185–2192. <https://doi.org/10.1002/adfm.201202502>.
132. Khazaei, M., Arai, M., Sasaki, T., Estili, M., and Sakka, Y. (2014). Two-dimensional molybdenum carbides: potential thermoelectric materials of the MXene family. *Phys. Chem. Chem. Phys.* 16, 7841–7849. <https://doi.org/10.1039/C4CP00467A>.
133. Liu, P., Ding, W., Liu, J., Shen, L., Jiang, F., Liu, P., Zhu, Z., Zhang, G., Liu, C., and Xu, J. (2020). Surface termination modification on high-conductivity MXene film for energy conversion. *J. Alloys Compd.* 829, 154634. <https://doi.org/10.1016/j.jallcom.2020.154634>.
134. Omugbe, E., Osafire, O.E., Nenuwe, O.N., and Enaibe, E.A. (2022). Energy band gaps and novel thermoelectric properties of two-dimensional functionalized Yttrium carbides (MXenes). *Physica B: Phys. Condens. Matter* 639, 413922. <https://doi.org/10.1016/j.physb.2022.413922>.
135. Huang, D., Kim, H., Zou, G., Xu, X., Zhu, Y., Ahmad, K., Almutairi, Z.A., and Alshareef, H.N. (2022). All-MXene thermoelectric nanogenerator. *Mater. Today Energy* 29, 101129. <https://doi.org/10.1016/j.mtener.2022.101129>.
136. Zhao, L.-D., Lo, S.-H., Zhang, Y., Sun, H., Tan, G., Uher, C., Wolverson, C., Dravid, V.P., and Kanatzidis, M.G. (2014). Ultralow thermal conductivity and high thermoelectric figure of merit in SnSe crystals. *Nature* 508, 373–377. <https://doi.org/10.1038/nature13184>.

137. Hong, S., Zou, G., Kim, H., Huang, D., Wang, P., and Alshareef, H.N. (2020). Photothermoelectric response of $\text{Ti}_3\text{C}_2\text{Tx}$ MXene confined ion channels. *ACS Nano* 14, 9042–9049. <https://doi.org/10.1021/acsnano.0c04099>.
138. Sarikurt, S., Çakır, D., Keçeli, M., and Sevik, C. (2018). The influence of surface functionalization on thermal transport and thermoelectric properties. *Nanoscale* 10, 8859–8868. <https://doi.org/10.1039/C7NR09144C>.
139. Kumar, S., and Schwingenschlögl, U. (2016). Thermoelectric performance of functionalized Sc_2C MXenes. *Phys. Rev. B* 94, 035405. <https://doi.org/10.1103/PhysRevB.94.035405>.
140. Guo, Z., Miao, N., Zhou, J., Pan, Y., and Sun, Z. (2018). Coincident modulation of lattice and electron thermal transport performance in MXenes via surface functionalization. *Phys. Chem. Chem. Phys.* 20, 19689–19697. <https://doi.org/10.1039/C8CP02564A>.
141. Xu, X., Li, L., Liu, W., Chen, Z., Chen, D., and Shen, G. (2022). Thermally chargeable supercapacitor with 3D $\text{Ti}_3\text{C}_2\text{Tx}$ MXene hollow sphere based freestanding electrodes. *Adv. Mater. Interfac.* 9, 2201165. <https://doi.org/10.1002/admi.202201165>.
142. Lee, T., Lee, J.W., Park, K.T., Kim, J.-S., Park, C.R., and Kim, H. (2021). Nanostructured inorganic chalcogenide-carbon nanotube yarn having a high thermoelectric power factor at low temperature. *ACS Nano* 15, 13118–13128. <https://doi.org/10.1021/acsnano.1c02508>.
143. Choi, J., Jung, Y., Yang, S.J., Oh, J.Y., Oh, J., Jo, K., Son, J.G., Moon, S.E., Park, C.R., and Kim, H. (2017). Flexible and robust thermoelectric generators based on all-carbon nanotube yarn without metal electrodes. *ACS Nano* 11, 7608–7614. <https://doi.org/10.1021/acsnano.7b01771>.
144. Park, S., Mo, J.-H., Kim, S., Hwang, H., and Jang, K.-S. (2020). Shape-deformable thermoelectric carbon nanotube doughs. *ACS Appl. Mater. Interfaces* 12, 19415–19422. <https://doi.org/10.1021/acscami.0c00617>.
145. Blackburn, J.L., Ferguson, A.J., Cho, C., and Grunlan, J.C. (2018). Carbon-nanotube-based thermoelectric materials and devices. *Adv. Mater.* 30, 1704386. <https://doi.org/10.1002/adma.201704386>.
146. Wei, J., Wu, D., Liu, C., Zhong, F., Cao, G., Li, B., Gao, C., and Wang, L. (2022). Free-standing p-Type SWCNT/MXene composite films with low thermal conductivity and enhanced thermoelectric performance. *Chem. Eng. J.* 439, 135706. <https://doi.org/10.1016/j.cej.2022.135706>.
147. Zhang, D., Yin, R., Zheng, Y., Li, Q., Liu, H., Liu, C., and Shen, C. (2022). Multifunctional MXene/CNTs based flexible electronic textile with excellent strain sensing, electromagnetic interference shielding and Joule heating performances. *Chem. Eng. J.* 438, 135587. <https://doi.org/10.1016/j.cej.2022.135587>.
148. Ding, W., Liu, P., Bai, Z., Wang, Y., Liu, G., Jiang, Q., Jiang, F., Liu, P., Liu, C., and Xu, J. (2020). Constructing layered MXene/CNTs composite film with 2D-3D sandwich structure for high thermoelectric performance. *Adv. Mater. Interfac.* 7, 2001340. <https://doi.org/10.1002/admi.202001340>.
149. Li, Q.-Y., Feng, T., Okita, W., Komori, Y., Suzuki, H., Kato, T., Kaneko, T., Ikuta, T., Ruan, X., and Takahashi, K. (2019). Enhanced thermoelectric performance of as-grown suspended graphene nanoribbons. *ACS Nano* 13, 9182–9189. <https://doi.org/10.1021/acsnano.9b03521>.
150. Zhao, M., Kim, D., Nguyen, V.L., Jiang, J., Sun, L., Lee, Y.H., and Yang, H. (2019). Coherent thermoelectric power from graphene quantum dots. *Nano Lett.* 19, 61–68. <https://doi.org/10.1021/acs.nanolett.8b03208>.
151. Harzheim, A., Spiece, J., Evangeli, C., McCann, E., Falko, V., Sheng, Y., Warner, J.H., Briggs, G.A.D., Mol, J.A., Gehring, P., and Kolosov, O.V. (2018). Geometrically enhanced thermoelectric effects in graphene nanoconstrictions. *Nano Lett.* 18, 7719–7725. <https://doi.org/10.1021/acs.nanolett.8b03406>.
152. Saeidi-Javash, M., Du, Y., Zeng, M., Wyatt, B.C., Zhang, B., Kempf, N., Anasori, B., and Zhang, Y. (2021). All-printed MXene-graphene nanosheet-based bimodal sensors for simultaneous strain and temperature sensing. *ACS Appl. Electron. Mater.* 3, 2341–2348. <https://doi.org/10.1021/acsaem.1c00218>.
153. Park, J., and Jeong, Y.G. (2022). Thermoelectric and photothermoelectric properties of nanocomposite films based on polybenzimidazole and carbon nanotubes. *ACS Appl. Electron. Mater.* 4, 386–393. <https://doi.org/10.1021/acsaem.1c01056>.
154. Xie, Z., Wang, J., and Yeow, J.T.W. (2022). Doped polyaniline/graphene composites for photothermoelectric detectors. *ACS Appl. Nano Mater.* 5, 7967–7973. <https://doi.org/10.1021/acsnanm.2c01039>.
155. Wu, Z., Zhai, Y., Kim, H., Azoulay, J.D., and Ng, T.N. (2018). Emerging design and characterization guidelines for polymer-based infrared photodetectors. *Acc. Chem. Res.* 51, 3144–3153. <https://doi.org/10.1021/acs.accounts.8b00446>.
156. Hasegawa, T., Ashizawa, M., Hayashi, Y., Kawauchi, S., Masunaga, H., Hikima, T., Manaka, T., and Matsumoto, H. (2019). P- and n-channel photothermoelectric conversion based on ultralong near-infrared wavelengths absorbing polymers. *ACS Appl. Polym. Mater.* 1, 542–551. <https://doi.org/10.1021/acscpm.8b00234>.
157. Jin, X.-z., Yang, Z.-y., Huang, C.-h., Yang, J.-h., and Wang, Y. (2022). PEDOT:PSS/MXene/PEG composites with remarkable thermal management performance and excellent HF-band & X-band electromagnetic interference shielding efficiency for electronic packaging. *Chem. Eng. J.* 448, 137599. <https://doi.org/10.1016/j.cej.2022.137599>.
158. Jiang, C., Chen, J., Lai, X., Li, H., Zeng, X., Zhao, Y., Zeng, Q., Gao, J., Wu, Z., and Qiu, Y. (2022). Mechanically robust and multifunctional polyimide/MXene composite aerogel for smart fire protection. *Chem. Eng. J.* 434, 134630. <https://doi.org/10.1016/j.cej.2022.134630>.
159. Zeng, Q., Wang, B., Lai, X., Li, H., Chen, Z., Xie, H., and Zeng, X. (2023). Multifunctional MXene-suspended cotton fabric with enhanced thermopower for smart fire protection. *Composites Part A* 164, 107305. <https://doi.org/10.1016/j.compositesa.2022.107305>.
160. Ma, T., Li, L., Pan, M., Guo, C., and Mei, C. (2023). Multifunctional MXene-based fire alarm wallpaper with sandwich-like structure for enhanced fire safety and prevention. *Chem. Eng. J.* 451, 138517. <https://doi.org/10.1016/j.cej.2022.138517>.
161. Wang, B., Lai, X., Li, H., Jiang, C., Gao, J., and Zeng, X. (2021). Multifunctional MXene/chitosan-coated cotton fabric for intelligent fire protection. *ACS Appl. Mater. Interfaces* 13, 23020–23029. <https://doi.org/10.1021/acscami.1c05222>.
162. Chen, W., Liu, P., Liu, Y., and Liu, Z. (2022). Recent advances in Two-dimensional $\text{Ti}_3\text{C}_2\text{T}_x$ MXene for flame retardant polymer materials. *Chem. Eng. J.* 446, 137239. <https://doi.org/10.1016/j.cej.2022.137239>.
163. Mao, M., Yu, K.-X., Cao, C.-F., Gong, L.-X., Zhang, G.-D., Zhao, L., Song, P., Gao, J.-F., and Tang, L.-C. (2022). Facile and green fabrication of flame-retardant $\text{Ti}_3\text{C}_2\text{T}_x$ MXene networks for ultrafast, reusable and weather-resistant fire warning. *Chem. Eng. J.* 427, 131615. <https://doi.org/10.1016/j.cej.2021.131615>.
164. Zhang, L., Huang, Y., Dong, H., Xu, R., and Jiang, S. (2021). Flame-retardant shape memory polyurethane/MXene paper and the application for early fire alarm sensor. *Composites Part B: Eng.* 223, 109149. <https://doi.org/10.1016/j.compositesb.2021.109149>.
165. Li, X., Río Saez, J.S.d., Ao, X., Vázquez-López, A., Xu, X., Xu, B., and Wang, D.-Y. (2022). Smart Low-temperature responsive fire alarm based on MXene/Graphene oxide film with wireless transmission: remote real-time luminosity detection. *Colloids Surf. A Physicochem. Eng. Asp.* 651, 129641. <https://doi.org/10.1016/j.colsurfa.2022.129641>.
166. Peng, T., Wang, S., Xu, Z., Tang, T., and Zhao, Y. (2022). Multifunctional MXene/aramid nanofiber composite films for efficient electromagnetic interference shielding and repeatable early fire detection. *ACS Omega* 7, 29161–29170. <https://doi.org/10.1021/acsomega.2c03219>.
167. Zhang, Y., Huang, Y., Li, M.-C., Zhang, S., Zhou, W., Mei, C., and Pan, M. (2023). Bioinspired, stable adhesive $\text{Ti}_3\text{C}_2\text{Tx}$ MXene-based coatings towards fire warning, smoke suppression and VOCs

- removal smart wood. *Chem. Eng. J.* 452, 139360.
168. Zhao, Y., Chen, J., Lai, X., Li, H., Zeng, X., Jiang, C., Zeng, Q., Li, K., Wu, Z., and Qiu, Y. (2022). Efficient flame-retardant and multifunctional polyimide/MXene composite aerogel for intelligent fire protection. *Composites Part A* 163, 107210. <https://doi.org/10.1016/j.compositesa.2022.107210>.
169. Mao, Y., Wang, D., Hu, J., and Fu, S. (2023). Mechanically flexible and flame retardant polyphenol-bridged casein/MXene composite for fire proofing repeatable contact/non-contact fire monitoring. *Chem. Eng. J.* 454, 140161. <https://doi.org/10.1016/j.cej.2022.140161>.
170. Zeng, Q., Zhao, Y., Lai, X., Jiang, C., Wang, B., Li, H., Zeng, X., and Chen, Z. (2022). Skin-inspired multifunctional MXene/cellulose nanocoating for smart and efficient fire protection. *Chem. Eng. J.* 446, 136899. <https://doi.org/10.1016/j.cej.2022.136899>.
171. Li, B.-X., Qin, L., Yang, D., Luo, Z., Zhao, T., and Yu, Z.-Z. (2022). Superelastic and responsive anisotropic silica nanofiber/polyvinylpyrrolidone/MXene hybrid aerogels for efficient thermal insulation and overheating alarm applications. *Compos. Sci. Technol.* 225, 109484. <https://doi.org/10.1016/j.compscitech.2022.109484>.
172. Li, X., Sánchez del Río Saez, J., Ao, X., Yusuf, A., and Wang, D.-Y. (2022). Highly sensitive fire alarm system based on cellulose paper with low temperature response and wireless signal conversion. *Chem. Eng. J.* 431, 134108. <https://doi.org/10.1016/j.cej.2021.134108>.
173. Du, X., Wang, J., Jin, L., Deng, S., Dong, Y., and Lin, S. (2022). Dopamine-decorated $\text{Ti}_3\text{C}_2\text{Tx}$ MXene/cellulose nanofiber aerogels supported form-stable phase change composites with superior solar-thermal conversion efficiency and extremely high thermal storage density. *ACS Appl. Mater. Interfaces* 14, 15225–15234. <https://doi.org/10.1021/acsmi.2c00117>.
174. Xiao, F., Yoo, B., Lee, K.H., and Myung, N.V. (2007). Synthesis of Bi_2Te_3 nanotubes by galvanic displacement. *J. Am. Chem. Soc.* 129, 10068–10069. <https://doi.org/10.1021/ja073032w>.
175. Li, W., Poudel, B., Nozariasbmarz, A., Sriramdas, R., Zhu, H., Kang, H.B., and Priya, S. (2020). Bismuth telluride/half-heusler segmented thermoelectric unicolor modules provide 12 % conversion efficiency. *Adv. Energy Mater.* 10, 2001924. <https://doi.org/10.1002/aenm.202001924>.
176. Mi, J.-L., Lock, N., Sun, T., Christensen, M., Søndergaard, M., Hald, P., Hng, H.H., Ma, J., and Iversen, B.B. (2010). Biomolecule-assisted hydrothermal synthesis and self-assembly of Bi_2Te_3 nanostring-cluster hierarchical structure. *ACS Nano* 4, 2523–2530. <https://doi.org/10.1021/nn100267q>.
177. Han, G., Chen, Z.-G., Yang, L., Hong, M., Drennan, J., and Zou, J. (2015). Rational design of Bi_2Te_3 polycrystalline whiskers for thermoelectric applications. *ACS Appl. Mater. Interfaces* 7, 989–995. <https://doi.org/10.1021/am5078528>.
178. Cheng, Y., Yang, J., Luo, Y., Li, W., Vtyurin, A., Jiang, Q., Dunn, S., and Yan, H. (2022). Enhancement of thermoelectric performance in $\text{Bi}_{0.5}\text{Sb}_{1.5}\text{Te}_3$ particulate composites including ferroelectric BaTiO_3 nanodots. *ACS Appl. Mater. Interfaces* 14, 37204–37212. <https://doi.org/10.1021/acsmi.2c10424>.
179. Li, S., Fan, T., Liu, X., Liu, F., Meng, H., Liu, Y., and Pan, F. (2017). Graphene quantum dots embedded in Bi_2Te_3 nanosheets to enhance thermoelectric performance. *ACS Appl. Mater. Interfaces* 9, 3677–3685. <https://doi.org/10.1021/acsmi.6b14274>.
180. Li, Y., Zhao, Y., Qiao, J., Jiang, S., Qiu, J., Tan, J., Zhang, L., Gai, Z., Tai, K., and Liu, C. (2020). A flexible and infrared-transparent Bi_2Te_3 -carbon nanotube thermoelectric hybrid for both active and passive cooling. *ACS Appl. Electron. Mater.* 2, 3008–3016. <https://doi.org/10.1021/acsaem.0c00617>.
181. Jung, S.-h., Kim, K.T., Lee, G.-S., Sun, J.-Y., Kim, D.W., Eom, Y.S., Yang, D.Y., Yu, J., Park, J.M., Hyeon, D.Y., and Park, K.-I. (2021). Synergistically improved thermoelectric energy harvesting of edge-oxidized-graphene-bridged N-type bismuth telluride thick films. *ACS Appl. Mater. Interfaces* 13, 5125–5132. <https://doi.org/10.1021/acsmi.0c20509>.
182. Wang, C.-H., Hsieh, H.-C., Sun, Z.-W., Ranganayakulu, V.K., Lan, T.-w., Chen, Y.-Y., Chang, Y.-Y., and Wu, A.T. (2020). Interfacial stability in Bi_2Te_3 thermoelectric joints. *ACS Appl. Mater. Interfaces* 12, 27001–27009. <https://doi.org/10.1021/acsmi.9b22853>.
183. Kim, K.-C., Lim, S.-S., Lee, S.H., Hong, J., Cho, D.-Y., Mohamed, A.Y., Koo, C.M., Baek, S.-H., Kim, J.-S., and Kim, S.K. (2019). Precision interface engineering of an atomic layer in bulk Bi_2Te_3 alloys for high thermoelectric performance. *ACS Nano* 13, 7146–7154. <https://doi.org/10.1021/acsnano.9b02574>.
184. Lu, X., Zhang, Q., Liao, J., Chen, H., Fan, Y., Xing, J., Gu, S., Huang, J., Ma, J., Wang, J., et al. (2020). High-efficiency thermoelectric power generation enabled by homogeneous incorporation of MXene in $(\text{Bi,Sb})_2\text{Te}_3$ matrix. *Adv. Energy Mater.* 10, 1902986. <https://doi.org/10.1002/aenm.201902986>.
185. Diao, J., Yuan, J., Cai, Z., Xia, L., Cheng, Z., Liu, X., Ma, W., Wang, S., and Huang, Y. (2022). High-performance electromagnetic interference shielding and thermoelectric conversion derived from multifunctional $\text{Bi}_2\text{Te}_{2.7}\text{Se}_{0.3}$ /MXene composites. *Carbon* 196, 243–252. <https://doi.org/10.1016/j.carbon.2022.04.078>.
186. Zhang, D., Cao, Y., Hui, Y., Cai, J., Ji, J., Yin, H., Zhang, M., Xu, J., and Zhang, Q. (2022). Enhancements of thermoelectric performance in n-type Bi_2Te_3 -based nanocomposites through incorporating 2D Mxenes. *J. Eur. Ceram. Soc.* 42, 4587–4593. <https://doi.org/10.1016/j.jeurceramsoc.2022.04.047>.
187. Shi, X., Wu, A., Liu, W., Moshwan, R., Wang, Y., Chen, Z.-G., and Zou, J. (2018). Polycrystalline SnSe with extraordinary thermoelectric property via nanoporous design. *ACS Nano* 12, 11417–11425. <https://doi.org/10.1021/acsnano.8b06387>.
188. Chandra, S., Banik, A., and Biswas, K. (2018). n-Type ultrathin few-layer nanosheets of Bi-doped SnSe: synthesis and thermoelectric properties. *ACS Energy Lett.* 3, 1153–1158. <https://doi.org/10.1021/acsenerylett.8b00399>.
189. Zhang, H., Chen, Y., Liu, X., Wang, H., Niu, C., Zheng, S., Zhang, B., Lu, X., Wang, G., Han, G., and Zhou, X. (2022). Enhancing the thermoelectric performance of solution-synthesized SnSe-based materials via incorporating $\text{Ti}_3\text{C}_2\text{Tx}$ MXene. *Mater. Today Energy* 30, 101137. <https://doi.org/10.1016/j.mtener.2022.101137>.
190. Wei, Y., Zhou, Z., Liu, J., Zhang, B., Wang, G., Han, G., Wang, G., Zhou, X., and Lu, X. (2022). MXene as charge reservoir promotes the thermoelectric performance of layered metal selenide SnSe_2 . *Acta Mater.* 241, 118369. <https://doi.org/10.1016/j.actamat.2022.118369>.
191. Jiang, X.-P., Tian, B.-Z., Sun, Q., Li, X.-L., Chen, J., Tang, J., Zhang, P., Yang, L., and Chen, Z.-G. (2021). Enhanced thermoelectric performance in MXene/SnTe nanocomposites synthesized via a facile one-step solvothermal method. *J. Solid State Chem.* 304, 122605. <https://doi.org/10.1016/j.jssc.2021.122605>.
192. Dixit, P., Jana, S.S., and Maiti, T. (2023). Enhanced thermoelectric performance of rare-earth-free n-type oxide perovskite composite with graphene analogous 2D MXene. *Small*, 2206710. <https://doi.org/10.1002/sml.202206710>.
193. Karttunen, A.J., Sarnes, L., Townsend, R., Mikkonen, J., and Karppinen, M. (2017). Flexible thermoelectric ZnO-organic superlattices on cotton textile substrates by ALD/MLD. *Adv. Electron. Mater.* 3, 1600459. <https://doi.org/10.1002/aeml.201600459>.
194. Roy, A., Cheng, Y.-T., and Falk, M.L. (2016). Amorphous ZnO-based compounds as thermoelectrics. *J. Phys. Chem. C* 120, 2529–2535. <https://doi.org/10.1021/acs.jpcc.5b11618>.
195. Chen, D., Zhao, Y., Chen, Y., Wang, B., Chen, H., Zhou, J., and Liang, Z. (2015). One-step chemical synthesis of ZnO/graphene oxide molecular hybrids for high-temperature thermoelectric applications. *ACS Appl. Mater. Interfaces* 7, 3224–3230. <https://doi.org/10.1021/am507882f>.
196. Luu, S.D.N., Duong, T.A., and Phan, T.B. (2019). Effect of dopants and nanostructuring on the thermoelectric properties of ZnO materials. *Adv. Nat. Sci. Nanosci. Nanotechnol.* 10, 023001.

<https://doi.org/10.1088/2043-6254/ab22ad>.

197. Nam, W.H., Lim, Y.S., Choi, S.M., Seo, W.S., and Lee, J.Y. (2012). High-temperature charge transport and thermoelectric properties of a degenerately Al-doped ZnO nanocomposite. *J. Mater. Chem.* *22*, 14633–14638. <https://doi.org/10.1039/C2JM31763J>.
198. Jood, P., Mehta, R.J., Zhang, Y., Peleckis, G., Wang, X., Siegel, R.W., Borca-Tasciuc, T., Dou, S.X., and Ramanath, G. (2011). Al-doped zinc oxide nanocomposites with enhanced thermoelectric properties. *Nano Lett.* *11*, 4337–4342. <https://doi.org/10.1021/nl202439h>.
199. Look, D.C., Reynolds, D.C., Szelove, J.R., Jones, R.L., Litton, C.W., Cantwell, G., and Harsch, W.C. (1998). Electrical properties of bulk ZnO. *Solid State Commun.* *105*, 399–401. [https://doi.org/10.1016/S0038-1098\(97\)10145-4](https://doi.org/10.1016/S0038-1098(97)10145-4).
200. Yan, L., Luo, X., Yang, R., Dai, F., Zhu, D., Bai, J., Zhang, L., and Lei, H. (2022). Highly thermoelectric ZnO@MXene (Ti₃C₂T_x) composite films grown by atomic layer deposition. *ACS Appl. Mater. Interfaces* *14*, 34562–34570. <https://doi.org/10.1021/acsmami.2c05003>.
201. Kim, H., Wang, Z., Hedhili, M.N., Wehbe, N., and Alshareef, H.N. (2017). Oxidant-dependent thermoelectric properties of undoped ZnO films by atomic layer deposition. *Chem. Mater.* *29*, 2794–2802. <https://doi.org/10.1021/acs.chemmater.6b04654>.
202. Yang, C., Souchay, D., Kneiß, M., Bogner, M., Wei, H.M., Lorenz, M., Oeckler, O., Benstetter, G., Fu, Y.Q., and Grundmann, M. (2017). Transparent flexible thermoelectric material based on non-toxic earth-abundant p-type copper iodide thin film. *Nat. Commun.* *8*, 16076. <https://doi.org/10.1038/ncomms16076>.
203. Almasoudi, M., Saeed, A., Salah, N., Alshahrie, A., Hasan, P.M.Z., Melaibari, A., and Koumoto, K. (2022). CuI: a promising halide for thermoelectric applications below 373 K. *ACS Appl. Energy Mater.* *5*, 10177–10186. <https://doi.org/10.1021/acsaem.2c01929>.
204. Morais Faustino, B.M., Gomes, D., Faria, J., Juntunen, T., Gaspar, G., Bianchi, C., Almeida, A., Marques, A., Tittonen, I., and Ferreira, I. (2018). CuI p-type thin films for highly transparent thermoelectric p-n modules. *Sci. Rep.* *8*, 6867. <https://doi.org/10.1038/s41598-018-25106-3>.